

Two-dimensional vortices in strain and shear flows

Citation for published version (APA):

Trieling, R. R. (1996). *Two-dimensional vortices in strain and shear flows*. [Phd Thesis 1 (Research TU/e / Graduation TU/e), Applied Physics and Science Education]. Technische Universiteit Eindhoven.
<https://doi.org/10.6100/IR470032>

DOI:

[10.6100/IR470032](https://doi.org/10.6100/IR470032)

Document status and date:

Published: 01/01/1996

Document Version:

Publisher's PDF, also known as Version of Record (includes final page, issue and volume numbers)

Please check the document version of this publication:

- A submitted manuscript is the version of the article upon submission and before peer-review. There can be important differences between the submitted version and the official published version of record. People interested in the research are advised to contact the author for the final version of the publication, or visit the DOI to the publisher's website.
- The final author version and the galley proof are versions of the publication after peer review.
- The final published version features the final layout of the paper including the volume, issue and page numbers.

[Link to publication](#)

General rights

Copyright and moral rights for the publications made accessible in the public portal are retained by the authors and/or other copyright owners and it is a condition of accessing publications that users recognise and abide by the legal requirements associated with these rights.

- Users may download and print one copy of any publication from the public portal for the purpose of private study or research.
- You may not further distribute the material or use it for any profit-making activity or commercial gain
- You may freely distribute the URL identifying the publication in the public portal.

If the publication is distributed under the terms of Article 25fa of the Dutch Copyright Act, indicated by the "Taverne" license above, please follow below link for the End User Agreement:

www.tue.nl/taverne

Take down policy

If you believe that this document breaches copyright please contact us at:

openaccess@tue.nl

providing details and we will investigate your claim.

**Two-Dimensional Vortices
in
Strain and Shear Flows**

An abstract painting featuring a central vortex-like structure. The vortex is composed of concentric, swirling bands of color, primarily red and green, with some yellow and white highlights. The background is a textured, mottled mix of red, brown, and green. The overall style is expressive and painterly, with visible brushstrokes and a sense of movement.

R.R. Trieling

Two-Dimensional Vortices
in
Strain and Shear Flows

by R.R. Trieling

Ruben Trieling
Fluid Dynamics Laboratory
Eindhoven University of Technology
P.O. Box 513
5600 MB Eindhoven
The Netherlands

Cover illustration by Ingrid IJsselmuiden

Trieling, Ruben Robert
Two-Dimensional Vortices in Strain and Shear Flows / Ruben
Robert Trieling. - Eindhoven : Technische Universiteit Eindhoven
Proefschrift Technische Universiteit Eindhoven. - Met lit. opg. -
Met samenvatting in het Nederlands en Engels.
ISBN 90-386-0039-9

Two-Dimensional Vortices
in
Strain and Shear Flows

PROEFSCHRIFT

ter verkrijging van de graad van doctor aan de
Technische Universiteit Eindhoven, op gezag
van de Rector Magnificus, prof.dr. M. Rem,
voor een commissie aangewezen door het College
van Dekanen in het openbaar te verdedigen op

woensdag 27 november 1996 om 16.00 uur

door

RUBEN ROBERT TRIELING

geboren te Dordrecht

Dit proefschrift is goedgekeurd door de promotoren:

prof.dr.ir. G.J.F. van Heijst

en

prof.dr.ir. L. van Wijngaarden



This research was supported by the Netherlands Foundation for Fundamental Research on Matter (FOM).

Contents

1	Introduction	3
2	Decay of monopolar vortices in a stratified fluid	7
2.1	Introduction	7
2.2	The extended decay model	8
2.2.1	Horizontal diffusion	9
2.2.2	Vertical diffusion	11
2.3	Experimental arrangement	12
2.4	Results	13
2.4.1	Cross-sectional distributions of velocity and vorticity	13
2.4.2	The (ω, ψ) -relationship	15
2.4.3	The net circulation	17
2.4.4	Comparison with the extended decay model	18
2.5	Discussion and conclusions	22
3	Dynamics of monopolar vortices in a strain flow	25
3.1	Introduction	25
3.2	Experimental arrangement	25
3.3	Strain flow characteristics	26
3.4	Monopolar vortices in a still ambient flow	33
3.5	Observed behaviour of a monopolar vortex in a strain flow	34
3.6	Modelling of monopolar vortices in a strain flow	47
3.6.1	Motion of a uniform elliptic vortex in a pure strain flow	47
3.6.2	Modelling of a distributed vortex in a pure strain flow	55
3.7	Discussion and conclusions	63
4	Kinematic properties of monopolar vortices in a strain flow	65
4.1	Introduction	65
4.2	Experimental set-up	66
4.3	Laboratory observations	67
4.4	Advection properties of the point-vortex model	72
4.4.1	Point-vortex model	72
4.4.2	Contour kinematics	74

4.4.3	Comparison with experimental results	80
4.5	Effect of distributed vorticity on the advection properties	82
4.6	Discussion and conclusions	87
5	Monopolar vortices in an irrotational annular shear flow	89
5.1	Introduction	89
5.2	Theoretical description of the source-sink flow	90
5.3	Experimental arrangement	92
5.3.1	Shear flow generation	93
5.3.2	Monopole generation	93
5.3.3	Flow visualization and measurements	93
5.4	Laboratory observations	94
5.4.1	Shear flow characteristics	94
5.4.2	Monopolar vortex characteristics	96
5.4.3	Evolution of the monopolar vortex in the shear flow	97
5.5	Kinematic description of vortex stripping	100
5.6	The influence of distributed vorticity	109
5.7	Conclusions	112
6	Dipolar vortices in a strain flow	113
6.1	Introduction	113
6.2	Experimental arrangement	114
6.3	Dipolar vortex in cooperative strain flow	115
6.3.1	Qualitative observations	115
6.3.2	Kinematic explanation of the head-tail formation	118
6.3.3	Quantitative observations	121
6.3.4	Numerical simulations	126
6.4	Dipolar vortex in adverse strain flow	129
6.4.1	Laboratory observations	129
6.4.2	Numerical simulations	133
6.5	Conclusions	135
7	Conclusions	137
	References	139
	Summary	144
	Samenvatting	145
	Dankwoord	146
	Curriculum Vitae	147

Chapter 1

Introduction

Two-dimensional vortices play an important part in large-scale geophysical flow systems, such as the planetary atmospheres and the world's oceans. Typical examples of large-scale vortices are the high and low pressure cells in the atmosphere and the Gulf Stream Rings in the Atlantic Ocean. Both the atmosphere and the ocean can be considered as thin layers covering the Earth, in which the depth scale of the flow is typically a few kilometers, whereas the horizontal scale is of the order of hundreds, or even thousands, of kilometers. Consequently, the motion of large-scale vortices is approximately two-dimensional. Furthermore, the planar motion is encouraged by both the rotation of the Earth and the vertical density stratification of geophysical flows.

The dynamics of two-dimensional flows is completely different from that of three-dimensional flows: two-dimensional flows are characterized by a spectral flux of kinetic energy to larger length scales (inverse energy cascade), leading to the self-organization of the flow. Indeed, satellite observations have revealed the presence of large-scale vortical structures, and also numerical studies have confirmed the formation of coherent structures in two-dimensional flow domains (see for example McWilliams (1984) and Legras, Santangelo & Benzi (1988)). In the laboratory, coherent vortex structures have been observed in a number of different situations, such as in rotating fluids (see Hopfinger & van Heijst (1993) for a recent overview), stratified flows (see e.g. van Heijst & Flór (1989)) and in soap films (Couder & Basdevant (1986)). Moreover, two-dimensional flows have been established by external magnetic forces, for example in magneto-hydrodynamic systems (Nguyen Duc & Sommeria (1988)) and in plasmas.

Two-dimensional vortices can be classified, based on their topological shape, into monopolar, dipolar and other multipolar vortex structures. Among these, the monopolar vortex is the most common type, which usually has a circular or elliptic core of single-signed vorticity, and possibly a ring of oppositely-signed vorticity. Geophysical examples of this vortex structure are the high and low pressure cells in the atmosphere, and oceanic eddies, such as cold- and warm-core eddies in the Gulf Stream and the Agulhas Current (see Robinson (1983)). Experimentally, monopolar vortices have been observed both in rotating and in stratified fluids (see Hopfinger & van Heijst (1993)). Another vortex type is the dipolar vortex, which is characterized by two closely packed patches of oppositely-signed

vorticity. The dipolar vortex is important because of its self-propelling motion which leads to the transport of heat, salt and other properties. Dipoles have been observed both in nature (see for example Ahlnäs, Royer & George (1987) and Fedorov & Ginsburg (1989)) and in the laboratory (see e.g. Flór & van Heijst (1994)).

An important question concerns the stability of these different vortex types when embedded in a shearing background flow field, the deformation being induced only by the straining part of the shear flow. Large-scale vortices in the Earth's atmosphere and oceanic eddies may experience a shearing background flow by their mutual interaction or by the global zonal currents. The most dramatic examples of stable vortices in shear flows are the Great Red Spot of the planet Jupiter, which has existed for more than 300 years, and the Great Dark Spot of Neptune.

The study of two-dimensional vortices in ambient flows is relevant for a better understanding of the mixing between the ozone depleted region in the stratosphere above Antarctica and the atmosphere at lower latitudes (see McIntyre (1989) and Waugh *et al.* (1994)). Chaotic advection provides an effective mixing of the fluid around these vortices, and therefore plays an important role in the exchange of physical properties. Ambient flows may also influence the evolution of dipolar vortex structures. For example, dipolar vortices may lead to a phenomenon called 'atmospheric blocking' (see McWilliams (1980) and Butchart, Haines & Marshall (1989)), which means that the global west-east circulation is locally hindered or 'blocked' by two pressure cells of opposite circulation. Atmospheric blocking systems may persist for a relatively long time and consequently may have a large effect on the local weather conditions. Therefore, it is essential to investigate the effect of a deforming background flow on the stability of these systems.

The behaviour of two-dimensional vortices in strain and shear flows has been studied by a number of investigators. An interesting analytical solution for an unsteady elliptical vortex in a uniform shear flow was found by Chaplygin (1899) and independently by Kida (1981) (see Meleshko & van Heijst (1994a) for a review on Chaplygin's earlier work). Depending on the relative magnitudes of the uniform vorticity in the vortex and that of the shear flow, the vortex was found to exhibit various types of motion, such as rotation and shape oscillations. This analytical model was recently used to describe the observed motion of Neptune's Great Dark Spot (see Polvani *et al.* (1990)). In the last few years, a number of interesting results concerning vortices in shear flows have been obtained from numerical simulations. For example, numerical studies by Dritschel (1989) and Legras & Dritschel (1993, 1994) have shown that for a vortex with a non-uniform vorticity distribution embedded in a shear flow, weak vorticity is being removed from the edge of the vortex; a phenomenon called 'vortex-stripping'.

For some reason, however, only few experimental studies have been performed related to the field of two-dimensional vortices in ambient flows. So far, laboratory observations have been reported by Brickman & Ruddick (1990), who considered the effect of a time-dependent strain flow on a lens in a rotating fluid, and by Paireau, Tabeling & Legras (1996), who examined the deformation of monopolar vortices in an approximately uniform shear flow. However, many other experimental work is still lacking. For example, the behaviour of dipolar vortices in straining or shearing background flows has as yet not been

observed in the laboratory.

Therefore, in this thesis, the evolution characteristics of two-dimensional vortices in strain and shear flows are investigated experimentally, and a comparison is made with analytical and numerical models. The attention will be restricted to monopolar and dipolar vortices. Two-dimensional flows were established in the laboratory either by density stratification or by background rotation, and the vortex motion was created by applying similar techniques to those used in previous work (see Flór & van Heijst (1996) and Kloosterziel & van Heijst (1992)). The strain flow was generated in a stratified fluid by a suitable arrangement of rotating discs, whereas the shear flow was created in a rotating fluid by an appropriate source-sink configuration. Flow-visualization techniques were used to observe the qualitative behaviour of the flow field, whereas quantitative information was obtained by tracking small tracer particles.

Theoretically, the laboratory observations are compared with analytical and numerical models. As a first approach, the monopolar and dipolar vortices are modelled numerically by point vortices surrounded with contours of passive tracers; a technique which is usually referred to as contour kinematics (see Meleshko & van Heijst (1994b)). As a second approach, numerical techniques of contour dynamics as well as a finite-difference method for solving the full 2D vorticity equation are applied.

Before investigating the evolution of two-dimensional vortices in strain and shear flows, it is important to be first familiar with their dynamics in quiescent fluids. In previous work, the evolution characteristics of stable and unstable barotropic vortices in rotating fluids were examined experimentally by Kloosterziel & van Heijst (1991, 1992), whereas the dynamical structure of monopolar and dipolar vortices in stratified fluids was investigated by Flór & van Heijst (1994, 1996). The latter authors presented a diffusion model to describe the decay of monopolar vortices in a stratified fluid. Although in their experiments these pancake-like structures were observed to expand in the radial direction, only the vertical growth of the monopolar vortex was taken into account.

Hence, in chapter 2, the evolution of monopolar vortices in a stratified fluid is investigated experimentally, with more accurate measurement techniques than those applied by Flór & van Heijst (1994), and the observations are compared with an analytical model that accounts for both the increasing vertical thickness and the radial expansion of these vortex structures. It will be shown that the theoretical model provides a better description of the vortex evolution than the diffusion model presented by Flór and van Heijst (1996).

Chapter 3 will deal with the dynamics of these monopolar vortices in a strain flow. Stratified fluid experiments will show that the monopolar vortex is deformed by the ambient flow, and that the vortex is finally torn apart along one of the principal axes of the strain flow. The observed deformation of the vortex is compared with the vortex motion derived from Kida's analytical model, which is slightly adapted to account for the diffusive decay of vorticity.

In chapter 4, the kinematic properties of monopolar vortices in a strain flow are investigated. Dye-visualization experiments in stratified fluids will demonstrate the stripping of the vortex. Also the advection properties of individual tracers will be considered, both experimentally and numerically.

The evolution of monopolar vortices in an irrotational annular shear is discussed in chapter 5. The motivation of this study is that vortices may feel an irrotational shearing background flow when they are relatively far apart. In contrast to the behaviour of monopolar vortices in uniform strain or shear flows, the vortex evolution is characterized by the asymmetric shedding of thin filaments.

In chapter 6, the strain-induced deformation of dipolar vortices is studied in a stratified fluid. Depending on the direction of the strain flow, either a head-tail structure is formed or the dipole is broken into two monopolar vortices.

Finally, the main conclusions are given in chapter 7. It should be noted that chapters 2 through 6 have initially been written as an article for publication. Therefore, throughout this thesis, some repetition occurs concerning the description of general theory and methods.

Chapter 2

Decay of monopolar vortices in a stratified fluid

2.1 Introduction

Two-dimensional vortices play an important part in large-scale geophysical flow systems, such as the planetary atmospheres and the world's oceans. The most common type is the so-called monopolar vortex, which has a core of single-signed vorticity, and possibly a ring of oppositely-signed vorticity. This vortex structure has been observed in nature through satellite pictures, examples of which are the high and low pressure cells in the atmosphere, and oceanic eddies (e.g. warm-core Gulf Stream rings) as discussed by Robinson (1983). Likewise, laboratory experiments have revealed the occurrence of monopolar vortices in rotating as well as in stratified fluids; a recent overview on this topic is given by Hopfinger & van Heijst (1993).

An important question concerns the evolution of monopolar vortices. Based on their experimental observations related to cyclonic barotropic vortices in a rotating fluid, Kloosterziel & van Heijst (1992) have shown that the evolution of these column-shaped vortices is characterized by a steepening of the flow profiles and by a faster decay than expected from linear Ekman dynamics. These results could mainly be ascribed to the advection of relative vorticity by the interior Ekman circulation.

The decay of monopolar vortex structures in a stratified fluid was investigated by Flór & van Heijst (1996), henceforth referred to as F&vH. From their laboratory observations, the monopolar vortex appeared to have a flat pancake-like shape. Furthermore, the experimental results were compared with two decay models based on a viscously decaying Bessel vortex: in the first model, the (vertical) thickness of the vortex was assumed constant, whereas in the second model, the vertical growth of the vortex was taken into account. Although F&vH clearly observed a radial expansion of the vortex, the vortex's radius was assumed constant in both models.

In the present study, a decay model will be derived that accounts for both the increasing thickness and the radial expansion of the vortex. This extended decay model will

be compared with more accurate laboratory observations than those reported by F&vH. Monopolar vortices were generated in a stratified fluid with the same techniques as used by F&vH, either by a small spinning sphere or by the so-called tangential injection method, and the corresponding velocity fields were measured by tracking passive tracer particles. It will be shown that the extended decay model provides a better description of the vortex evolution than the diffusion models presented by F&vH.

This chapter is organized as follows. In section 2.2 a theoretical treatment of the extended decay model will be given, followed by a description of the experimental arrangement (section 2.3). Next, in section 2.4, the laboratory observations will be presented and a comparison will be made with the analytical model. Finally, a discussion of the results and some conclusions are given in section 2.5.

2.2 The extended decay model

Experimental observations by F&vH and Flór, van Heijst & Delfos (1995) have revealed that monopolar and dipolar vortices in a stratified fluid have a flat pancake-like shape. From a simple scaling analysis, vertical diffusion of vorticity proved to be more important than horizontal diffusion. Therefore, the horizontal size of the vortices was assumed constant as a first-order approximation. In the present study, the attention will be restricted to the monopolar vortex. The analysis of F&vH will be followed closely, but now the horizontal expansion of the vortex will be reckoned with in the theoretical model.

The monopolar vortex structure is assumed to be confined in a disc-shaped region, and the extended decay model will be restricted to the region near the mid-plane ($z = 0$), where the vorticity vectors are directed approximately vertically and the vortex tilting by the vertical shear is negligible. From a scaling analysis, similar to that of Riley, Metcalfe & Weissman (1981) and Lilly (1983), it was shown by F&vH that for a buoyancy-dominated flow, subject to the foregoing restraints, the three-dimensional vorticity equation is at lowest order in Ri^{-1} reduced to

$$\frac{\partial \omega}{\partial t} + J(\omega, \psi) = \nu \nabla_h^2 \omega + \nu \frac{\partial^2 \omega}{\partial z^2}, \quad (2.1)$$

with ω the vertical component of vorticity, ψ the stream function defined by $\mathbf{u}_h = -\mathbf{k} \times \nabla \psi$ (\mathbf{u}_h represents the horizontal velocity component), ν the kinematic viscosity, and ∇_h^2 the Laplace operator acting in horizontal directions. Here, the bulk Richardson number Ri is defined by $Ri = N^2 \sigma^2 / U^2$, with 2σ the typical thickness of the monopole and U a characteristic horizontal velocity scale. The Jacobian J can be written as

$$J(\omega, \psi) = \frac{1}{r} \frac{\partial \omega}{\partial r} \frac{\partial \psi}{\partial \theta} - \frac{1}{r} \frac{\partial \omega}{\partial \theta} \frac{\partial \psi}{\partial r}, \quad (2.2)$$

where (r, θ) are polar coordinates. Equation (2.1) implies that the horizontal motions are completely decoupled from the vertical motions.

When the disc-shaped region is allowed to diffuse both in horizontal and in vertical direction, the vorticity can be written as

$$\omega = \omega_{2D}(r, t)\Phi(z, t), \quad (2.3)$$

where $\omega_{2D}(r, t)$ represents any horizontal vorticity distribution satisfying the two-dimensional vorticity equation

$$\frac{\partial \omega_{2D}}{\partial t} + J(\omega_{2D}, \psi) = \nu \nabla_h^2 \omega_{2D}, \quad (2.4)$$

and $\Phi(z, t)$ is an amplitude function. By substitution of (2.3) in (2.1), one obtains a diffusion equation for the viscous decay of Φ :

$$\frac{\partial \Phi}{\partial t} = \nu \frac{\partial^2 \Phi}{\partial z^2}. \quad (2.5)$$

2.2.1 Horizontal diffusion

For axisymmetric vortex structures the Jacobian is identically zero ($J \equiv 0$), implying that any functional relationship between vorticity and stream function is possible. In that case the two-dimensional vorticity equation (2.4) can be written as (from now on, the subscripts $2D$ will be omitted):

$$\frac{\partial \omega}{\partial t} = \frac{\nu}{r} \frac{\partial}{\partial r} \left(r \frac{\partial \omega}{\partial r} \right). \quad (2.6)$$

F&vH approximated the horizontal flow of the monopolar vortices by the Bessel-vortex model, which is based on the linear relationship

$$\omega = k^2 \psi, \quad (2.7)$$

with k being a constant. Applying Poisson's equation, $\omega = -\nabla_h^2 \psi$, and assuming axisymmetry leads to the vorticity distribution given by

$$\omega = Ak^2 J_0(kr), \quad (2.8)$$

with J_0 the zeroth-order Bessel function of the first kind, and A a constant. Because F&vH only considered the core of the vortex, the solution (2.8) was truncated at the first zero of J_0 , i.e. at $r = R$ for which $J_0(kR) = 0$, yielding the dispersion relation $kR = 2.40$. The vortex thus obtained is defined on a disc of radius R containing only single-signed vorticity. Although horizontal diffusion of vertical vorticity was taken into account by F&vH, the radius of the vortex was assumed constant (i.e. k is constant). This means that the discontinuity in $\partial\omega/\partial r$ at $r = R$ was ignored.

Detailed measurements described in the present study will show, however, that the observed vortices tend to grow in horizontal size. Moreover, their net circulation will appear to be zero, i.e. these vortices are isolated. A possible model describing isolated vortex structures is the so-called Gaussian vortex model, which is often applied to laboratory

vortices, such as stirring-induced vortices in rotating fluids (see Hopfinger & van Heijst (1993)), and oceanic vortices (see Simpson, Dickey & Koblinsky (1984)). In this model, the scaled expressions for the vorticity $\omega^* = \omega R/V$ and the azimuthal velocity $v_\theta^* = v_\theta/V$ (with R being a typical length scale and V a characteristic velocity scale) are given by

$$\omega^* = [1 - \eta^2] \exp(-\eta^2) \quad (2.9)$$

$$v_\theta^* = \frac{1}{2}\eta \exp(-\eta^2), \quad (2.10)$$

with $\eta = r/R$ the scaled radial distance. Obviously, the Gaussian vortex is characterized by continuous vorticity and velocity distributions.

The scaled stream function ψ^* can be derived from (2.10), which yields:

$$\psi^* = \frac{1}{2} \exp(-\eta^2). \quad (2.11)$$

(The Gaussian vortex owes its name to the Gaussian shape of the stream function distribution). Combination of (2.9) and (2.11) leads to the functional relationship F between ω^* and ψ^* :

$$\omega^* = F(\psi^*) = 2\psi^* [1 + \ln 2\psi^*]. \quad (2.12)$$

In order to find a time-dependent solution that accounts for the horizontal diffusion of vorticity, and that will give an expression for the radial growth of the vortex, the Gaussian vortex model is extended by assuming a similarity solution of the form

$$\omega = f(t)g(\eta), \quad (2.13)$$

where $f(t)$ is an arbitrary function of time, and $g(\eta)$ represents the solution (2.9). The choice of a self-similar solution is obvious since the present problem has no natural length or time scales (the flow is assumed to be unbounded).

From dimensional considerations the length scale R can only be a function of ν and t , and is therefore written as

$$R = \beta\sqrt{\nu t}, \quad (2.14)$$

with β a constant, which still has to be determined.

Substitution of (2.13) in (2.6), and using (2.14), leads to $\beta = 2$ and $f(t) \sim 1/t^2$, so that the (dimensional) time-dependent solutions of vorticity and azimuthal velocity are given by

$$\omega(r, t) = \frac{C}{(\nu t)^2} \left[1 - \frac{r^2}{4\nu t} \right] \exp\left(-\frac{r^2}{4\nu t}\right) \quad (2.15)$$

and

$$v_\theta(r, t) = \frac{Cr}{2(\nu t)^2} \exp\left(-\frac{r^2}{4\nu t}\right), \quad (2.16)$$

respectively, where C is a constant. This time-dependent expression for the azimuthal velocity was also found by Taylor (1918) using a different approach. Apparently, the profiles (2.9) and (2.10) can be considered as a 'snap-shot' of the decaying Gaussian vortex.

It can be derived from (2.10) that the azimuthal velocity reaches a maximum at $\eta = 1/\sqrt{2}$. When R_m is defined as the radial position of peak velocity, it follows from (2.14) that

$$R_m = \sqrt{2\nu t}, \quad (2.17)$$

where t can be considered as the time required by the vortex to attain a radius R_m . Following Taylor (1918), this will be called the ‘age’ of the vortex.

As can be derived from the above equations, at time $t = 0$, both ω and v_θ have infinite values and the radius of the vortex is zero, which is not the case in reality. Therefore, it will be assumed that initially, the vortex already has a finite vorticity and velocity distribution corresponding with an initial ‘age’ t_0 . By applying the transformation $t \rightarrow t' + t_0$ (and omitting the primes), the vorticity is given by

$$\omega(r, t) = \frac{C}{\nu^2(t + t_0)^2} \left[1 - \frac{r^2}{4\nu(t + t_0)} \right] \exp\left(-\frac{r^2}{4\nu(t + t_0)}\right), \quad (2.18)$$

and the expression for R_m can be written as

$$R_m^2 = R_0^2 + 2\nu t, \quad (2.19)$$

where $R_0 (= \sqrt{2\nu t_0})$ represents the initial radius of the vortex.

2.2.2 Vertical diffusion

As F&vH did, it is assumed that initially the vorticity is confined to a thin region according to $\Phi(z, 0) = \Phi_0\delta(z)$, with δ the Dirac delta function. The solution of the vertical diffusion equation (2.5) is then given by

$$\Phi = \frac{\Phi_0}{\sqrt{\nu t}} \exp\left(-\frac{z^2}{4\nu t}\right). \quad (2.20)$$

Although this singular initial condition cannot be satisfied in the actual flow, it is assumed that the thickness of the vortex at $t = 0$ is relatively small, and that at later times (2.20) still gives a reasonable description of the finite vertical vorticity distribution.

The complete solution for the three-dimensional evolution of the vertical vorticity, which will further be referred to as the ‘extended decay model’, is then given by

$$\omega = \omega_{2D}(r, t) \frac{\Phi_0}{\sqrt{\nu t}} \exp\left(-\frac{z^2}{4\nu t}\right), \quad (2.21)$$

with ω_{2D} the horizontal distribution of vertical vorticity (2.18) according to the time-dependent Gaussian vortex model. Note, however, that the extended decay model is restricted to a thin region around the mid-plane $z = 0$.

The decay of maximum (vertical) vorticity ω_m can be obtained from (2.21) by setting $r = z = 0$, which leads to

$$\omega_m = \frac{C}{\nu^{5/2}(t + t_0)^2\sqrt{t}}, \quad (2.22)$$

where the transformation $C\Phi \rightarrow C'$ has been applied and the prime has been omitted.

2.3 Experimental arrangement

The laboratory experiments were performed in a perspex tank (with horizontal dimensions 1×1 m and a depth of 0.3 m), which was filled with two layers of salt solution, each having a different density. Owing to vertical mass diffusion of salt, a linear density distribution was formed (within a layer of approximately 10 cm thickness) near the mid-plane of the tank after a few days. However, the diffusion of mass is believed to have no significant influence during the evolution of a typical experiment. The depth of the fluid was about 26 cm, and the buoyancy frequency N of the stratification near the mid-plane was varied between 2.3 and 2.9 rad s^{-1} . Here, N is defined by $N = (-g/\bar{\rho} \, d\rho/dz)^{1/2}$, with g the gravitational constant, $\bar{\rho}$ the mean density, and $d\rho/dz$ the density gradient in vertical direction.

Two different forcing techniques were used to generate monopolar vortices. In both cases, the forcing device was positioned at the mid-level of the tank, and the time at which the forcing was stopped was taken as $t = 0$ s.

According to the first generation method, a small sphere (with diameter 2.5 cm) was spun about its vertical axis. The rotation speed Ω_s was either set to 150 or 300 rpm, and the forcing period δt was varied between 5 and 15 s. During the forcing, a boundary layer is present at the surface of the sphere, in which fluid is accelerated and swept radially outward near the sphere's equator. Hence, a turbulent region is formed, which moves away horizontally from the sphere. After the forcing was stopped, the sphere was carefully raised and removed from the tank. Shadowgraph visualizations have shown that, in the next stage, the turbulent region collapses under gravity, and a laminar horizontal vortex motion is formed (see F&vH).

As a second method, fluid was injected horizontally along the inner wall of an open thin-walled cylinder (with inner diameter 9.8 cm, thickness 0.1 cm and height 3 cm). The injection nozzle (with diameter 0.6 cm) was connected parallel to the inner wall of the cylinder, and the density of the injected fluid was taken equal to that of the ambient fluid at the injection level. A computer-driven injection mechanism was used to control the injection parameters: the injection rate Q was varied between 1.1 and 2.2 ml s^{-1} , and the forcing period δt ranged from 20 to 60 s. Care was taken that during the injection the motion remained confined within the cylinder. Typically 30 s after the forcing was stopped, an axisymmetric swirling flow was present and the cylinder was carefully lifted. As from now, this generation technique is referred to as the tangential-injection method.

Horizontal size oscillations, owing to internal wave motions, inevitably emerge during and shortly after the forcing and lifting of either of the forcing devices. However, typically 1 min after the device was raised these internal waves could no longer be observed by eye, and they are hence believed to play an insignificant role in the subsequent stage of the experiment.

In order to obtain quantitative information about the horizontal flow field, small polystyrene particles of density 1.04 g cm^{-3} were added to the fluid at the mid-level of the tank. The tracer particles were distributed within a layer of typically 1 cm thickness and they were assumed to follow the fluid without affecting the flow itself.

The motion of the particles was monitored by video camera mounted at some distance

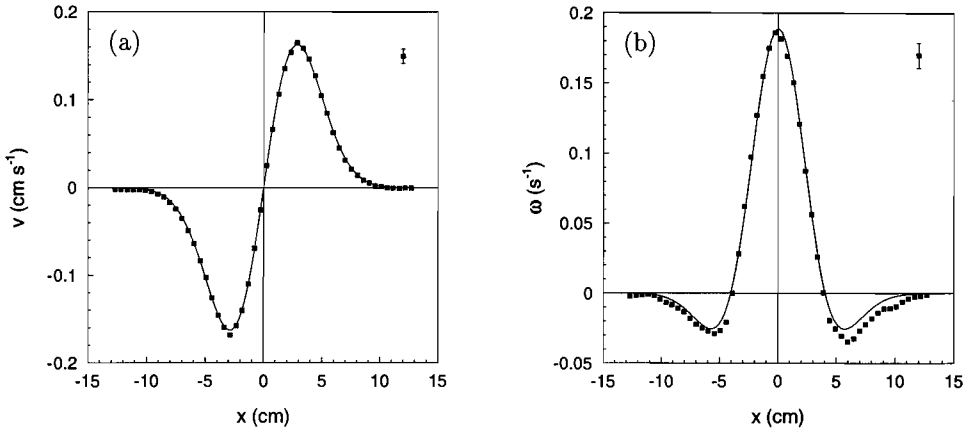


FIGURE 2.1: The radial cross-sectional distribution of (a) the velocity v directed perpendicularly to the cross-section and (b) the vorticity ω of a typical monopolar vortex generated by the spinning sphere, 180 s after the forcing was stopped. The experimental data (denoted by squares) are least-square fitted with (2.9) and (2.10) of the Gaussian vortex model. Experimental parameters: $\Omega_s = 150$ rpm, $\delta t = 5$ s and $N = 2.9$ rad s $^{-1}$.

above the tank. Afterwards, the video images were digitized and processed by the image analysis system *DigImage* (see Dalziel (1992)). A particle-tracking algorithm was used to determine the time-evolution of the particle positions and to calculate the local velocities. In the next stage, the velocity field was calculated at the mesh points of a rectangular grid of 30×30 grid points by a spline interpolation method (see Paihua Montes (1978) or Nguyen Duc & Sommeria (1988)). From this interpolated velocity field, the vorticity ω and the stream function ψ could be evaluated in each grid point by numerical differentiation and integration, respectively. The positive circulation Γ^+ and negative circulation Γ^- were obtained by taking the discrete surface integral over the positive and negative vorticity values, respectively.

2.4 Results

2.4.1 Cross-sectional distributions of velocity and vorticity

In figure 2.1(a,b) typical cross-sectional distributions are shown of a vortex generated by the spinning sphere. The velocity v and the vorticity ω are plotted along a line (with spatial coordinate x) through the centre (defined by $x = 0$) of the vortex. This velocity v corresponds with the velocity component directed perpendicularly to the cross-section and it has the same magnitude as the azimuthal velocity v_θ for perfectly axisymmetric flow. The experimental data are denoted by squares, the data in between the grid points being obtained by bilinear interpolation. The solid curves, corresponding to (2.9) and

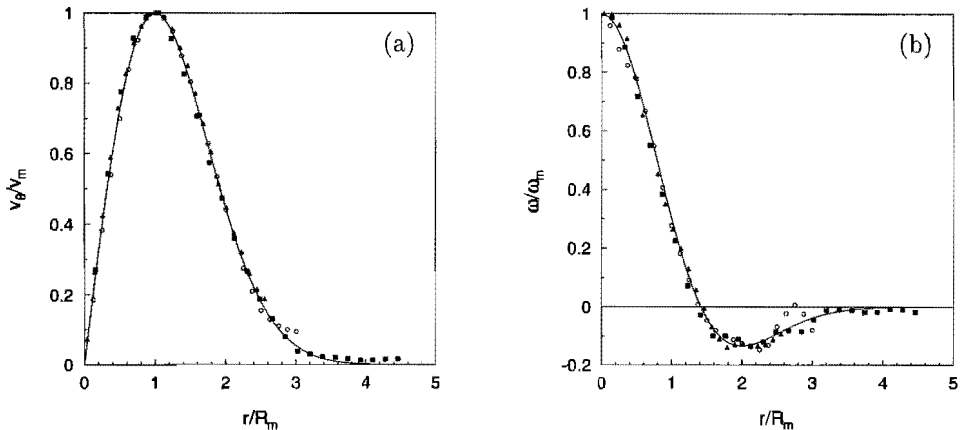


FIGURE 2.2: Graphs showing (a) the scaled azimuthal velocity and (b) the scaled vorticity profiles of a vortex generated by the spinning sphere. The measured profiles correspond with three different times, viz. at $t = 120$ s (squares), 480 s (circles), and 720 s (triangles). The azimuthal velocity v_θ and the vorticity ω have been scaled with their maximum values v_m and ω_m , respectively, whereas the radial coordinate r has been scaled with the position of maximum velocity R_m . The maximum values decreased from $v_m = 0.55$ cm s $^{-1}$ and $\omega_m = 0.69$ s $^{-1}$ at $t = 120$ s to $v_m = 0.05$ cm s $^{-1}$ and $\omega_m = 0.04$ s $^{-1}$ at $t = 720$ s, respectively. The time evolution of R_m^2 is shown in figure 2.7(a). The measured profiles are compared with the velocity and vorticity profiles according to the Gaussian vortex model (denoted by solid lines). Experimental parameters: $\Omega_s = 150$ rpm, $\delta t = 15$ s and $N = 2.9$ rad s $^{-1}$.

(2.10) of the Gaussian vortex model, have each been least-square fitted to the observed data. Although there is some difference at the extrema of the profiles, a good agreement between the experimental data and the fitted curves is visible; the deviations are mainly caused by small deviations from axisymmetry. It is clear that the absolute velocity has a maximum and falls off to zero quite rapidly at larger radii. Obviously, the vortex has a core of positive vorticity, which is maximum in the centre, while it is enclosed by a ring of negative vorticity.

According to the time-dependent Gaussian vortex model, all profiles at different times should collapse onto a single curve if the velocity and vorticity profiles are appropriately scaled. In figure 2.2 the measured distributions (indicated by markers) of a vortex generated by the spinning sphere are presented at three different times, varying from $t = 2$ min to $t = 12$ min (the forcing was stopped at $t = 0$ s). For each profile, the azimuthal velocity and the vorticity have been scaled by their maximum values v_m and ω_m , respectively, whereas the radial coordinate has been scaled by the position of peak velocity R_m . It is seen that, apart from some scatter in the outer region of negative vorticity, all curves coincide very well. Hence, the measured velocity and vorticity profiles are self-similar in time, as expected from the time-dependent Gaussian vortex model. Also, the scaled velocity and vorticity

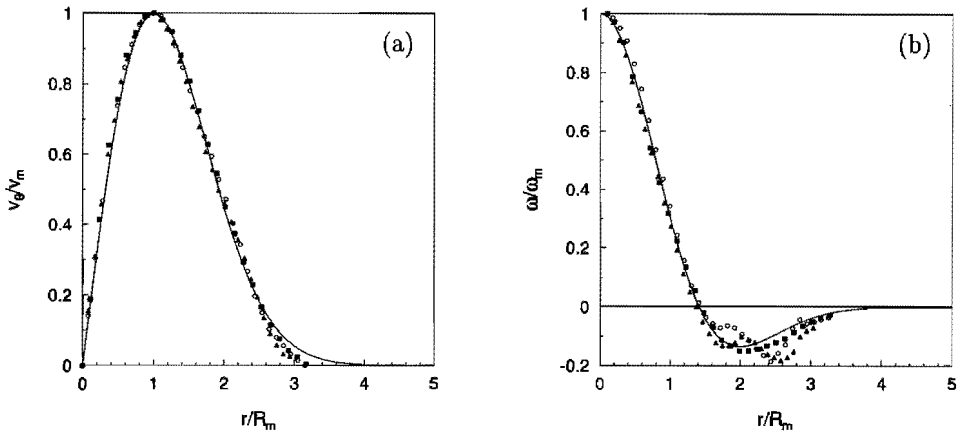


FIGURE 2.3: Graphs showing (a) the scaled azimuthal velocity and (b) the scaled vorticity profiles of a vortex generated by the tangential-injection method. The measured profiles correspond with three different times, viz. at $t = 380$ s (squares), 740 s (circles) and 920 s (triangles). The azimuthal velocity v_θ and the vorticity ω have been scaled as in figure 2.2. The maximum values decreased from $v_m = 0.060$ cm s $^{-1}$ and $\omega_m = 0.05$ s $^{-1}$ at $t = 380$ s to $v_m = 0.016$ cm s $^{-1}$ and $\omega_m = 0.01$ s $^{-1}$ at $t = 920$ s, respectively. The profiles according to the Gaussian vortex model are denoted by solid lines. Experimental parameters: $Q = 1.7$ ml s $^{-1}$, $\delta t = 40$ s and $N = 2.7$ rad s $^{-1}$.

profiles as obtained from the Gaussian model (solid lines) closely match the observed profiles. Similar results were obtained for a vortex generated by the tangential-injection method, which can be inferred from figure 2.3. Apparently, both generation techniques yield the same flow profiles.

The measured velocity profiles obtained by F&vH were less steep for large radii (typically $r > 2R_m$) and showed much more scatter than the profiles presented in figures 2.2(a) and 2.3(a). As a result, in their experiments the ring containing negative vorticity was wider and weaker in amplitude, and self-similarity was only present in the core of the vortex. Since the present results, shown in figures 2.1–2.3, are in good agreement with the time-dependent Gaussian vortex model, the discrepancy with the results obtained by F&vH is attributed to the different measurement techniques that were used, as will be discussed in section 2.5.

2.4.2 The (ω, ψ) -relationship

The functional relation between the scaled vorticity ω^* and the scaled stream function ψ^* is shown in figure 2.4 for four consecutive times. In this case, the vortex was generated by the spinning sphere. Each measured data point (ω^*, ψ^*) corresponds to one of the 900 mesh points of the rectangular grid. The vorticity and stream function have been scaled

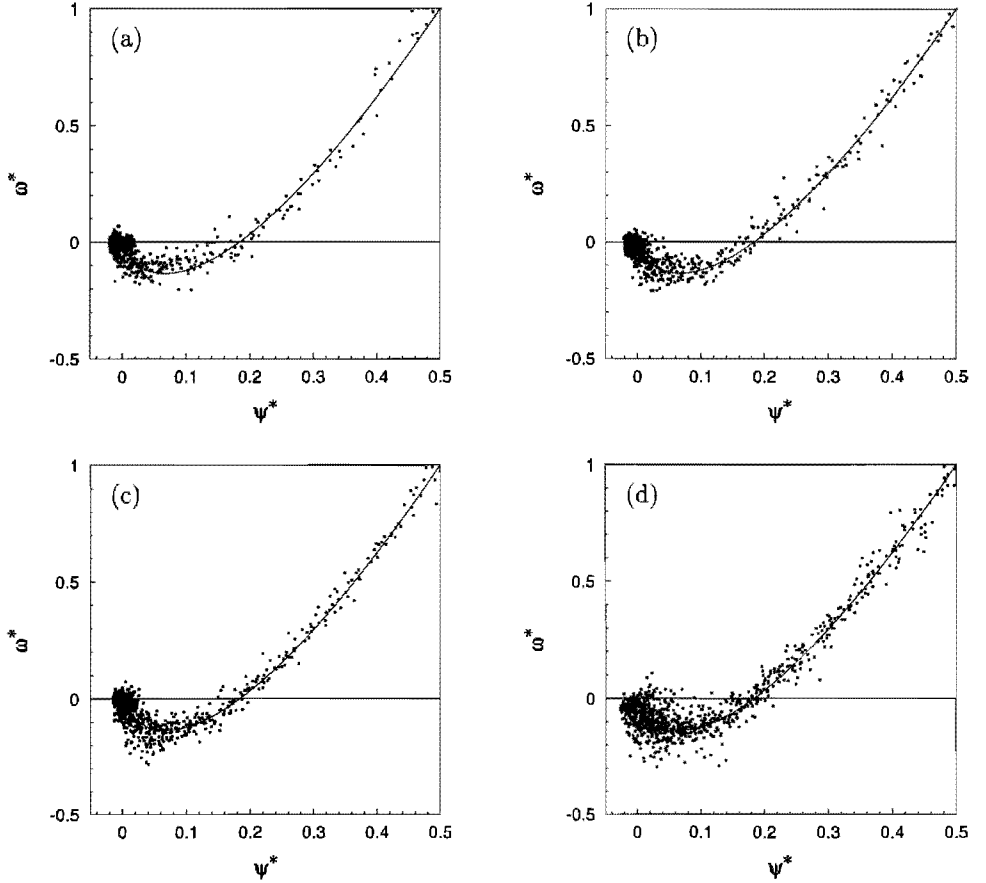


FIGURE 2.4: The scaled vorticity ω^* versus the scaled stream function ψ^* at successive times after the forcing was stopped: (a) $t = 120$ s, (b) 300 s, (c) 420 s and (d) 960 s. The vorticity and stream function have been scaled by ω_m and $2\psi_m$, respectively. The maximum velocity and vorticity range from $v_m = 0.55$ cm s $^{-1}$, $\omega_m = 0.69$ s $^{-1}$ at $t = 120$ s to $v_m = 0.03$ cm s $^{-1}$ and $\omega_m = 0.02$ s $^{-1}$ at $t = 960$ s, respectively. Further details about the scaling can be found in the text. The observed data (denoted by squares) are compared with the (ω^*, ψ^*) -relationship (2.12) according to the Gaussian vortex model. Experimental parameters: see figure 2.2.

with ω_m and $2\psi_m$, respectively, in such a way that $\psi^* = 0$ corresponds to the mean stream function value of the data points clustered near $\omega = 0$. The obtained (ω^*, ψ^*) -relation, also called ‘scatter plot’, can be interpreted as follows: the approximately linear branch with $\omega^* > 0$ represents the core of the vortex, whereas the negative part of the scatter plot corresponds to the ring of negative vorticity. The observed data are compared with the (ω^*, ψ^*) -relation (2.12) of the Gaussian vortex (solid curve), and despite some scatter in the experimental data, for each graph a good agreement is obtained. The scatter is probably caused by experimental errors and radial transport of fluid, which will be discussed later. In figure 2.4(d), the scatter appears to be large compared to the deviations in (ω^*, ψ^*) -plots at earlier times, especially near the ring of negative vorticity. However, this is merely a result of the scaling process, which blows up small deviations when the maximum vorticity is relatively small. It is clear from figure 2.4 that the measured (ω^*, ψ^*) -relationships are self-similar in time. Scatter plots of vortices generated by the tangential-injection method revealed similar results as discussed above.

Laboratory observations by F&vH also showed a nearly linear (ω, ψ) -relationship in the core of the vortex, but the ring of oppositely signed vorticity was distributed over a wider region and was smaller in amplitude compared to the results in figure 2.4. This contradiction may again be ascribed to the measurement technique used by F&vH (see section 2.5).

Because of the nearly linear (ω, ψ) -relationship in the core of the vortex, each scatter plot was least-square fitted for $\omega > 0$ with the linear relation $\omega = k^2\psi$ (see (2.7)). According to the Bessel-vortex model $kR_m = 1.84$, which was checked through multiplication of each obtained k -value by the corresponding radius of peak velocity R_m as determined from the measured velocity profiles. The values of kR_m are plotted against time in figure 2.5(a) for a typical experiment and appear to have a mean value of 1.79 ± 0.01 , which is in agreement with the mean value 1.79 ± 0.06 found by F&vH using the same procedure. However, both obtained values are systematically below the model-value $kR_m = 1.84$ (dashed line).

In order to derive a similar value for kR_m based on the Gaussian vortex model, the average slope $(k^*)^2$ of the theoretical (ω^*, ψ^*) -relation (2.12) was calculated for $\omega^* > 0$ (see figure 2.5(b)) by

$$(k^*)^2 = \frac{\omega^*(\psi_c^*) - \omega^*(\psi_s^*)}{\psi_c^* - \psi_s^*}, \quad (2.23)$$

with ψ_c^* ($= 0.5$) and ψ_s^* ($= 0.18$) corresponding to the centre of the vortex and the radius at which vorticity changes sign, respectively. Since $\omega^*(\psi_c^*) = 1$ and $\omega^*(\psi_s^*) = 0$, it follows that $k^* = kR_m = 1.78$ (solid line in figure 2.5(a)), which is in very good agreement with the experimental observations. This result was obtained for all experiments.

2.4.3 The net circulation

In order to examine whether the observed vortices are isolated (i.e. have no net circulation), for each time the negative circulation Γ^- is plotted against the positive circulation Γ^+ for the vortex generated by the spinning sphere (figure 2.6). Clearly, the data points coincide

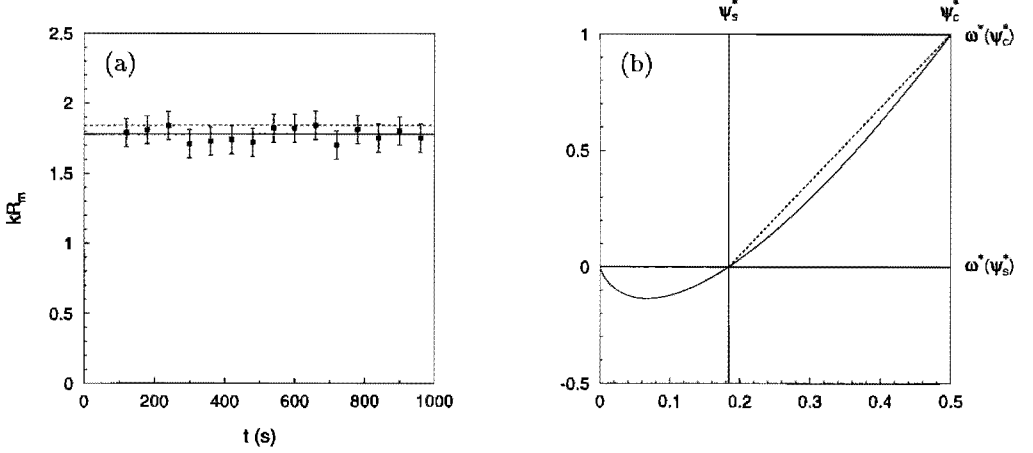


FIGURE 2.5: (a) Measured time evolution of kR_m (denoted by squares) of a vortex generated by the spinning sphere. According to the Bessel vortex model $kR_m = 1.84$ (dashed line), whereas the Gaussian vortex model yields $kR_m = 1.78$ (solid line). Experimental parameters as in figure 2.2. (b) Definition of the slope $(k^*)^2$ (dashed line) according to (2.23). The solid line corresponds to relation (2.12).

very well with the solid line ($\Gamma^- = \Gamma^+$), which confirms that the vortex generated by the spinning sphere is indeed isolated, as implied by the Gaussian vortex model. The vortices generated by the tangential-injection method proved to be isolated as well.

2.4.4 Comparison with the extended decay model

In figure 2.7(a) the measured values of R_m^2 are plotted as a function of time for three different experiments in which the vortices were generated by the spinning sphere, and for each experiment a good linear relationship can be observed. Each data set was least-square fitted with the relation $R_m^2 = R_0^2 + \alpha t$, where R_0 represents the initial radius of the vortex, and α is the radial expansion rate, which according to (2.19) should be equal to $2\nu = 1.94 \times 10^{-2} \text{ cm}^2 \text{ s}^{-1}$ ($\nu = 0.97 \times 10^{-2} \text{ cm}^2 \text{ s}^{-1}$ for a salt solution of density $\rho = 1.04 \text{ g cm}^{-3}$ at a temperature of 24°C). The experimental parameters as well as the obtained values for R_0 and α are listed in table 2.1 for five different ‘spinning sphere’-experiments that were analysed. From this table it can be inferred that the values of α approach the theoretical expansion rate reasonably well. However, in all cases the vortex radius expands somewhat faster than predicted by the extended decay model, which is most likely due to radial advection caused by the initial acceleration of the fluid during the forcing. This conjecture is supported by the observation that larger values of α are obtained when either the rotation speed Ω_s or the forcing period δt is increased.

Similar expansion rate values were obtained for vortices generated by the tangential-injection method, as can be deduced from table 2.2. The faster expansion rate is probably

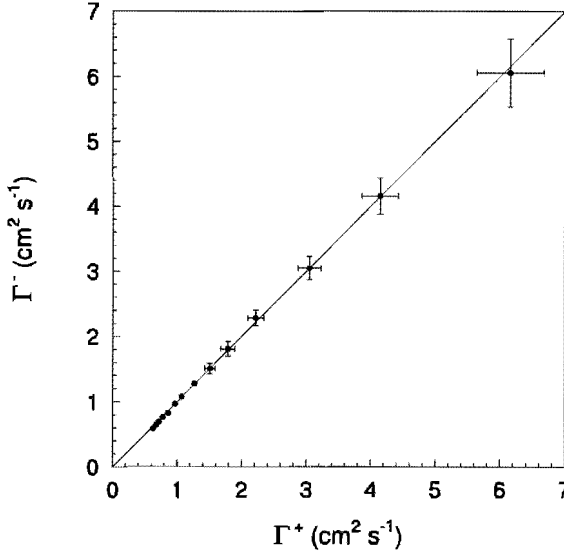


FIGURE 2.6: Negative circulation Γ^- versus positive circulation Γ^+ of a vortex generated by the spinning sphere. The solid line corresponds with an isolated vortex, for which $\Gamma^- = \Gamma^+$. Experimental parameters: $\Omega_s = 150$ rpm, $\delta t = 5$ s and $N = 2.9$ rad s⁻¹.

due to the collapse of the injected layer of uniform density, which intrudes radially into the quiescent ambient fluid after the lifting of the cylinder.

In their study, F&vH attributed the main part of the horizontal growth of the vortex to entrainment of ambient fluid. However, close inspection of their results reveals that the radial expansion rate is of the same order as predicted by the extended decay model. Although entrainment of ambient fluid might lead to a faster growth of the vortex size, the above results show that the main part of the horizontal expansion can be ascribed to horizontal diffusion.

From the initial radius R_0 , the initial age t_0 of the vortex was calculated by applying the relation $R_0^2 = \alpha t_0$. Table 2.1 shows that for the vortices generated by the spinning sphere, both R_0 and t_0 become larger with increasing rotation speed and forcing period, although for $\Omega_s = 150$ rpm the dependence on the forcing period is not so clear. Again, these results can be understood by considering the radial motion of fluid during the forcing: a larger forcing period means that initially the turbulent intrusion near the sphere's equator can travel over a larger distance, and consequently the size of the vortex at $t = 0$ increases. (Note that the forcing was stopped at $t = 0$). Likewise, a larger rotation speed leads to a faster growth of the intrusion in horizontal direction, and thus to a larger initial radius of the vortex. These arguments are supported by a scaling analysis which reveals that one of the parameters that R_0 and t_0 should depend on is the number of revolutions of the sphere $\Omega_s \delta t$.

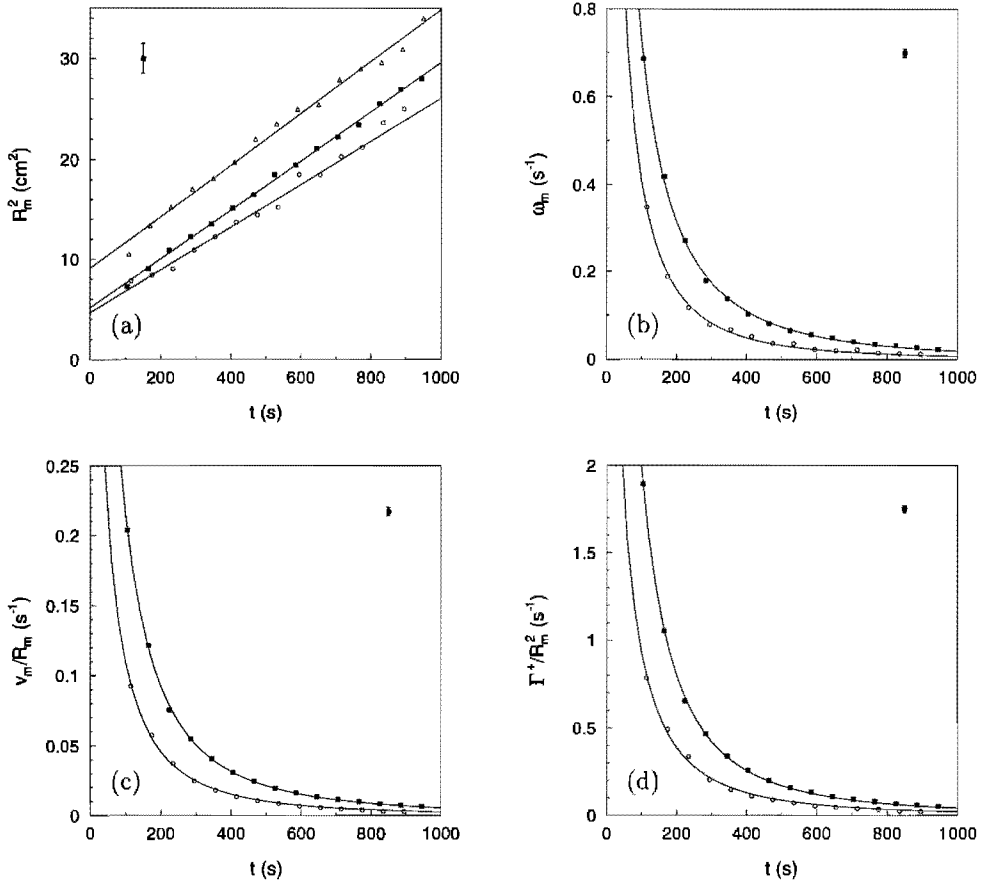


FIGURE 2.7: (a) Graph showing the value of R_m^2 as a function of time for three different experiments: circles, exp. 1; squares, exp. 3; triangles, exp. 5. The values of (b) maximum vorticity ω_m , (c) v_m/R_m and (d) Γ^+/R_m^2 are plotted against time. The experimental data, indicated by circles (exp. 1) and squares (exp. 3), are least-square fitted with (2.22) of the extended decay model (solid lines). The vortices were generated by the spinning sphere. Experimental parameters: see table 2.1.

Exp. No.	Ω_s (rpm)	δt (s)	α ($\times 10^{-2}$ cm ² s ⁻¹)	R_0 (cm)	$t_0^{(R_0)}$ (s)	$t_0^{(\omega)}$ (s)	$t_0^{(v_m/R_m)}$ (s)	$t_0^{(\Gamma^+/R_m^2)}$ (s)
1	150	5	2.1 ± 0.1	2.2 ± 0.2	218 ± 36	186 ± 24	233 ± 30	233 ± 23
2	150	10	2.3 ± 0.1	2.2 ± 0.1	211 ± 27	216 ± 16	255 ± 19	241 ± 14
3	150	15	2.4 ± 0.1	2.3 ± 0.1	211 ± 26	263 ± 15	254 ± 15	209 ± 9
4	300	5	2.4 ± 0.1	2.4 ± 0.1	248 ± 28	233 ± 25	276 ± 31	234 ± 20
5	300	10	2.6 ± 0.1	3.0 ± 0.1	355 ± 27	425 ± 39	414 ± 40	292 ± 21

TABLE 2.1: Experimental parameters (columns 2–3) and results obtained from the extended decay model for five different laboratory experiments. In each experiment the sphere was given a rotation speed Ω_s with a forcing period δt . The parameters α and R_0 are obtained from the relation $R_m^2 = R_0^2 + \alpha t$ (see text). The last four columns provide the initial ‘ages’ of the vortex obtained from fits with experimental data.

Exp. No.	Q (ml s ⁻¹)	δt (s)	V (ml)	α ($\times 10^{-2}$ cm ² s ⁻¹)	R_0 (cm)	$t_0^{(R_0)}$ (s)
6	2.2	20	44	2.1 ± 0.2	1.8 ± 0.4	143 ± 63
7	1.1	60	67	2.0 ± 0.3	2.2 ± 0.4	254 ± 114
8	1.7	40	67	2.3 ± 0.2	2.4 ± 0.3	240 ± 62
9	1.7	60	100	2.0 ± 0.3	3.0 ± 0.2	444 ± 116

TABLE 2.2: Experimental parameters (columns 2–4) and results obtained from the extended decay model for four different laboratory experiments. The vortices were generated by the tangential injection method with a given injection rate Q and forcing period δt . The parameters α and R_0 are obtained from the relation $R_m^2 = R_0^2 + \alpha t$ (see text).

In the same way, vortices generated by the tangential-injection method show that both R_0 and t_0 depend on the injection rate Q and the injection period δt , as can be inferred from table 2.2. A similar scaling analysis as applied to the spinning sphere relates R_0 and t_0 to the injected volume of fluid $V (= Q\delta t)$, which seems to be in agreement with the observations (see table 2.2).

According to the extended decay model, the maximum vorticity ω_m , maximum azimuthal velocity v_m and positive circulation Γ^+ are related by: $\omega_m \sim v_m/R_m \sim \Gamma^+/R_m^2$. Therefore, v_m and Γ^+ have been appropriately scaled by R_m . Figures 2.7(b), (c) and (d) show the temporal decay of ω_m , v_m/R_m and Γ^+/R_m^2 , respectively, for two different ‘spinning-sphere’-experiments. The observed data were least-square fitted by (2.22) of the extended decay model (solid lines), with the constant C and the initial age t_0 taken as free parameters, and a very good agreement was obtained for each graph. The initial ages $t_0^{(\omega)}$, $t_0^{(v_m/R_m)}$ and $t_0^{(\Gamma^+/R_m^2)}$, obtained from fits as shown in figure 2.7(b), (c) and (d), are listed in table 2.1. For each experiment these values are of the same order as the initial age $t_0^{(R_0)}$. Similar results were obtained for vortices generated by the tangential-injection method.

2.5 Discussion and conclusions

Stratified fluid experiments described in this chapter have demonstrated that the instantaneous horizontal flow field of the observed monopolar vortices is in good agreement with the time-dependent Gaussian vortex model. The vortices were generated either by a small spinning sphere or by the tangential-injection method.

Detailed measurements of the mid-plane flow field revealed that these vortices are characterized by a core of single-signed vorticity and a ring of oppositely-signed vorticity, and that their net circulation is zero. The measured cross-sectional distributions of vorticity and azimuthal velocity closely match the theoretical profiles. The observed (ω, ψ) -relationship is in good agreement with that of a Gaussian vortex, and appears to be approximately linear in the vortex core, but highly nonlinear in the outer region of the vortex.

In the paper of F&vH the horizontal flow field was modelled by the Bessel vortex, which is essentially non-isolated. Consequently, only good agreement with the experimental data was obtained in the core of the vortex. Moreover, in the outer region of the vortex the measured velocity and vorticity distributions differed from the laboratory observations presented in this chapter, which was also true for the negative branch in the scatter plots. Since the present experimental results are in good agreement with the time-dependent Gaussian vortex model, it is believed that this discrepancy can be ascribed to the measurement technique that was used by F&vH. In their case, the horizontal velocity field was obtained from streak photographs, which had to be digitized manually on a digitization tablet (see Flór & van Heijst (1994) for more details), whereas in the present study the velocity fields were obtained by a more accurate method in which video images of passive tracer particles were digitized and linked together by the computer-controlled particle-tracking method.

In an analytical study by Kloosterziel (1990), the Gaussian vortex appeared to be a member of a one-parameter family of self-similar solutions of the radial diffusion equation.

Moreover, the Gaussian vortex was used in a numerical instability study by Carton, Flierl & Polvani (1989). From their analysis it turned out that the Gaussian vortex was unstable in inviscid flows, so one might wonder why the observed Gaussian vortices are stable. Inviscid instability, however, is not a guarantee for instability in a viscous medium, and given the fact that the Gaussian vortex corresponds to the edge of the instability regime, it is not unlikely that the Gaussian vortex is stable in a viscous fluid. Apparently the growth of the perturbations is damped by horizontal and vertical diffusion.

In the present study, the decay of maximum vorticity and peak velocity, as well as the evolution of positive circulation could be accurately fitted with the extended decay model, which is based on both horizontal diffusion (described by the time-dependent Gaussian vortex model) and vertical diffusion of vorticity. The radius of the vortex appeared to increase in time, which could mainly be assigned to horizontal diffusion. A small part of the horizontal expansion of the vortex was caused by radial advection of fluid, which can be ascribed to the generation techniques, and possibly by entrainment of ambient fluid.

In their diffusion models, F&vH did not allow for the radial growth of the vortex, and the observed horizontal expansion was mainly attributed to entrainment of ambient fluid. The extended decay model shows, however, that horizontal diffusion cannot be neglected to describe the radially increasing vortex size. Since the extended decay model is in good agreement with the observations, and can also explain the radial growth of the vortex, it gives a better description of the vortex evolution than the diffusion models presented by F&vH.

Chapter 3

Dynamics of monopolar vortices in a strain flow

3.1 Introduction

In this chapter, the dynamics of monopolar vortices in a strain flow will be examined based on laboratory experiments which have been performed in a stratified fluid. The strain flow was established by four rotating horizontal discs, whereas the monopolar vortex was generated by a small spinning sphere. Quantitative information about the flow field was obtained by tracking passive tracer particles.

The laboratory observations will be compared with Kida's analytical model (see Kida (1981)), which will be extended to account for the observed decay of vorticity. As a second approach, the full two-dimensional vorticity equation will be solved numerically by a finite-difference method, and the corresponding results will be compared with the laboratory observations.

This chapter is organized as follows. After the description of the experimental set-up in section 3.2, the measured characteristics of the strain flow and the monopolar vortex will be presented in section 3.3 and section 3.4, respectively. In section 3.5, the observed evolution of monopolar vortices in strain flows is discussed, and in section 3.6 a comparison is made with the results obtained from the theoretical models. Finally, in section 3.7, the experimental and theoretical findings of this study will be discussed and the main conclusions will be given.

3.2 Experimental arrangement

The experiments were carried out in a square tank of inner dimensions $100 \times 100 \times 30$ cm (length \times width \times depth), which was filled with a two-layer salt stratification. Typically after a few days, an approximately linear density stratification was formed near the mid-plane of the tank within a horizontal layer of about 10 cm thickness. The fluid depth was about 26 cm and the buoyancy frequency N at mid-depth was varied between 1.6 and 3.4

rad s⁻¹.

The strain flow was generated by four rotating horizontal discs (diameter 10 cm, thickness 0.5 cm), which were positioned at the corners of a square in the mid-plane of the tank (see figure 3.1). The diagonal distance D between the centres of the discs was either 40 or 50 cm, and the discs were rotated continuously at a constant angular speed Ω_d in the directions indicated in figure 3.1(a). The system was driven by a single motor to ensure each disc of having the same rotation speed.

Typically one hour after the start of the strain flow forcing, a monopolar vortex was generated in the centre of the mid-plane by a small sphere (with a diameter of 2.5 cm) spinning about its vertical axis. For the experiments presented in this chapter, the rotation speed of the sphere, Ω_s , was varied between 150 and 279 rpm, and the corresponding forcing period ranged from 5 to 15 s. After the spinning was stopped (at $t = 0$ s), the sphere was carefully lifted and removed from the tank.

In order to determine the horizontal velocity field, small polystyrene particles of density 1.04 g cm^{-3} were added to the fluid at the mid-level of the tank. The passive tracers were monitored continuously by a video camera which was mounted above the tank. Afterwards, the particles in successive digitized video images were linked together, using the image analysis system *DigImage* developed by Dalziel (1992). In this way, the local velocity vectors could be determined at successive times. Next, the measured velocity vectors were calculated at the mesh points of a rectangular grid of 30×30 points by a spline-interpolation method (see Paihua Montes (1978) and Nguyen Duc & Sommeria (1988)). The vorticity (ω), horizontal divergence ($\partial u/\partial x + \partial v/\partial y$), and local strain rates ($\partial u/\partial x$ and $\partial v/\partial y$) could be calculated in each grid point by differentiation of the splines. Likewise, the stream function was obtained from the interpolated velocity field by numerical integration. The total circulation was obtained by taking the discrete surface integral over the vorticity values.

3.3 Strain flow characteristics

The strain flow pattern is clearly visible from the photograph in figure 3.2, which shows the trajectories of the passive tracers at the mid-plane of the tank. The path lines appear to be smooth without crossing each other, which indicates that the flow is laminar and approximately planar. The flow is characterized by a stagnation point and two symmetry axes, and from the lengths of the particle paths it can be seen that the absolute velocity of the fluid increases at larger radii from the stagnation point.

For a pure strain flow, with the Cartesian coordinates (x, y) taken along the symmetry axes of the flow, the corresponding velocity components would be

$$u(x, y) = ex \tag{3.1}$$

$$v(x, y) = -ey, \tag{3.2}$$

respectively, where the origin coincides with the stagnation point and e is the strain rate.

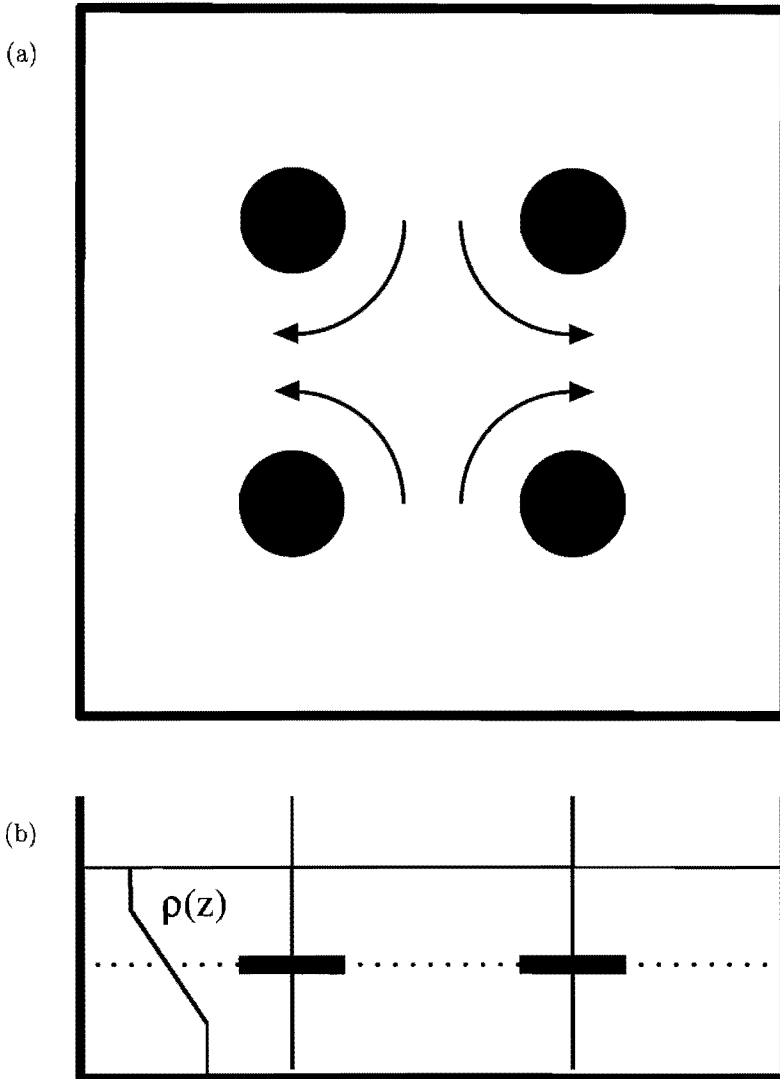


FIGURE 3.1: Schematic drawing of the top view (a) and the side view (b) of the laboratory set-up. The experiments were performed in a 1×1 m perspex tank with a working depth of 0.3 m. A linear density stratification is present near the mid-level of the tank. The strain flow is generated by four rotating horizontal discs, which rotate continuously at a constant angular speed Ω_d . The diagonal distance D between the discs was either 40 or 50 cm. In order to measure the horizontal flow characteristics, passive tracer particles have been added to a horizontal layer of the fluid, which also contains the four rotating discs.

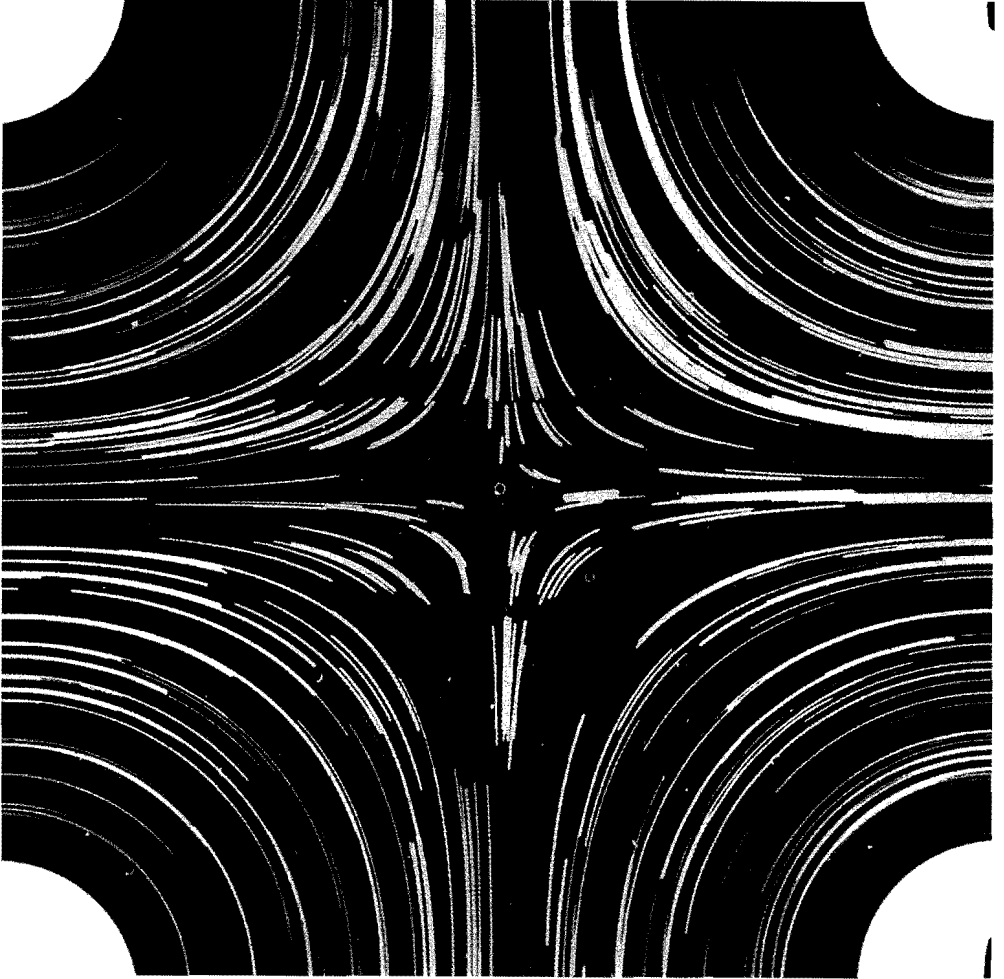


FIGURE 3.2: Photograph showing the trajectories of the tracer particles in the mid-plane of the tank, 4 hours after the start of the forcing. The flow was generated by four rotating horizontal discs, and the strain rate e near the centre of the tank was $0.80 \times 10^{-2} \text{ s}^{-1}$. The photograph was taken with an exposure time of 120 s. Experimental parameters: $\Omega_d = 3.0 \text{ rpm}$, $D = 50 \text{ cm}$ and $N = 2.8 \text{ rad s}^{-1}$.

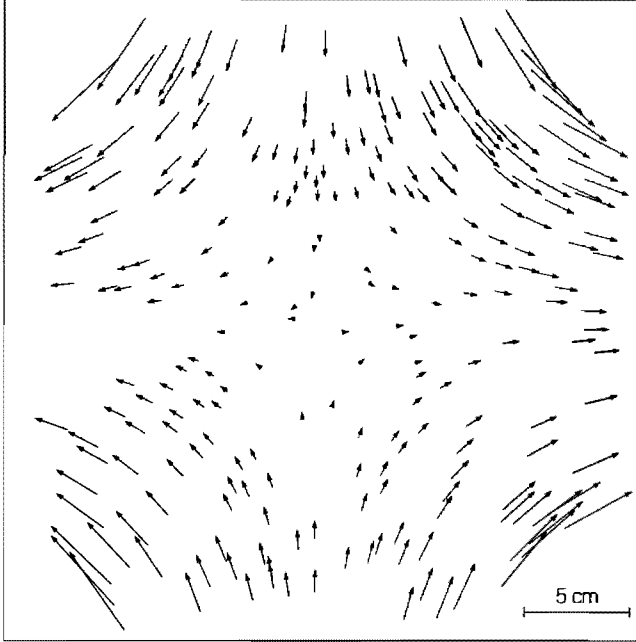


FIGURE 3.3: Measured velocity vectors as obtained from the digitized particle paths, 120 min after the start of the strain flow forcing. The largest vector corresponds to a velocity of 0.142 cm s^{-1} , and the strain rate e near the stagnation point of the flow was equal to $(0.283 \pm 0.003) \times 10^{-2} \text{ s}^{-1}$. Experimental parameters: $\Omega_d = 1.9 \text{ rpm}$, $D = 50 \text{ cm}$ and $N = 2.8 \text{ rad s}^{-1}$.

The measured velocity vectors, as obtained from the digitized particle paths, are plotted in figure 3.3 for one moment of time. To examine whether (3.1) and (3.2) hold for this observed velocity field, for each velocity vector depicted in figure 3.3 the velocity components u and v are plotted versus the spatial coordinates x and y , respectively (see figure 3.4), and substantial scatter is found close to the rotating discs ($D = 50 \text{ cm}$). However, in the centre of the flow field a linear relationship is found, and the scatter can be eliminated by only considering the velocity vectors within a specific circular region around the stagnation point. Figure 3.5 shows the velocity data obtained within a circle of radius 8 cm, and a good linear relationship is observed for each graph.

In order to determine the strain rate within this confined region, each reduced data set was least-squared fitted with the relations $u = e_1(x + x_0)$ and $v = -e_2(y + y_0)$, respectively. The parameters x_0 and y_0 were introduced to account for a possible shift of the stagnation point, but in view of the experimental errors their values were negligibly small. For the data shown in figure 3.5, the slopes e_1 and e_2 are both equal to $0.283 \pm 0.003 \text{ s}^{-1}$. Obviously, a pure strain flow is present within this limited region.

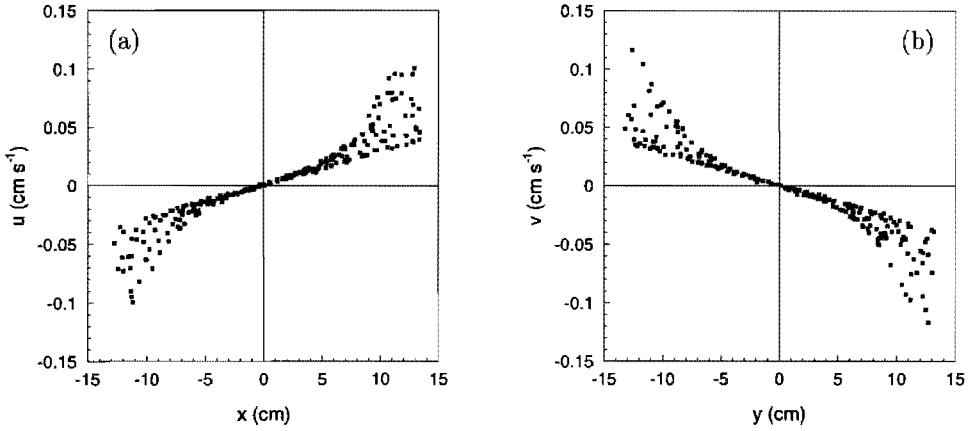


FIGURE 3.4: (a) Velocity component u versus x , and (b) velocity component v versus y , as obtained from each measured velocity vector depicted in figure 3.3. Experimental parameters as in figure 3.3.

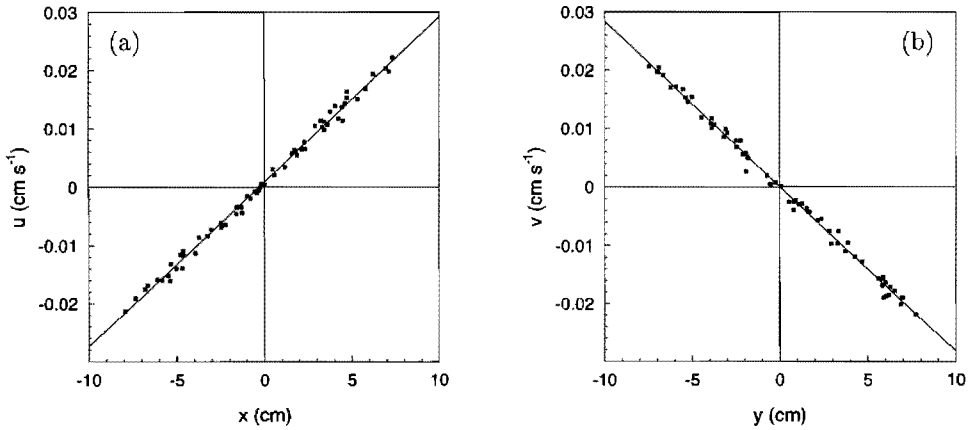


FIGURE 3.5: (a) Velocity component u versus x , and (b) velocity component v versus y . The experimental data (squares) correspond to the velocity vectors in figure 3.3 within the region enclosed by a circle of radius 8 cm. The straight lines correspond to linear least-square fits. Experimental parameters as in figure 3.3.

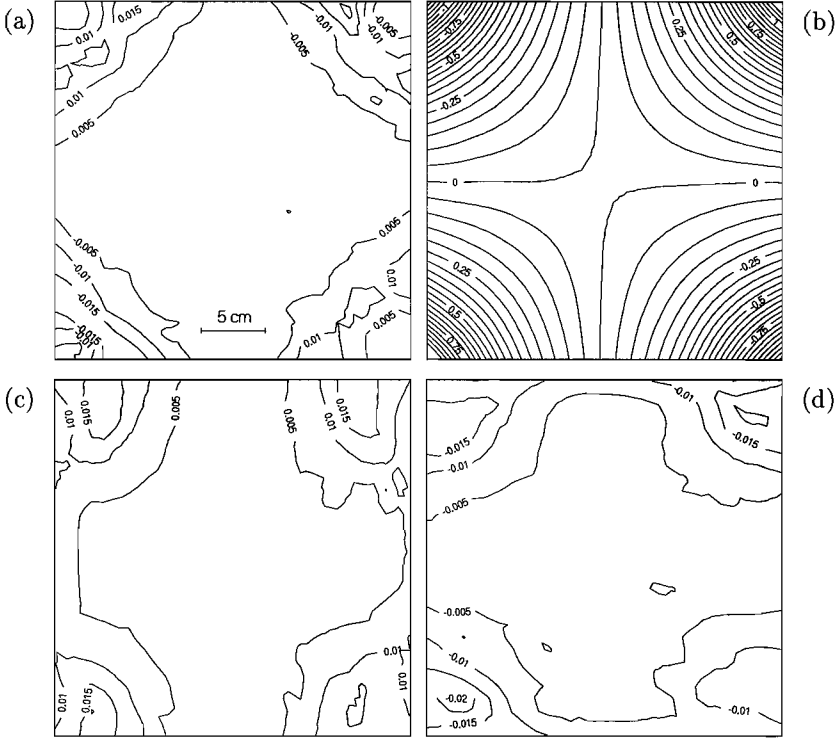


FIGURE 3.6: Contour plots of (a) vorticity ω and (b) stream function ψ , along with the local strain rates (c) $\partial u/\partial x$ and (d) $\partial v/\partial y$. Experimental parameters as in figure 3.3.

This assertion is supported by figure 3.6(a), which provides the vorticity contours of the measured flow field. The vorticity contour plot reveals that the flow is irrotational in the central region, i.e. the magnitude of vorticity is of the same order as the experimental errors. From the non-zero vorticity values near to the rotating discs it can be explained why the corresponding velocity field deviates from a pure strain flow.

In figure 3.6(b) a contour plot of the stream function is shown, and a good agreement is observed with the path lines in figure 3.2. Apparently, the generated strain flow is (quasi) steady, which will be confirmed by the measured time-evolution of the strain rate (see later on).

Calculation of the horizontal divergence $\partial u/\partial x + \partial v/\partial y$ revealed that, except for a small region around the discs, this quantity was approximately zero, which implies that within the region of interest vertical motions can be neglected, i.e. the flow is mainly horizontal. The non-zero divergence values near the discs are caused by three-dimensional effects. That is, at the disc's upper and lower surface a boundary layer is present in which fluid is

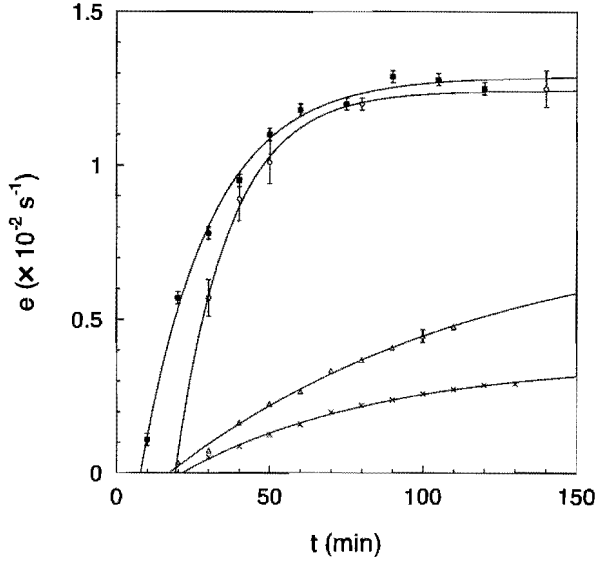


FIGURE 3.7: Temporal evolution of the strain rate e for four different experiments, viz.: exp. 1 (crosses), exp. 2 (triangles), exp. 3 (squares) and exp. 4 (circles). Experimental parameters: see table 3.1.

accelerated. As a result, close to the edge of the disc, fluid is swept radially outward and a turbulent region is formed, which causes vertical motions.

In figure 3.6(c,d) contours of $\partial u/\partial x$ and $\partial v/\partial y$ are shown which represent the local strain rates in the x - and y -directions, respectively. Obviously, the local strain rate values are constant near the centre of the flow, implying a uniform strain flow, but they increase when approaching the rotating discs. This observation is supported by figure 3.4, which shows that the slopes of the relations $u(x)$ and $v(y)$ are constant within the central region of the flow, but become steeper at larger radii.

In order to investigate the stationarity of the generated strain flow, the temporal evolution of the strain rate e is plotted in figure 3.7 for four different experiments. The strain rates were calculated by linear regression of plots as shown in figure 3.5 and by taking the average of the corresponding values e_1 and e_2 , i.e. $e = (e_1 + e_2)/2$. The bounding radius was varied, depending on the diagonal distance D . In all cases it was observed that the strain rate increased in time and eventually reached a constant value. Therefore, each data set was least-square fitted with the relation

$$e(t; e_\infty, \tau, t_0) = e_\infty \left[1 - \exp\left(-\frac{t - t_0}{\tau}\right) \right], \quad (3.3)$$

where the free parameters are written explicitly, and a good agreement was obtained in each case. Apparently, the obtained values e_∞ , τ and t_b depend on the distance D and the rotation speed Ω_d , as can be inferred from table 3.1.

Exp.No.	Ω_d (rpm)	D (cm)	N (rad s ⁻¹)	e_∞ (10 ⁻² s ⁻¹)	τ (min)	t_b (min)
1	1.9	50	2.8	0.36 ± 0.02	64 ± 6	21.4 ± 1.3
2	3.0	50	2.8	0.81 ± 0.11	104 ± 21	17.2 ± 1.4
3	6.4	40	2.1	1.29 ± 0.02	23 ± 2	7.8 ± 0.6
4	6.4	50	2.8	1.24 ± 0.05	18 ± 5	19.0 ± 3.6

TABLE 3.1: Experimental parameters (columns 2–4) and results obtained from least-square fits with (3.3) for four laboratory experiments in which the time-evolution of the strain rate was investigated. The symbols are defined in the text.

The effect of D on the time-evolution of the strain rate can be seen by comparing experiment 3 ($D = 40$ cm, squares) with experiment 4 ($D = 50$ cm, circles). In both cases $\Omega_d = 6.4$ rpm. It is observed that when the discs are positioned further apart, t_b increases, whereas e_∞ remains nearly constant. Also the dependence on the rotation speed of the discs can be examined by comparing experiment 2 ($\Omega_d = 3.0$ rpm, triangles) with experiment 4 ($\Omega_d = 6.4$ rpm, circles). In both cases $D = 50$ cm. It is seen that an increasing rotation speed causes e_∞ to increase, whereas t_b remains virtually constant. The present results are, however, not decisive about the dependence of τ on the experimental parameters.

From the laboratory observations presented above it can be concluded that a pure strain flow can be established near the centre of the tank when the flow is generated by four rotating horizontal discs in a stratified fluid. This was evident quantitatively from the linear relationships between the velocity components and the spatial coordinates, the zero vorticity, the zero horizontal divergence, the stream function, the constant local strain rates, and qualitatively from the particle path photographs.

Furthermore, it was observed that the strain rate establishes at a constant value e_∞ within the characteristic time τ . Therefore, the monopolar vortex was generated at least a period τ after the start of the strain flow forcing to ensure an approximately constant strain flow during the temporal evolution of the vortex.

3.4 Monopolar vortices in a still ambient flow

The evolution of vortices generated by a spinning sphere has been studied in detail in chapter 2. For de sake of completeness, a short outline will be given here.

It was shown in chapter 2 that the measured distributions of vorticity ω and azimuthal velocity v_θ can be closely approximated by the self-similar distributions of the so-called Gaussian vortex (see e.g. figure 2.2), which are given by

$$\omega^* = \left[1 - \frac{1}{2}(r^*)^2\right] \exp\left\{-\frac{1}{2}(r^*)^2\right\} \quad (3.4)$$

and

$$v^* = \frac{1}{2\sqrt{2}} r^* \exp \left\{ -\frac{1}{2} (r^*)^2 \right\}, \quad (3.5)$$

respectively. Here, $\omega^* = \omega/\omega_m$ is the scaled vorticity, with ω_m being the maximum vorticity, and v^* is the corresponding normalized azimuthal velocity. The radial position of the peak velocity r_m , which is a measure of the vortex radius, has been used to normalize the radial coordinate r according to $r^* = r/r_m$. The Gaussian vortex is typified by a core of single-signed vorticity and a ring of oppositely-signed vorticity. Moreover, the Gaussian vortex is ‘isolated’, i.e. the vortex has no net vorticity. This was checked in chapter 2 by taking the discrete surface integral over the measured vorticity values at the grid points, and the total circulation of the vortex indeed appeared to be zero within the experimental errors.

The corresponding nondimensional stream function can be derived from (3.5), and is given by

$$\psi^* = \frac{1}{2} \exp \left\{ -\frac{1}{2} (r^*)^2 \right\}, \quad (3.6)$$

Furthermore, the functional relationship F between ω^* and ψ^* can be obtained from (3.4) and (3.6), yielding

$$\omega^* = F(\psi^*) = 2\psi^* [1 + \ln 2\psi^*]. \quad (3.7)$$

This theoretical relationship was in good agreement with the laboratory observations (see figure 2.4).

It was also shown in chapter 2 that the radial expansion of the vortex can mainly be ascribed to horizontal diffusion of vorticity, which can be expressed analytically as

$$r_m^2 = r_0^2 + 2\nu t, \quad (3.8)$$

where r_0 represents the radius of the peak velocity at $t = 0$. Furthermore, it was shown that the maximum vorticity near the mid-plane ($z = 0$) decays by both horizontal and vertical diffusion according to

$$\omega_m = \frac{C}{\nu^2(t+t_0)^2} \frac{1}{\sqrt{\nu t}}, \quad (3.9)$$

in which the ‘initial time’ t_0 is related to the initial radius of the vortex by $r_0 = \sqrt{2\nu t_0}$.

3.5 Observed behaviour of a monopolar vortex in a strain flow

The typical observed evolution of a monopolar vortex in a strain flow is illustrated by the vorticity contour plots in figure 3.8. The essential experimental parameters are listed in table 3.2 for five different experiments. In this case, exp. 6, the strain rate was equal to $0.30 \times 10^{-2} \text{ s}^{-1}$. Figure 3.8(a) shows the vorticity contours 60 s after the generation of the vortex. It can be clearly seen that the vortex is still approximately axisymmetric and has a core of positive vorticity surrounded by a ring of negative vorticity. In the

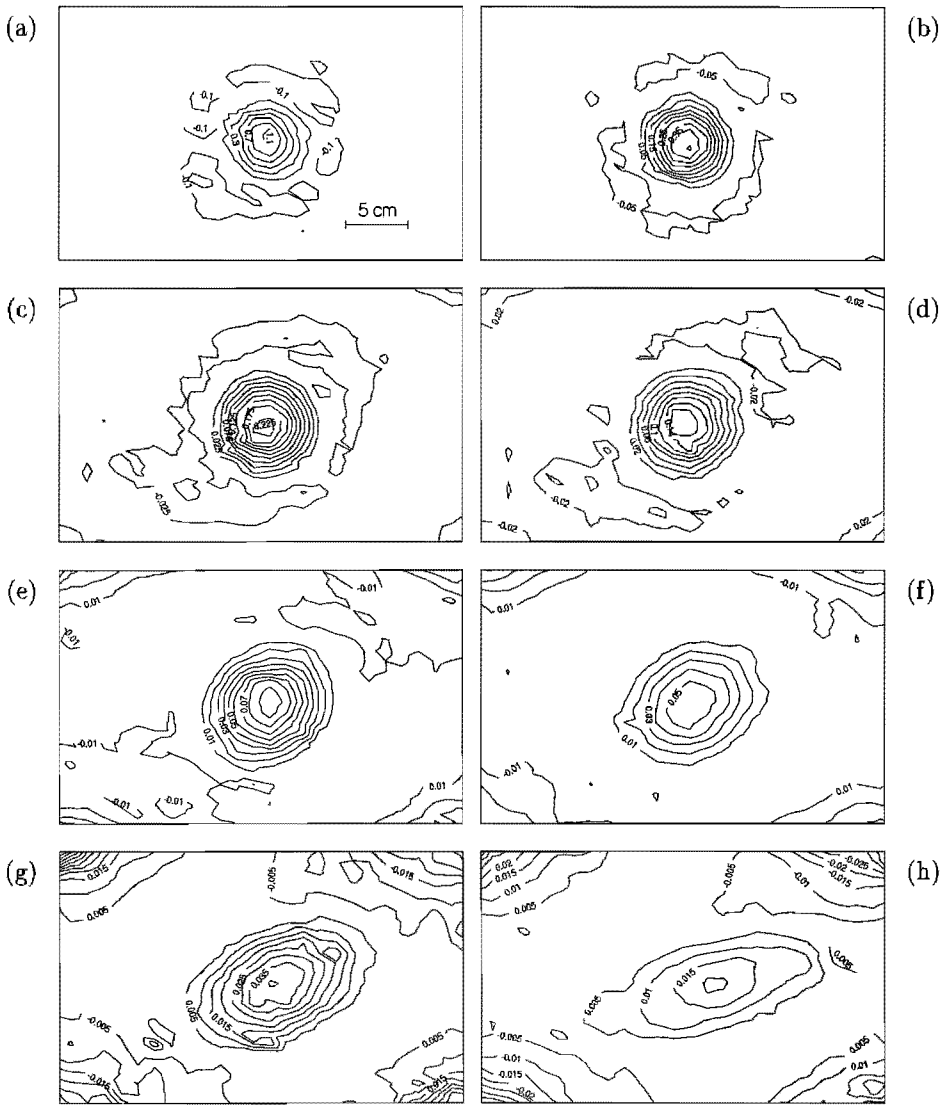


FIGURE 3.8: Contour plots of vorticity ω for a monopolar vortex in a strain flow of (initial) strength $e = (0.303 \pm 0.005) \times 10^{-2} \text{ s}^{-1}$: (a) $t = 60 \text{ s}$, (b) 120 s , (c) 180 s , (d) 240 s , (e) 360 s , (f) 480 s , (g) 600 s and (h) 840 s . Experimental parameters are given in table 3.2 (exp. 6).

Exp.No.	Ω_d (rpm)	D (cm)	N (rad s ⁻¹)	t_f (min)	$e(t_f)$ (10 ⁻² s ⁻¹)	Ω_s (rpm)	δt (s)
5	0	-	2.9	-	0	150	15
6	1.9	50	2.8	150	0.303 ± 0.005	150	15
7	3.0	40	2.8	110	0.474 ± 0.005	162	15
8	6.4	50	1.6	90	1.29 ± 0.03	252	10
9	12.4	40	3.4	100	2.5 ± 0.1	279	5

TABLE 3.2: Experimental parameters for five laboratory experiments in which a monopolar vortex was submitted to a strain flow. Before the onset of the vortex generation, the ambient flow was allowed to develop during a time period t_f . The other symbols are defined in the text.

next stage, see (b) and (c), this ring breaks up into two patches, positioned at an angle of approximately 45 degrees with respect to the horizontal strain axis, which are soon thereafter removed from the vortex core by the ambient flow, see (d). Eventually, the core of positive vorticity remains, surrounded by weak oppositely-signed vorticity, as evident from (e) and (f). Comparison of frames (d)–(g) reveals that the vortex elongates while at high vorticity values its orientation remains almost constant at an angle of 45 degrees with respect to the horizontal strain axis. In the final stage, beyond $t \approx 600$ s (see (h)), the elliptic-like vortex rotates towards the horizontal strain axis and is continuously elongated by the ambient flow.

Note that during the total time-evolution, the horizontal size of the vortex increases, whereas the maximum of vorticity decreases. Later on, it will be shown that the expansion of the vortex can mainly be attributed to horizontal diffusion of vorticity, and that the decay of vorticity is caused by both horizontal and vertical diffusion.

The strain rate dependence of the vortex evolution was examined by performing similar experiments as shown in figure 3.8, but with higher strain rates. The effect of the larger strain rate $e = 0.47 \times 10^{-2} \text{ s}^{-1}$ (exp. 7) is evident from the vorticity plots presented in figure 3.9(a–h). The rotation speed and the forcing period of the sphere were taken the same as in the previous experiment. At $t = 75$ s (a), the core of the vortex is circular, but the accompanying negative vorticity is already concentrated into two satellites, which are located on opposite sides of the vortex core. When both patches of negative vorticity are orientated at an angle of approximately 45 degrees with respect to the horizontal strain axis, as observed in (b), they are quickly advected by the strain flow, see (c), and an elliptic vortex remains with mainly positive vorticity, as shown in (d). After $t \approx 375$ s, both the fast elongation and the overturning motion of the vortex are clearly visible from (e)–(g). Finally, the vortex is completely torn apart along the horizontal strain axis, and the basic strain flow remains, as can be seen in (h). Comparison with figure 3.8 reveals that the indefinite elongation of the vortex sets in sooner when a larger strain rate is applied.

Figure 3.10 shows the evolution of a monopolar vortex in a strain flow of strength

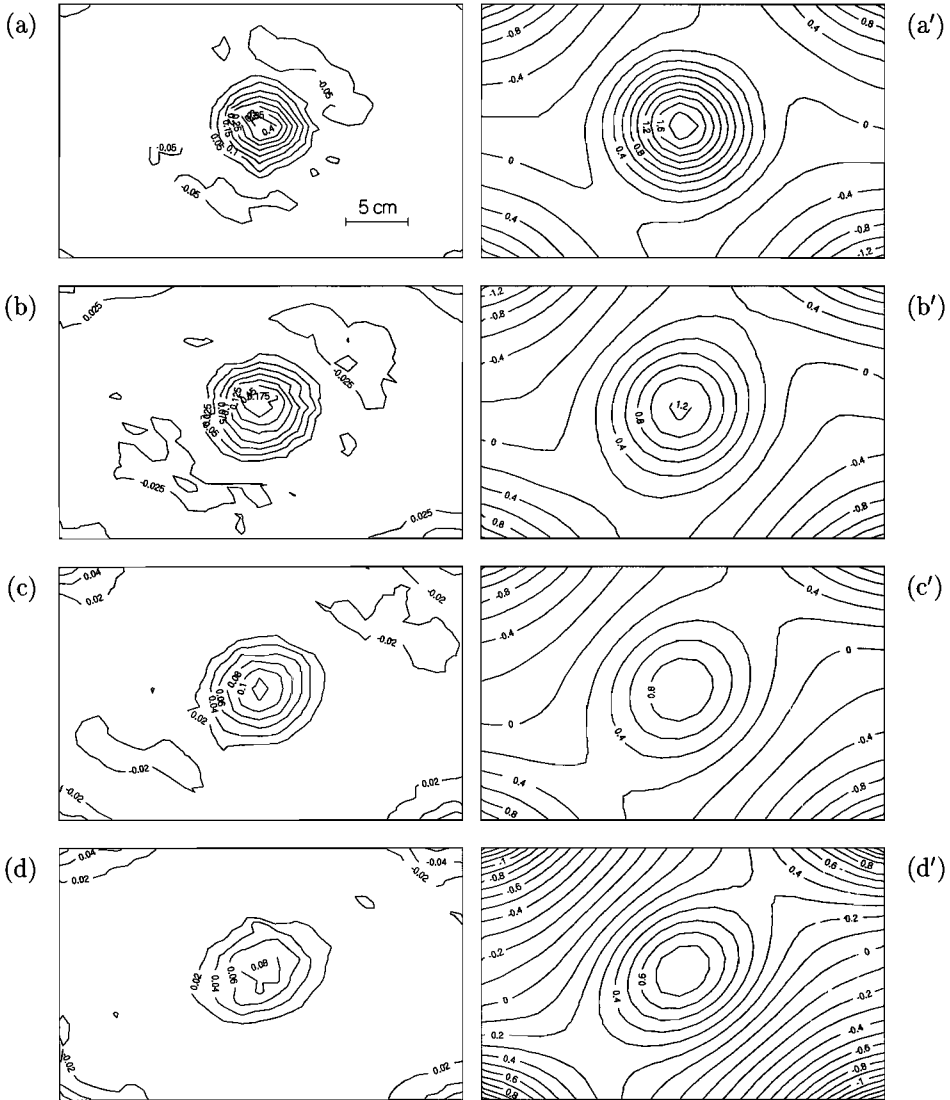


FIGURE 3.9: Contour plots of vorticity ω (left column) and corresponding stream function ψ (right column) for a monopolar vortex in a strain flow with initial strength $e = (0.474 \pm 0.005) \times 10^{-2} \text{ s}^{-1}$: (a,a') $t = 75 \text{ s}$, (b,b') 135 s , (c,c') 195 s , (d,d') 255 s , (e,e') 375 s , (f,f') 495 s , (g,g') 615 s and (h,h') 855 s . Experimental parameters are given in table 3.2 (exp. 7).

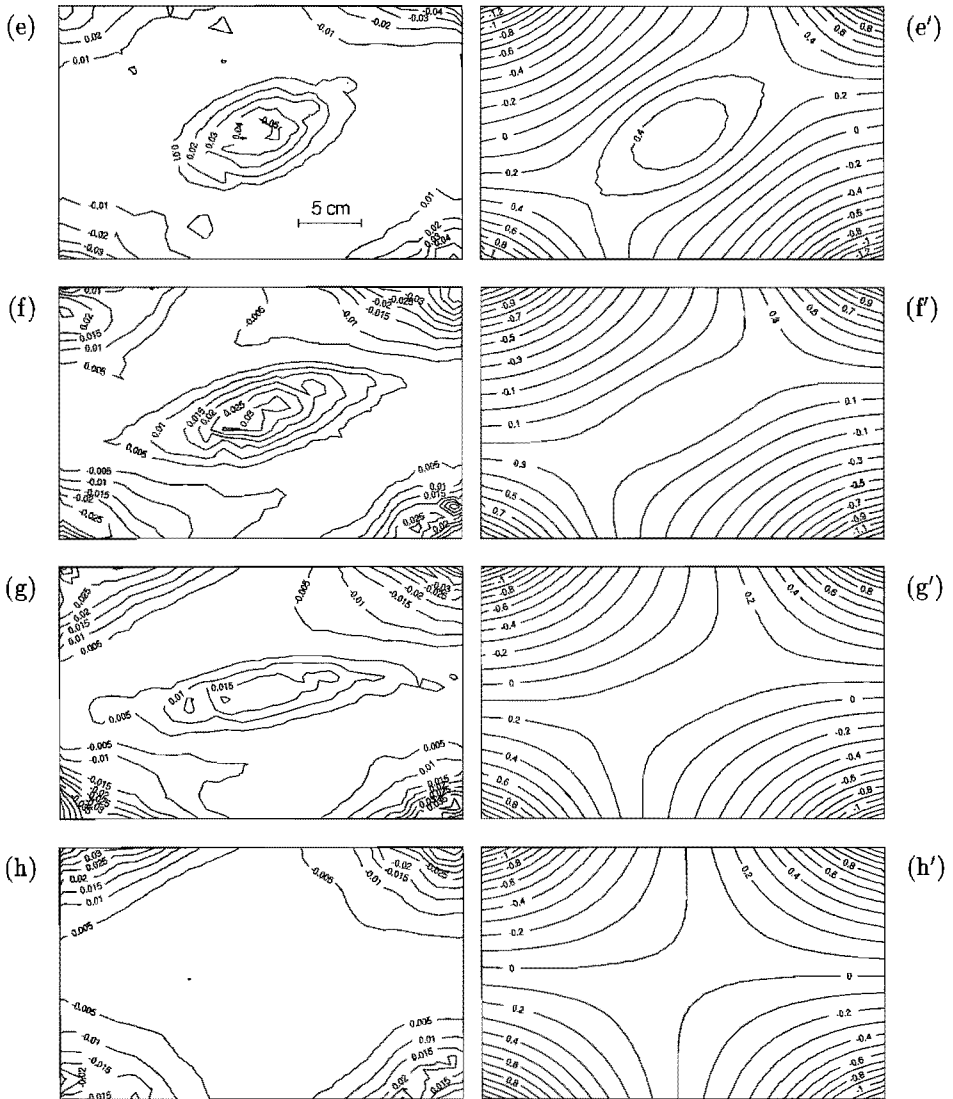


FIGURE 3.9: Continued.

$e = 2.5 \times 10^{-2} \text{ s}^{-1}$ (exp. 9), which is considerably stronger than the strain rates considered in figures 3.8 and 3.9. In order to minimize the effect of the ambient flow on the vortex generation, the sphere was spun during a shorter time period and with a higher rotation speed. Almost immediately after the generation of the vortex, the ring of negative vorticity is carried away by the ambient flow, as can be observed in figure 3.10(a) and (b). Likewise, the irreversible elongation of the vortex has already started at $t \approx 160 \text{ s}$, see (c)–(f), which is much sooner than for weaker strain rates. Nevertheless, a similar evolution is observed as in figures 3.8 and 3.9. Therefore, it can be concluded that the strain rate merely determines the speed of the vortex evolution, but not the evolution itself.

The shedding of the negative vorticity ring can be explained by considering the stream function plots, which are depicted in figure 3.9(a')–(h'). Two types of streamlines can be defined for these graphs: 'closed' streamlines, which enclose the centre of the vortex, and 'open' streamlines, which are apparently unbounded (actually each encloses one of the rotating discs). Both types are separated by the so-called 'separatrix', which is the boundary of the nested set of closed streamlines. In most plots two stagnation points can be identified, which both lie on the separatrix, provided that the flow is symmetric with respect to both strain axes. If the flow is stationary, fluid particles within the separatrix are trapped and rotate around the vortex centre, whereas outside they follow unbounded trajectories. However, owing to the decay of vorticity, the area enclosed by the separatrix becomes smaller, i.e. fluid particles that were initially trapped are forced to leave the enclosed region. Furthermore, horizontal diffusion may account for a continuous leakage of vorticity through the separatrix.

At $t = 75 \text{ s}$ (see figure 3.9(a')) the vortex is almost entirely enclosed by the separatrix. However, as time increases, negative vorticity leaks through the separatrix owing to the processes described above. Subsequently, negative vorticity accumulates near the stagnation points, see (b,b'), giving rise to two patches of negative vorticity which are carried away along the open streamlines, as shown in (c,c'). Next, see (d,d') and (e,e'), positive vorticity crosses the separatrix. Note that until this stage, the vorticity contours in the vortex core closely match the corresponding streamlines. Soon thereafter, however, the entire vortex structure rotates towards the horizontal strain axis. During this final stage of the evolution, the area enclosed by the separatrix quickly decreases (see (f')), the stagnation points vanish (see (g')) and the basic strain flow pattern returns, as can be observed in (h'). Similar streamline patterns were obtained for other experiments (see e.g. figure 3.10(a')–(f')).

The advection of negative vorticity can be illustrated differently by plotting the velocity component v and the vorticity ω along the x -axis, as shown in figure 3.11 (exp. 6). The measured data points (indicated by squares) were obtained from the values at the grid points by bilinear interpolation. The velocity and vorticity have been scaled with their extremal values v_m and ω_m , respectively, whereas the x -coordinate has been scaled with the position of the peak velocity. The observed data are compared with the self-similar profiles (3.4) and (3.5) associated with the Gaussian vortex model (solid lines). In figure 3.11(b), the measured cross-sectional vorticity distribution is shown at $t = 120 \text{ s}$. Obviously, the vortex core is surrounded by a well-defined ring of negative vorticity, and the measured

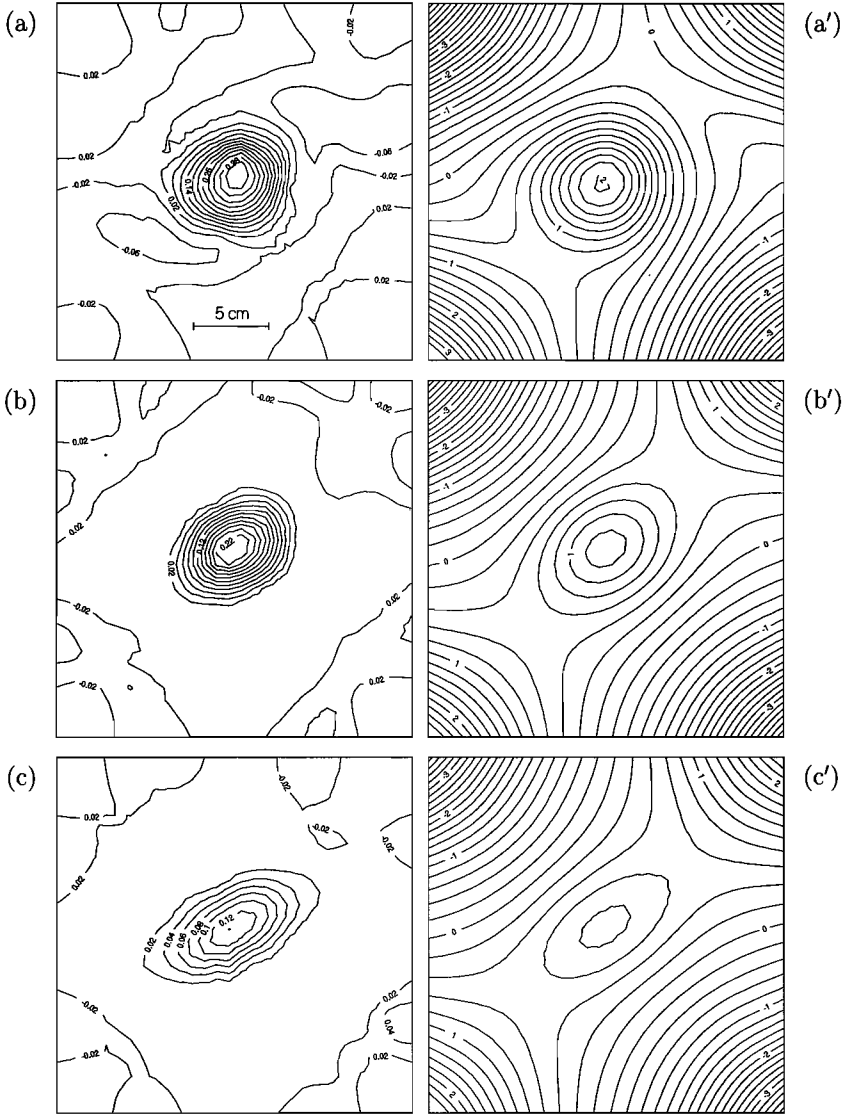


FIGURE 3.10: Contour plots of vorticity ω (left column) and corresponding stream function ψ (right column) for a monopolar vortex in a strain flow with $e \approx 0.025 \text{ s}^{-1}$: (a,a') $t = 40$ s, (b,b') 120 s, (c,c') 180 s, (d,d') 220 s, (e,e') 260 s and (f,f') 320 s. Experimental parameters are given in table 3.2 (exp. 9).

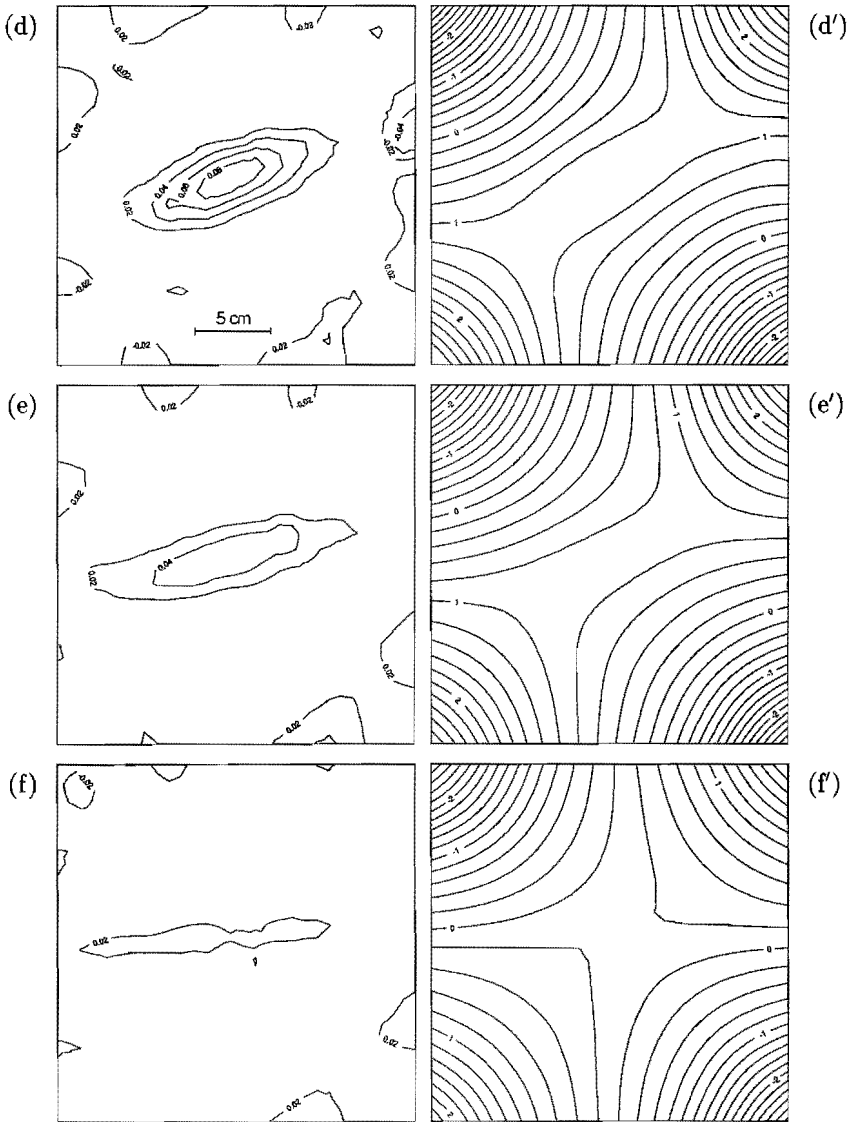


FIGURE 3.10: Continued.

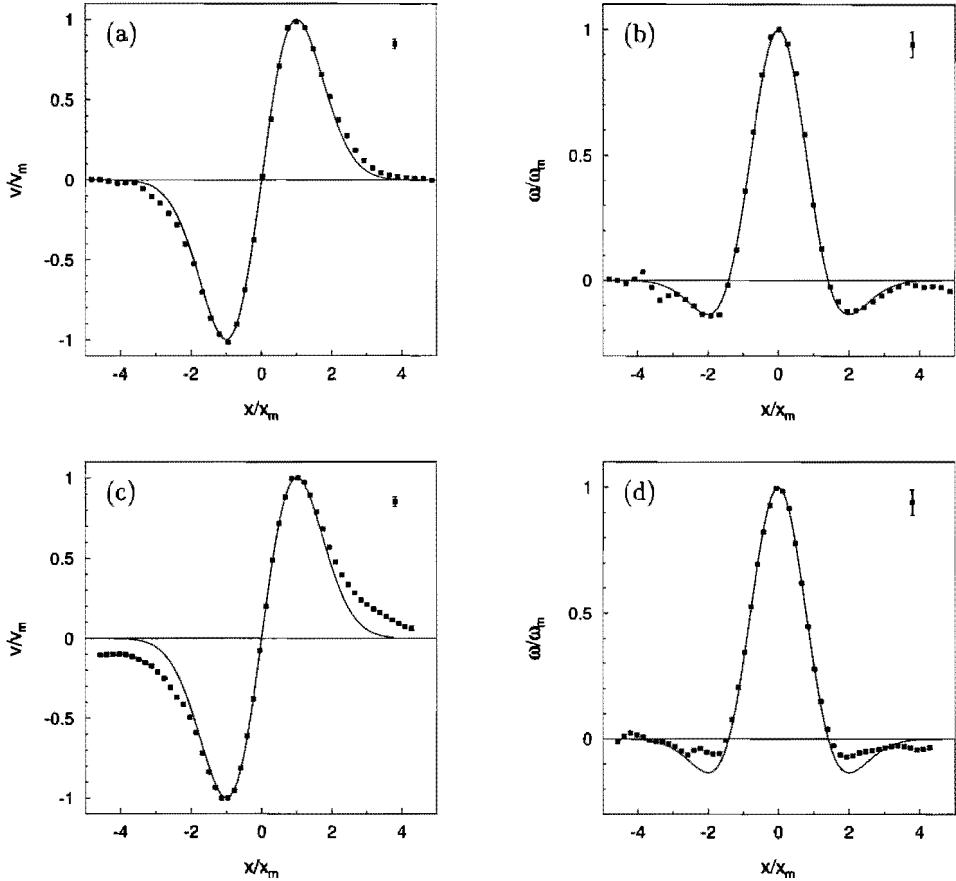


FIGURE 3.11: Cross-sectional distributions of the velocity component v (left column) and the vorticity ω (right column) along the x -axis at (a,b) $t = 120$ s and (c,d) 360 s, for a monopolar vortex in a strain flow. The velocity and vorticity have been scaled with their extremal values ω_m and v_m , respectively, whereas the x -coordinate has been scaled with the position of the peak velocity x_m . The observed data (denoted by squares) are compared with the profiles according to the Gaussian vortex model (solid lines). At $t = 120$ s: $\omega_m = 0.41$ s $^{-1}$, $v_m = 0.40$ cm s $^{-1}$ and $r_m = 2.9$ cm; whereas at $t = 360$ s: $\omega_m = 0.09$ s $^{-1}$, $v_m = 0.11$ cm s $^{-1}$ and $r_m = 4.0$ cm. Experimental parameters: see table 3.2 (exp. 6).

data are in good agreement with the Gaussian vortex model. However, at $t = 360$ s (see (d)), the (scaled) amplitude of the negative vorticity has decreased by a factor two, whereas the core of the vortex still closely matches the profile corresponding to the Gaussian vortex model. In this case, part of the negative vorticity has been removed from the vortex along the open streamlines.

The removal of negative vorticity is also evident from the accompanying velocity profiles depicted in figure 3.11(a) and (c). Initially, the measured velocity data are in good agreement with the Gaussian vortex model, as shown in figure 3.11(a), but later on, see figure 3.11(c), the tail of the observed velocity profile becomes less steep and tends towards a $1/r$ -velocity distribution, indicating that vorticity has been carried away by the ambient flow.

In summary, the results in figures 3.9–3.11 show that outside the separatrix, vorticity is being removed from the vortex, whereas inside the separatrix the vorticity distribution is apparently unaffected by the strain flow. Hence, the separatrix serves as a sharp boundary between the inner and outer flow.

Close observation of figures 3.9 and 3.10 reveals that the vorticity contours in the core of the vortex coincide very well with the corresponding streamlines for a considerable time until the vortex is overcome by the strain flow. Stationary vortices are characterized by a functional relationship between vorticity ω and stream function ψ , and therefore it is argued that the initial evolution of the observed vortex in the straining field is quasi-stationary. To obtain a more quantitative idea of this process, the vorticity has been plotted versus the stream function in a scatter plot for four successive times (see figure 3.12). For clarity, the background vorticity close to the rotating discs has been excluded by only plotting the measured data points corresponding to the centre of the flow field. Figure 3.12(a) shows the scatter plot at $t = 120$ s, and a good agreement is obtained with the (ω, ψ) -relationship of a Gaussian vortex (solid line), which has been fitted with the experimental data for $\omega > 0.25\omega_m$. So far, the main vortex characteristics appear to be not affected by the strain flow. However, at $t = 360$ s (see (b)), the scatter in the vortex ring is more pronounced, because negative vorticity is being shed from the vortex by the strain flow. At this time, the positive branch is still virtually unaffected. After that, low-amplitude vorticity of positive sign is carried away by the ambient flow, which is obvious in (c) ($t = 600$ s) from the scatter in the positive vorticity branch. Note that the scatter is less pronounced for larger values of positive vorticity, which implies that the main part of the vortex core is still close to equilibrium. Finally, the vortex rotates towards the horizontal strain axis while simultaneously being torn apart, as evident on (d) ($t = 840$ s) from the large scatter in the entire vortex. Based on these scatter plots it can be concluded that the main part of the vortex core evolves quasi-stationary until the vortex is overcome by the strain flow.

At high vorticity amplitudes, the vorticity contours have a shape that is close to elliptic, as can be seen in figures 3.8–3.10. In figure 3.13, typical measured vorticity contours are shown, which are represented by the squares. A least-squares algorithm was used to fit each observed contour with an ellipse (solid line), and a good agreement is obtained in each case. This procedure was applied to several vorticity contours and their corresponding streamlines at various moments of time. In this way, aspect ratios $\lambda_\omega(\omega, t)$ and $\lambda_\psi(\psi, t)$,

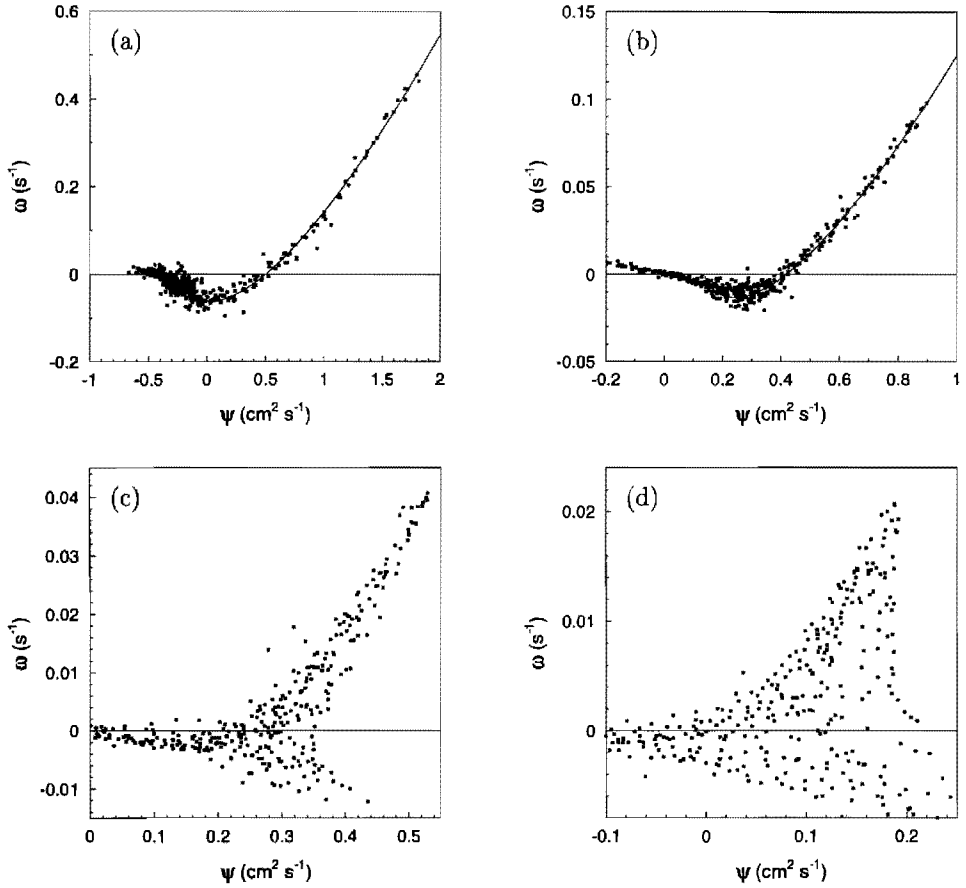


FIGURE 3.12: Sequence of measured (ω, ψ) -scatter plots (squares) showing the typical evolution of the (ω, ψ) -relation for a monopolar vortex in a strain flow: (a) $t = 120$ s, (b) 360 s, (c) 600 s and (d) 840 s. In (a) and (b), the (ω, ψ) -relationship (3.7) of the Gaussian vortex (solid line) has been least-square fitted to the observed data for $\omega > 0.25\omega_m$. Experimental parameters: see table 3.2 (exp. 6).

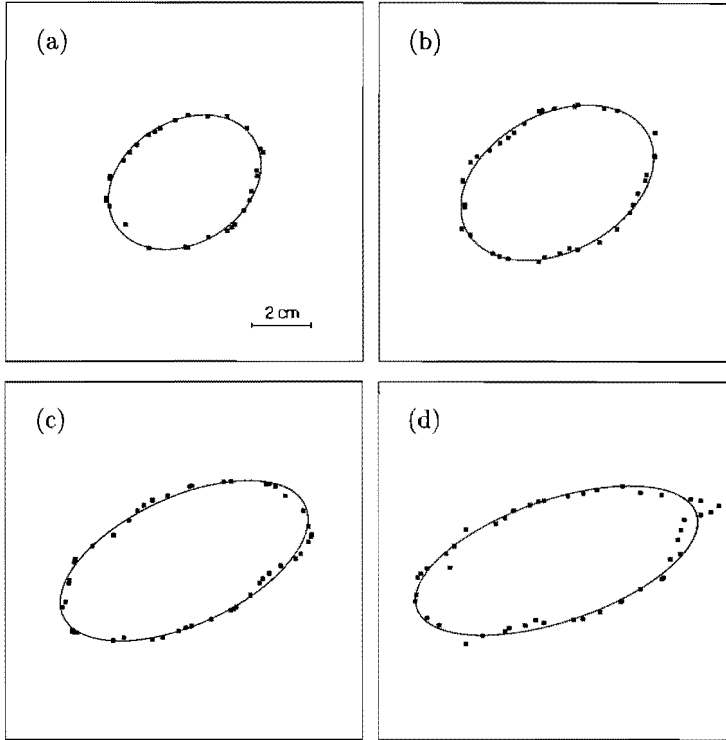


FIGURE 3.13: Typical discretized vorticity contours $\omega = 0.697\omega_m$ of a vortex in a strain flow at four different times, viz. at (a) $t = 420$ s, (b) 600 s, (c) 720 s and (d) 840 s. A perfect elliptic contour (solid line) has been fitted to each measured contour. Experimental parameters: see table 3.2 (exp. 6).

and orientations $\phi_\omega(\omega, t)$ and $\phi_\psi(\psi, t)$ were obtained. The temporal evolution of these quantities will be given in the next section.

A similar method, introduced by Overman & Zabusky (1984), has been applied to numerical simulations by Melander, McWilliams & Zabusky (1987). The latter authors determined the aspect ratio and orientation of an elliptic-like contour by calculating the second-order moments of the domain contained by that specific contour. Because of the relatively low resolution of the present laboratory observations, however, this approach was not adopted here, and the simple least-squares algorithm appeared to be the most suitable method.

As far as the region inside the separatrix is concerned, both $\lambda_\omega(\omega, t)$ and $\phi_\omega(\omega, t)$ varied less than 10% as a function of ω , which was also true for the aspect ratio and orientation of the stream function contours. In other words, $\lambda_\omega(\omega, t) \approx \lambda_\omega(t)$ and $\phi_\omega(\omega, t) \approx \phi_\omega(t)$,

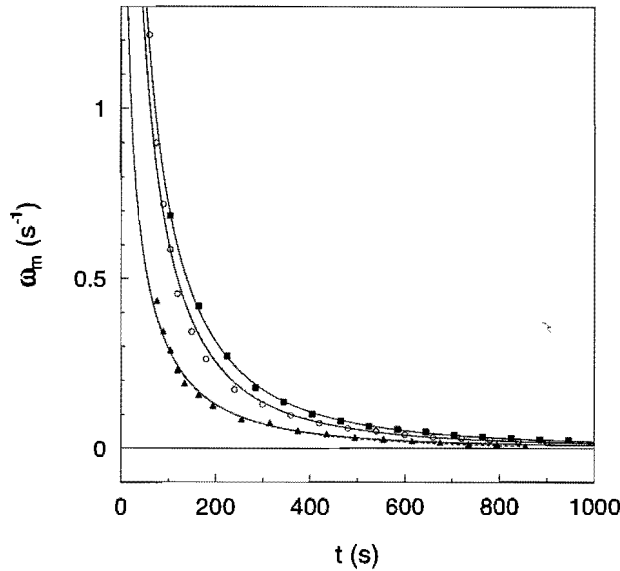


FIGURE 3.14: Temporal evolution of the peak vorticity ω_m for a monopolar vortex in a strain flow: $e = 0 \text{ s}^{-1}$ (exp. 5, squares), $e = 0.30 \times 10^{-2} \text{ s}^{-1}$ (exp. 6, circles) and $e = 0.47 \times 10^{-2} \text{ s}^{-1}$ (exp. 7, triangles). The solid lines have been least-square fitted with (3.9) to the observed data (see text for more details). The dashed lines (which closely follow the solid lines) correspond to the numerically obtained decay of maximum vorticity (see section 3.6).

and likewise for the aspect ratio and orientation of the closed streamlines. Obviously, the vortex core is robust and behaves like a patch of uniform vorticity.

During the initial quasi-stationary evolution of the vortex, also $\lambda_\omega(t) \approx \lambda_\psi(t)$ and $\phi_\omega(t) \approx \phi_\psi(t)$, i.e. the contours are in phase (see figures 3.9(d) and 3.9(d') as an example). However, when the vortex starts to tumble towards the horizontal strain axis, the equivorticity lines and streamlines inside the separatrix become phase-shifted, i.e. $\phi_\omega(t) < \phi_\psi(t)$. For instance, compare the orientation of the vorticity contours and streamlines plotted in figures 3.9(f) and 3.9(f'), respectively. The reason for this phase-shift is that the streamline pattern is rather insensitive to the exact shape of the vortex.

In figure 3.14, the temporal decay of maximum vorticity ω_m is plotted for the experiments shown in figure 3.8 (circles, exp. 6) and figure 3.10 (triangles, exp. 7). Also, the decay of the peak vorticity is presented for a vortex without background flow (squares, exp. 5). In these three experiments, both the rotation speed and the forcing period of the sphere were taken the same. Each data set was least-square fitted by (3.9), where the constant C and the initial time t_0 were taken as free parameters. In a numerical study by Mariotti, Legras & Dritschel (1994) on monopolar vortices in shear flows, it was observed that during the final stage of indefinite elongation the decay of maximum vorticity acceler-

ates by the combined effect of shear and horizontal diffusion. Since their numerical results may also be applied to the case of a monopolar vortex in a strain flow, in figure 3.14 only the initial stage of the maximum vorticity evolution was least-squares fitted, i.e. $t < 700$ s for exp. 6 and $t < 400$ s for exp. 7. Although relation (3.9) has been derived for a Gaussian vortex in a still ambient fluid, for each experiment a good agreement is obtained until the moment of indefinite elongation. Apparently, the initial decay of maximum vorticity is not affected by the strain flow. In the next section, this assertion will be confirmed by numerical simulations.

Nevertheless, it is clear from figure 3.14 that at each moment of time the peak vorticity is smaller for larger strain rates, although in each experiment the vortex was generated with the same rotation speed and forcing period. Therefore, it is most likely that the formation of the vortex is affected by the strain flow. During the spinning of the sphere, fluid is swept away horizontally near the sphere's equator, so that part of the momentum might be removed by the background flow before a well-defined vortex is formed, with less momentum, i.e. weaker maximum vorticity, than for a vortex in a still ambient fluid.

3.6 Modelling of monopolar vortices in a strain flow

Only few exact solutions of the 2D Euler equations are known concerning the motion of elliptic vortices. It was shown analytically by Kirchhoff (1876) that an elliptic patch of uniform vorticity in an otherwise quiescent fluid rotates steadily around its centre, without any shape changes. Likewise, steady elliptic vortices in a uniform shear flow were considered by Moore & Saffman (1971), whereas the corresponding unsteady solutions were obtained by Kida (1981). Since a uniform shear flow can be decomposed into a solid-body rotation and a pure strain flow, Kida's analysis can be applied to the case of a vortex in a pure strain flow.

The laboratory observations presented in section 3.5 have demonstrated that in the initial stage of the evolution, the vortex core behaves like an elliptic patch of uniform vorticity. Therefore, as a first approach, the laboratory vortex will be modelled by an elliptic patch of uniform vorticity, and Kida's original model will be extended to account for the observed decay of vorticity. It will be shown that during the initial stage, the vortex evolves close to equilibrium states, which was also observed in the laboratory.

As a second approach, the full 2D vorticity equation will be solved numerically by a finite-difference method to account for the non-uniform vorticity distribution of the laboratory vortex and the horizontal diffusion of vorticity. The results will be compared with the laboratory observations.

3.6.1 Motion of a uniform elliptic vortex in a pure strain flow

An elliptic region of uniform vorticity ω is considered with aspect ratio λ and with its major axis tilted by an angle ϕ with respect to the x -axis. The vortex is embedded in a

pure strain flow, for which the velocity components in the Cartesian directions (x, y) are given by (3.1) and (3.2).

According to Kida (1981), the equations of motion for the elliptic vortex are given by

$$\dot{\lambda} = 2e\lambda \cos 2\phi \quad (3.10)$$

$$\dot{\phi} = -e \frac{\lambda^2 + 1}{\lambda^2 - 1} \sin 2\phi + \frac{\omega\lambda}{(\lambda + 1)^2}, \quad (3.11)$$

where e represents the strain rate, and differentiation with respect to time is denoted by a dot.

From (3.10) and (3.11) several types of motion can be derived depending on the ratio $\Lambda = |e/\omega|$ as well as the initial aspect ratio λ_0 and orientation ϕ_0 of the elliptic vortex. When the rate of strain is larger than a critical value, i.e. $\Lambda > \Lambda_c = 0.15$, the vortex will be elongated irreversibly in the strain direction, whereas in weaker strain flows ($\Lambda < \Lambda_c$) the vortex may rotate around its centre or wobble around a fixed angle, generally with shape oscillations. For each value of $\Lambda < \Lambda_c$, two stationary states exist, of which one is unstable. These steady solutions have also been obtained before by Moore & Saffman (1971).

Following Kida, the occurrence of these different types of motion may be explained qualitatively by combining (3.10) and (3.11), which yields

$$\frac{e}{\omega} \sin 2\phi = g(\lambda; s), \quad (3.12)$$

where the so-called g -function is defined by

$$g(\lambda; s) \equiv \frac{\lambda}{\lambda^2 - 1} \ln \frac{(\lambda + 1)^2}{4s\lambda}, \quad (3.13)$$

with s a constant of integration. Differentiation of (3.13) with respect to λ , and using (3.11), leads to

$$\dot{\phi} = \omega\lambda \left. \frac{\partial g}{\partial \lambda} \right|_s, \quad (3.14)$$

implying that the rotation of the vortex is related to the derivative of g with respect to λ .

Now, the motion of the elliptic vortex can be deduced by considering the family of g -functions plotted in figure 3.15, where each curve corresponds to a particular value of s . Since $g(\lambda; s) = -g(1/\lambda; s)$ and the equations of motion are invariant by the transformation $(\omega, \phi) \rightarrow (-\omega, -\phi)$, it suffices to consider the range $0 \leq \lambda \leq 1$ and $\omega \geq 0$. If $0 < s \leq s_c$, with $s_c (= 0.893)$ a critical value, g is a monotonically decreasing function of λ , while it has two extremal values if $s_c < s < 1$. Only one extremal value is present for $s \geq 1$. When $s = s_c$, the two extremal values coincide at $\lambda = \lambda_c = 0.346$, for which $g = -\Lambda_c = -0.15$. In figure 3.15, the (local) extremal values are connected by the dashed line.

The state of the elliptic vortex is given by (λ, ϕ) , which can be represented in the λg -plane (figure 3.15) by the vector \vec{k} , defined by

$$\vec{k} \equiv (\lambda, g), \quad (3.15)$$

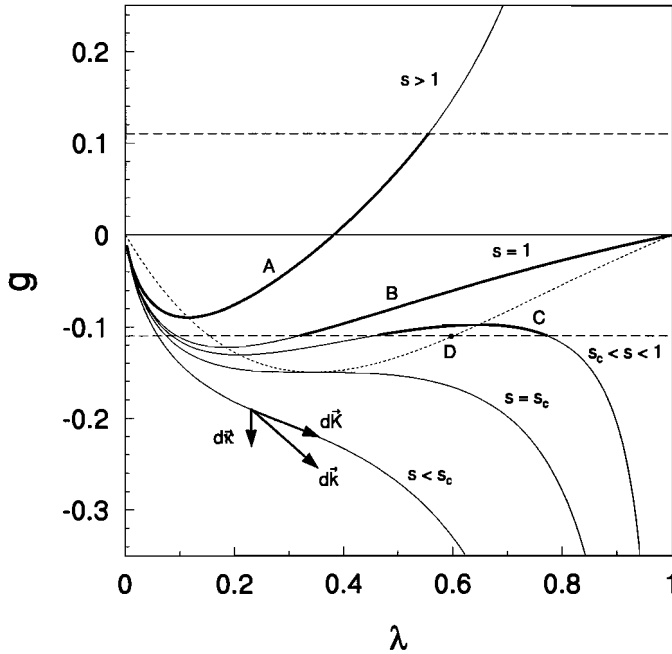


FIGURE 3.15: Graph showing the g -function versus λ for different values of s (indicated by the solid line) in case of a pure strain flow. The local extrema of g are connected by the dashed line. The heavy solid lines, which are bounded by the extremal values $g = \pm\Lambda = \pm 0.11$ (dotted lines), represent different kinds of motion of the elliptic vortex, viz.: irreversible elongation (A), rotation (B), nutation (C) and equilibrium (D). Also the vector decomposition of $d\vec{k}$ is indicated for a time-dependent Λ (see text).

where g merely represents the orientation ϕ of the vortex, as can be seen from relation (3.12). For example, a circular-shaped vortex corresponds with $\vec{k} = (1, 0)$, whereas an infinitely elongated vortex is represented by $\vec{k} = (0, 0)$. Strictly speaking, \vec{k} represents two degenerate states in the λg -plane that have the same aspect ratio but different orientations, i.e.: (λ, ϕ) and $(\lambda, \pi - \phi)$. However, the actual state is always obvious from the sign of $\dot{\lambda}$ in (3.10).

Likewise, the motion of the vortex, represented by $(\dot{\lambda}, \dot{\phi})$, is given in the λg -plane by

$$\frac{d\vec{k}}{dt} = (\dot{\lambda}, \dot{g}). \quad (3.16)$$

Note that \dot{g} is related to $\dot{\phi}$ through relation (3.14), since $\dot{g} = (\partial g / \partial \lambda)|_s \dot{\lambda}$.

Given a value for the constant s , which is determined by the initial state \vec{k}_0 , i.e. (λ_0, ϕ_0) , the vector \vec{k} moves along the corresponding g -curve, where the direction of motion (along the λ -axis) is determined by (3.10). From (3.12) it follows that the motion in the λg -plane is restricted to the region $|g| \leq \Lambda$. When $|g| = \Lambda$, the motion of the vortex is reversed by (3.10), i.e. $\dot{\lambda} = 0$. It is this restriction that brings about the different types of motion. This is illustrated by the marked g -curves in figure 3.15, where $\Lambda = 0.11$ is taken as an example. Curve A corresponds with a vortex that will eventually be elongated along the horizontal strain axis, while curve B represents a rotating vortex (note that this curve continues into the region $\lambda > 1$). Furthermore, curve C indicates a vortex that oscillates around a fixed angle, and point D represents a stationary vortex, i.e. $\dot{\lambda} = 0$ and $\dot{\phi} = 0$.

Decay of vorticity

When the vorticity of the elliptic patch is allowed to decay in time, the equations given above are still applicable, but now the parameters ω and s are functions of time, i.e. $\omega = \omega(t)$ and $s = s(t)$. For each time, the state and the motion of the vortex in the λg -plane are represented again by the vectors \vec{k} and $d\vec{k}/dt$, respectively. However, the motion is no longer restricted to g -curves of constant s , which can be seen as follows. By defining

$$h(\phi; \omega) \equiv \frac{e}{\omega} \sin 2\phi, \quad (3.17)$$

expression (3.12) can be written as

$$g(\lambda; s) = h(\phi; \omega). \quad (3.18)$$

Differentiation of g with respect to time yields

$$\begin{aligned} \dot{g} &= \dot{h} \\ &= \left. \frac{\partial h}{\partial \phi} \right|_{\omega} \dot{\phi} + \left. \frac{\partial h}{\partial \omega} \right|_{\phi} \dot{\omega}, \end{aligned} \quad (3.19)$$

so that the motion of the vortex is described by

$$\begin{aligned} \frac{d\vec{k}}{dt} &= \left(\dot{\lambda}, \left. \frac{\partial h}{\partial \phi} \right|_{\omega} \dot{\phi} \right) + \left(0, \left. \frac{\partial h}{\partial \omega} \right|_{\phi} \dot{\omega} \right) \\ &\equiv \frac{d\vec{K}}{dt} + \frac{d\vec{\kappa}}{dt}, \end{aligned} \quad (3.20)$$

where $d\vec{K}/dt$ corresponds to the motion of an elliptic patch with constant vorticity, and $d\vec{\kappa}/dt$ represents the motion owing to the decay of vorticity.

The contribution from the decreasing vorticity can be rewritten as:

$$\begin{aligned} \frac{d\vec{\kappa}}{dt} &= \left(0, -\frac{e\dot{\omega}}{\omega^2} \sin 2\phi \right) \\ &\equiv (0, \beta). \end{aligned} \quad (3.21)$$

Since $\dot{\omega} < 0$ by assumption, it follows that

$$\beta > 0 \quad \text{if } g > 0 \quad (3.22)$$

$$\beta < 0 \quad \text{if } g < 0. \quad (3.23)$$

Thus, the effect of the decaying vorticity is to shift the vector \vec{k} to an adjoining upper or lower g -curve, depending on the sign of the original g -value. This is indicated schematically in figure 3.15.

Non-uniform vorticity distribution

In section 3.5 it was shown that the core of the laboratory vortex is characterized by the non-uniform vorticity distribution according to the Gaussian vortex model. Moreover, it was observed that the vortex core behaves like an elliptic patch of uniform vorticity. In order to compare the laboratory observations with the extended Kida model, a mean vorticity value $\bar{\omega}$ will be defined for the laboratory vortex, according to

$$\bar{\omega}^* = \frac{1}{\pi} \int_0^{2\pi} \int_0^1 \omega^*(r^*) r^* dr^* d\phi \quad (3.24)$$

where the vorticity ω has been scaled with the extremal value of $\omega(r)$, and the radius r has been normalized by the corresponding radial position of the peak velocity r_m . Here, only the region $r \leq r_m$ is considered to calculate the mean vorticity. When $\omega^*(r^*)$ is taken as the scaled vorticity distribution associated with the Gaussian vortex model, see (3.4), it follows that $\bar{\omega}^* = 0.697$ (see figure 3.16).

Using (3.24) and $\bar{\omega}^* = 0.697$, the critical ratio between the rate of strain and the maximum vorticity can be calculated for a Gaussian vortex, according to

$$\left| \frac{e}{\omega_m} \right|_c = 0.697 \left| \frac{e}{\bar{\omega}} \right|_c = 0.697 \Lambda_c. \quad (3.25)$$

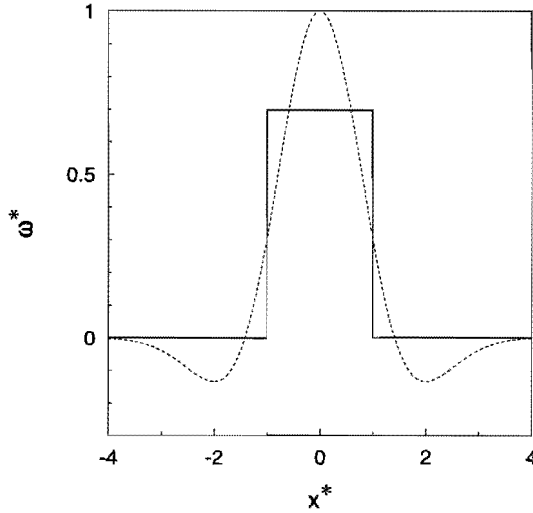


FIGURE 3.16: Vorticity profile of the Gaussian vortex (dashed line) compared with the uniform vorticity distribution of the Kida vortex (solid line). The vorticity ω and spatial coordinate x have been normalized by the extremal vorticity ω_m of the Gaussian vortex and the corresponding radius of the peak velocity r_m , respectively.

Since $\Lambda_c = 0.15$ it follows that $|e/\omega_m|_c = 0.105$. This is in very good agreement with unpublished results by Dritschel, who found the same value based on contour dynamics simulations. Similar calculations (see e.g. Legras & Dritschel (1993)) have shown that this critical value $|e/\omega_m|_c$ is independent of the vorticity distribution inside the vortex as long as the shape of the profile near the vortex centre is parabolic, which is generally the case for smooth vorticity distributions. For an exact parabolic profile ($\omega = 1 - r^2$, with $0 \leq r \leq 1$), the mean vorticity as defined in (3.24) is equal to $2/3 \approx 0.667$, which is close to the corresponding value for a Gaussian vortex.

Numerical algorithm

A fourth-order Runge-Kutta method was applied to solve the equations of motion (3.10) and (3.11), and the numerical integration was performed with a time step $\Delta t = 0.05$ s. The state $(\lambda_0, \phi_0) = (1, 0)$ was taken as the initial condition, and the strain rate e was held constant at $0.303 \times 10^{-2} \text{ s}^{-1}$ (which is equal to the strain rate in experiment 6). Since the initial decay of (maximum) vorticity is not affected significantly by the strain flow (see section 3.5), this decay was modelled by (3.9) for a Gaussian vortex without background flow. Because of the infinite vorticity at $t = 0$ (see (3.9)), the time integration was started at $t = \Delta t$, which is believed to have no significant effect on the numerical results.

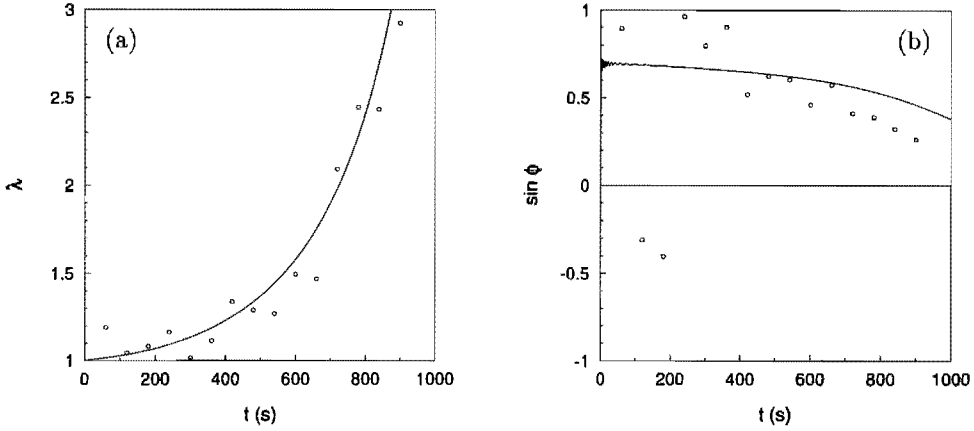


FIGURE 3.17: The aspect ratio λ and orientation ϕ versus time as obtained from the numerical integration (solid line) and the laboratory observations (circles). The integration was started at $t = \Delta t$ (Δt being the time step) with an initially circular patch of vorticity ($\vec{k} = (1, 0)$) in a strain flow of strength $e = 0.303 \times 10^{-2} \text{ s}^{-1}$. The uniform vorticity was allowed to decay according to (3.9), with $C = 5.36 \text{ cm}^5 \text{ s}^{-1}$, $\nu = 1.065 \times 10^{-2} \text{ cm}^2 \text{ s}^{-1}$ and $t_0 = 227 \text{ s}$. Experimental parameters: see table 3.2 (exp. 6).

Numerical results

Figure 3.17 shows the numerical results (solid lines) for the time-evolution of λ and ϕ . Initially, the aspect ratio gradually increases, whereas the orientation of the vortex ϕ oscillates with high frequency. However, the amplitude and frequency of the fluctuations in ϕ are quickly damped, and in the next stage, $t > 300 \text{ s}$, the angle ϕ gradually decreases with no more oscillations. Close to the critical value Λ_c at $t \approx 700 \text{ s}$, the indefinite vortex tearing sets in, which is clear from the exponential increase of λ and the accelerated decrease of ϕ .

In order to make a comparison with the laboratory observations, the measured vorticity contours satisfying $\omega = \bar{\omega} = 0.697\omega_m$ were least-square fitted with ellipses, as described in section 3.5, for various moments of time. The measured aspect ratio λ ($= \lambda_\omega(\bar{\omega}, t)$) and orientation ϕ ($= \phi_\omega(\bar{\omega}, t)$) are plotted in figure 3.17 versus time, and the numerical solution for the aspect ratio appears to be in good agreement with the experimental results. The measured time-evolution of ϕ deviates systematically from the calculated evolution, but qualitatively the same behaviour is observed. For $t < 400 \text{ s}$, large-amplitude oscillations are present for the observed orientation of the ellipse, which are less pronounced in the numerical simulation. These fluctuations are probably induced by the satellites of negative vorticity, which initially rotate around the vortex core before being detached by the ambient flow; an effect that is not dealt with by the extended Kida model. Part of the oscillation may also be caused by internal waves, which inevitably emerge during the forcing stage and the subsequent lifting of the sphere.

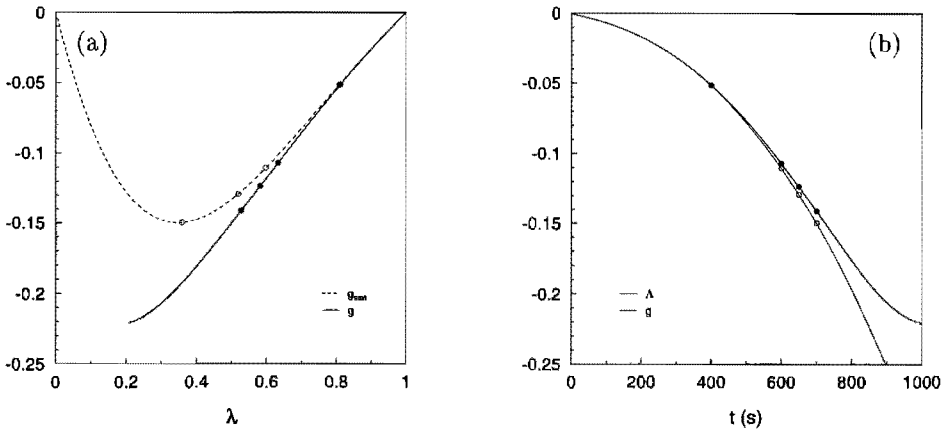


FIGURE 3.18: (a) Solution curve (solid line) in the λg -plane, corresponding to the evolution depicted in figure 3.17, and the stationary states (dashed line) as obtained analytically from the Kida model. At four different times, the state \vec{k} of the elliptic vortex (marked by filled circles) is compared with the corresponding steady state (open circles). (b) Comparison between the calculated evolution of $g(t)$ (solid line) and $\Lambda(t)$ (dotted line).

In section 3.5 it was argued that the indefinite vortex elongation is preceded by a quasi-stationary stage. Since Kida's model allows to calculate the stationary states analytically, it is interesting to see how close the numerical solutions are to equilibrium before the indefinite elongation sets in. The vortex evolves along quasi-stationary states as long as the state \vec{k} is close to the curve connecting the (local) extremal values of g , i.e. $\dot{\phi} \approx 0$, and its component g is close to one of the bounding values $\pm\Lambda$, so that $\dot{\lambda} \approx 0$.

Accordingly, in figure 3.18(a) the numerically obtained values of g (solid line) are plotted versus λ , as well as the curve corresponding with the (local) extremal values of g (dashed line). For convenience, the transformations $\lambda \rightarrow 1/\lambda$ and $g \rightarrow -g$ have been applied. It is seen that initially both curves coincide very well. When $\lambda \approx 0.8$ ($t \approx 400$ s) the numerical solution g starts to separate from the dashed line, but both curves are still close to each other up to $\lambda \approx 0.6$ ($t \approx 600$ s). After that, an accelerated deviation is observed around $\lambda = 0.5$ ($t = 700$ s). Thus, the calculated g -values are close to the dashed curve until the final stage of indefinite elongation. However, this assertion does not guarantee quasi-stationary solutions; it is a necessary but not sufficient condition for quasi-equilibrium states. The another requirement is that g is close to Λ . Therefore, the calculated time-evolutions of g (solid line) and Λ (dotted line) are plotted in figure 3.18(b), and a good agreement is obtained between both curves until the vortex is torn apart at $t \approx 700$ s.

In order to make a direct comparison, in figure 3.18 the calculated states \vec{k} and the corresponding equilibrium states have been marked by filled and open circles, respectively, at four different times. Again it is clear that the vortex evolves close to equilibrium states until the final breaking of the vortex by the strain flow.

3.6.2 Modelling of a distributed vortex in a pure strain flow

Experimental observations by Flór & van Heijst (1996) have revealed that monopolar vortices in a stratified fluid are characterized by a flat pancake-like shape. From a simple scaling analysis, it was shown that to leading order in Ri^{-1} vertical motions are decoupled from the horizontal motions, and vorticity vectors are approximately directed vertically in a thin region around the mid-plane ($z = 0$). Here, Ri represents the bulk Richardson number $Ri = N^2\sigma^2/U^2$, with 2σ the typical monopole thickness and U a characteristic horizontal velocity scale. Consequently, the three-dimensional vorticity equation around $z = 0$ is reduced to:

$$\frac{\partial\omega}{\partial t} + J(\omega, \psi) = \nu\nabla_h^2\omega + \nu\frac{\partial^2\omega}{\partial z^2}, \quad (3.26)$$

with ω the vertical component of vorticity, ν the kinematic viscosity, ∇_h the gradient operator acting in horizontal direction, and the Jacobian J defined by

$$J(\omega, \psi) = \frac{\partial\omega}{\partial x}\frac{\partial\psi}{\partial y} - \frac{\partial\omega}{\partial y}\frac{\partial\psi}{\partial x}. \quad (3.27)$$

Because of this quasi-two-dimensional behaviour of the flow around the mid-plane $z = 0$, the vertical diffusion term in (3.26) will be modelled by an analytical expression, so as to solve (3.26) in only two dimensions. As in earlier studies (see Flór, van Heijst & Delfos (1995), Flór & van Heijst (1996) and chapter 2), the vorticity is written as

$$\omega = \omega_{2D}(x, y, t)\Phi(z, t), \quad (3.28)$$

where $\omega_{2D}(x, y, t)$ represents the horizontal vorticity distribution satisfying the purely two-dimensional vorticity equation

$$\frac{\partial\omega_{2D}}{\partial t} + J(\omega_{2D}, \psi) = \nu\nabla_h^2\omega_{2D}, \quad (3.29)$$

and $\Phi(z, t)$ is an amplitude function associated with the vertical diffusion of vorticity. Substitution of (3.28) in (3.26) reveals that the viscous decay of Φ is governed by:

$$\frac{\partial\Phi}{\partial t} = \nu\frac{\partial^2\Phi}{\partial z^2}. \quad (3.30)$$

The vortex is assumed to be confined in a very thin region, represented by $\Phi(z, 0) = \Phi_0\delta(z)$, with δ the Dirac delta function. The corresponding solution of the vertical diffusion equation (3.30) is then given by

$$\Phi = \frac{\Phi_0}{\sqrt{\nu t}} \exp\left(-\frac{z^2}{4\nu t}\right). \quad (3.31)$$

Although this delta-like initial condition cannot be satisfied in the actual flow, it is assumed that the thickness of the vortex at $t = 0$ is relatively small, and that at later times (3.31) still gives a reasonable description of the finite vertical vorticity distribution.

In the mid-plane, $z = 0$, the vertical diffusion term in (3.26) can now be expressed analytically, using (3.28) and (3.31), as

$$\nu \left. \frac{\partial^2 \omega}{\partial z^2} \right|_{z=0} = \nu \omega_{2D} \left. \frac{\partial^2 \Phi}{\partial z^2} \right|_{z=0} = -\frac{\omega(z=0)}{2t}. \quad (3.32)$$

As a result, the flow around $z = 0$ satisfies the quasi-2D vorticity equation

$$\frac{\partial \omega}{\partial t} + J(\omega, \psi) = \nu \nabla_h^2 \omega - \frac{\omega}{2t}, \quad (3.33)$$

for $t > 0$, along with the 2D continuity equation

$$\omega = -\nabla_h^2 \psi. \quad (3.34)$$

Both (3.33) and (3.34) have been solved by a finite-difference method that is second-order accurate both in space and in time. The numerical scheme is based on that of Orlandi (1990), and has been slightly adapted to account for the vertical damping term and the ambient velocity field.

The time-integration was performed by a third-order Runge-Kutta method; the Jacobian being calculated explicitly, while the horizontal and vertical diffusion terms were discretized by the implicit Crank-Nicolson scheme. The nonlinear term J in (3.33) was evaluated by the so-called Arakawa scheme (see Arakawa (1966)), which in the inviscid limit conserves the higher-order invariants of motion, such as energy and enstrophy. The implicit treatment of the horizontal diffusion term leads to a pentadiagonal matrix, the inversion of which is highly time consuming. Therefore, this matrix was decomposed into two tridiagonal matrices, which can be easily inverted by common solvers. Although this approach reduces the accuracy of the time-integration to second-order, the scheme has a larger stability regime than other commonly used second-order schemes, i.e. $CFL \leq \sqrt{3}$.

The solution of (3.34) was obtained by a FACR (Fourier Analysis and Cyclic Reduction) Poisson solver (see Hockney (1970)) with appropriate boundary conditions to account for the pure strain flow (note that the ambient flow contains zero vorticity):

$$\psi|_b = exy|_b, \quad (3.35)$$

where b indicates the boundary of the computational domain.

The Cartesian coordinate system has been chosen such that the origin coincides with the stagnation point of the ambient flow, and that the x - and y -axis are oriented along the principle axes of the strain flow. The calculations were performed on a 256×256 grid, which proved to be accurate enough to resolve the vorticity field.

As an initial condition, the vorticity distribution (3.4) corresponding to the Gaussian vortex was chosen. Since the quasi-2D vorticity equation (3.33) is singular at $t = 0$, and the vorticity values are very large for small t (implying a very small time step to satisfy the CFL condition), the time integration was started at $t = 5$ s. The corresponding values for ω_m and r_m , which determine the instantaneous state of the Gaussian vortex, were

obtained from the least-squares fits through the observed data as shown in figure 3.14. Strictly speaking, the vorticity distribution at $t = 5$ s is not represented by that of a Gaussian vortex. However, considering the small initial ratio e/ω_m , the contribution from the strain flow may be neglected at small times.

The typical flow evolution as obtained numerically is shown by the sequence of vorticity contour plots depicted in figure 3.19. Here, the initial conditions of experiment 6 have been used, and a similar behaviour is found as observed in the laboratory (see figure 3.8). Initially, see figure 3.19(a), the vortex is virtually unaffected by the ambient flow, given the nearly axisymmetric shape of the vortex. When time increases, see (b), the vortex becomes slightly distorted but is still close to circular. In the next stage (c–g), however, the emergence of two patches of negative vorticity and the removal of negative vorticity by the strain flow are obvious. Finally, see (h), the vortex is rotated towards the horizontal strain axis and is eventually torn apart. Comparison with figure 3.8 reveals that the advection of negative vorticity occurs faster in the laboratory than in the numerical simulation. Also the final rotation speed of the vortex is experimentally larger than numerically. The differences may be explained by the non-uniformity of the experimental strain flow, which will be discussed later on.

Laboratory observations presented in section 3.5 have demonstrated that the vortex core evolves quasi-steadily until the final stage of indefinite elongation. A sequence of numerically obtained (ω, ψ) -scatter plots is shown in figure 3.20, and a good agreement is observed with the experimental results presented in figure 3.12. The scatter in figure 3.12 is more pronounced because of the experimental errors and the faster evolution of the laboratory vortex. From figure 3.20, it is also evident that the positive branch of the calculated scatter plots is in good agreement with the (ω, ψ) -relationship according to the Gaussian model.

In figure 3.14, the numerically obtained decay of the maximum vorticity (dashed lines) is compared with the experimental data, and a good agreement is observed for each experiment. In addition, the numerical results closely match the least-squares fits (solid lines) related to the extended-decay model until the vortex is overcome by the strain flow. This is most clear from the data corresponding to experiment 7 (triangles). Around $t = 400$ s ($|e/\omega_m| \approx |e/\omega_m|_c$), the calculated curve departs from the least-squares fit, but still closely follows the experimental data. These results support the assertion that the initial decay of the maximum vorticity is not affected by the strain flow and is accurately described by (3.9).

In order to make a quantitative comparison between the experiments and the numerical simulations, the numerically obtained vorticity contours $\omega = \bar{\omega} = 0.697\omega_m$ were discretized and least-square fitted with ellipses, using the same method as described in section 3.5. Figure 3.21 shows typical discretized vorticity contours corresponding to the intermediate and the final stage of the vortex evolution, and the contours clearly resemble perfect ellipses. These ellipses were used to determine the major and minor axes (a and b), the aspect ratio (λ) and the inclination (ϕ) for a sequence of times.

The calculated evolutions of the major and the minor axis (a and b) are indicated in figure 3.22(a) by the solid and dashed lines, respectively. Initially, both a and b increase

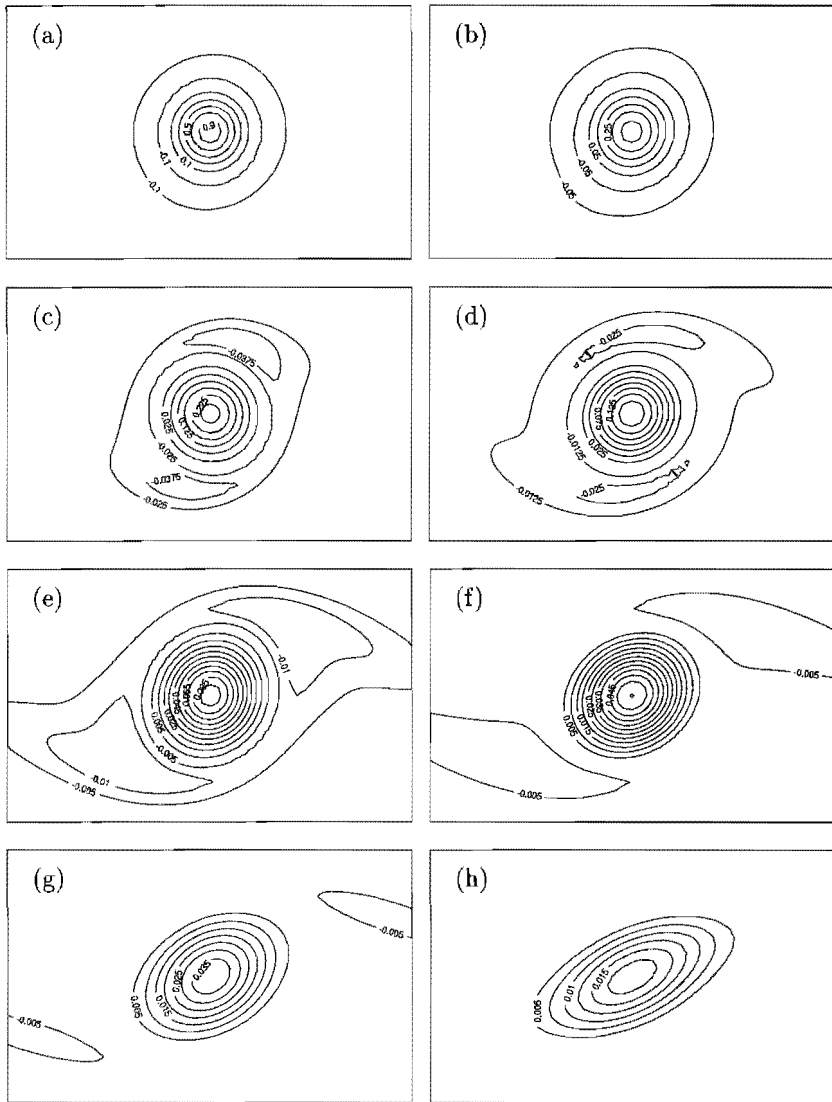


FIGURE 3.19: Sequence of vorticity contour plots as obtained from the numerical simulation of an isolated monopolar vortex in a pure strain flow (with $e = 0.30 \times 10^{-2} \text{ s}^{-1}$). As an initial condition (at $t = 5$), a Gaussian vortex was taken with $\omega_m = 5.48 \text{ s}^{-1}$ and $r_m^2 = 4.93 \text{ cm}^2$. (a) $t = 60 \text{ s}$, (b) 120 s , (c) 180 s , (d) 240 s , (e) 360 s , (f) 480 s , (g) 600 s and (h) 840 s ($\nu = 1.065 \times 10^{-2} \text{ cm}^2 \text{ s}^{-1}$, CFL = 0.5). The numerical results may be compared with the measured contours of vorticity depicted in figure 3.8.

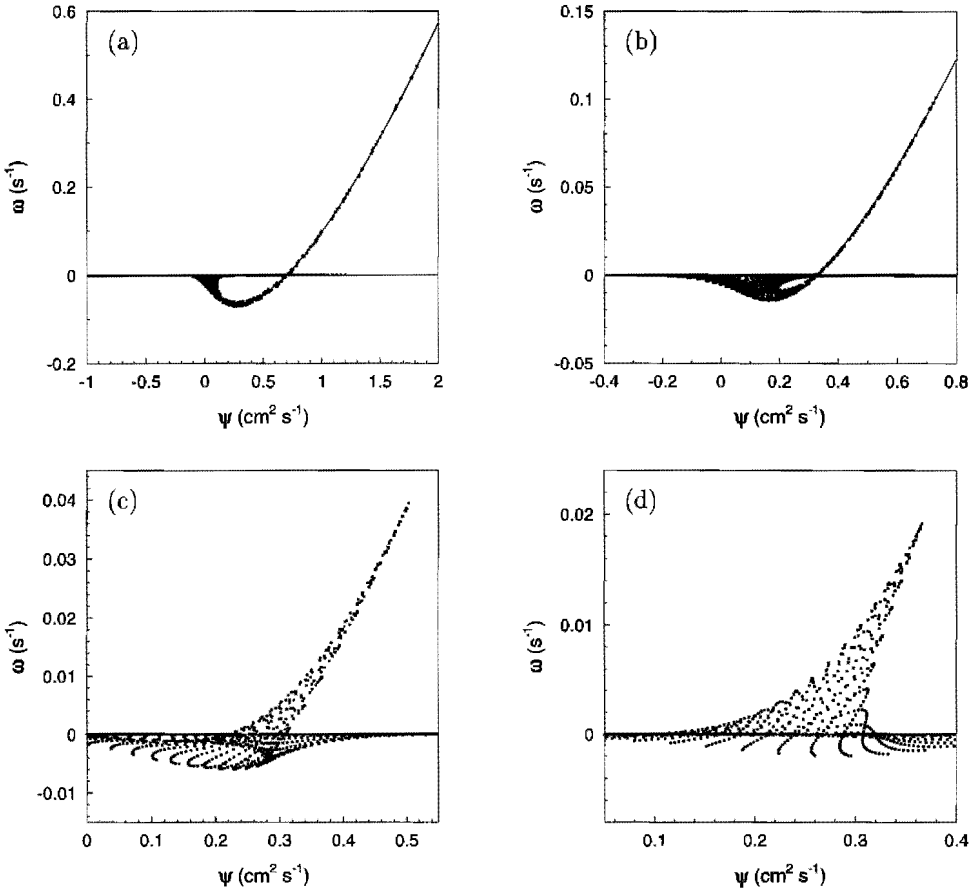


FIGURE 3.20: Sequence of numerically obtained (ω, ψ) -scatter plots: (a) $t = 120 \text{ s}$, (b) 360 s , (c) 600 s and (d) 840 s . The same initial parameters were used as in figure 3.19. The solid line corresponds to the (ω, ψ) -relationship according to the Gaussian vortex model, and has been least-square fitted to the numerical data for $\omega = 0.25\omega_m$. The maximum vorticity decreased from $\omega_m = 0.50 \text{ s}^{-1}$ at $t = 120 \text{ s}$ to $\omega_m = 0.019 \text{ s}^{-1}$ at $t = 840 \text{ s}$. The results may be compared with those in figure 3.12.

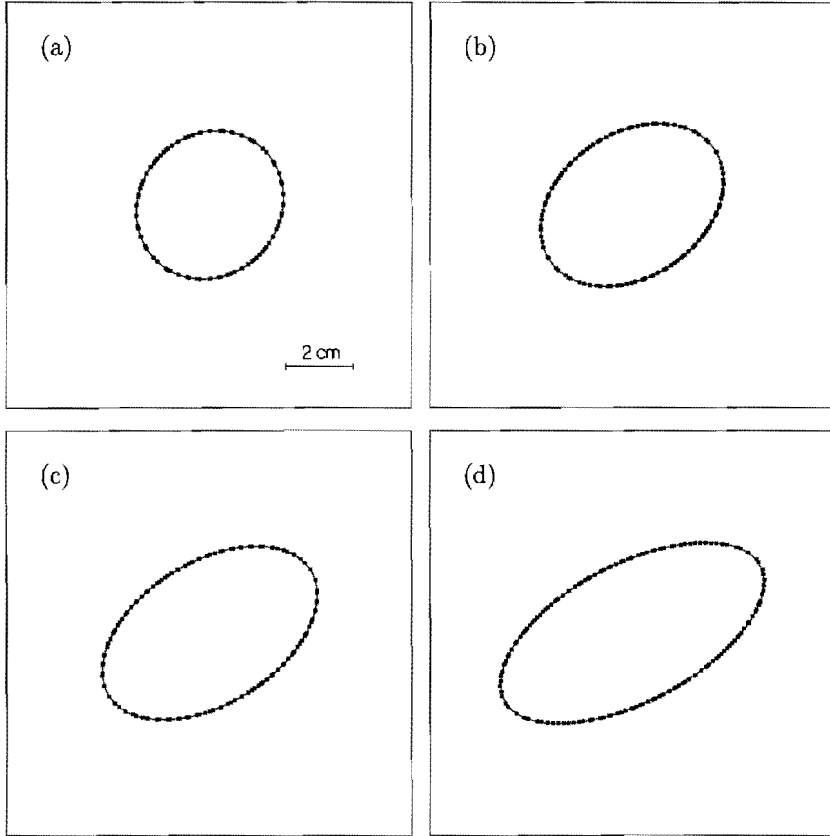


FIGURE 3.21: Typical discretized vorticity contours $\omega = \bar{\omega} = 0.697\omega_m$ of a vortex in a strain flow at four different times, viz. at (a) $t = 420$ s, (b) 600 s, (c) 720 s and (d) 840 s. A perfect elliptic contour (solid line) has been fitted to each numerically obtained contour. Numerical parameters as in figure 3.19.

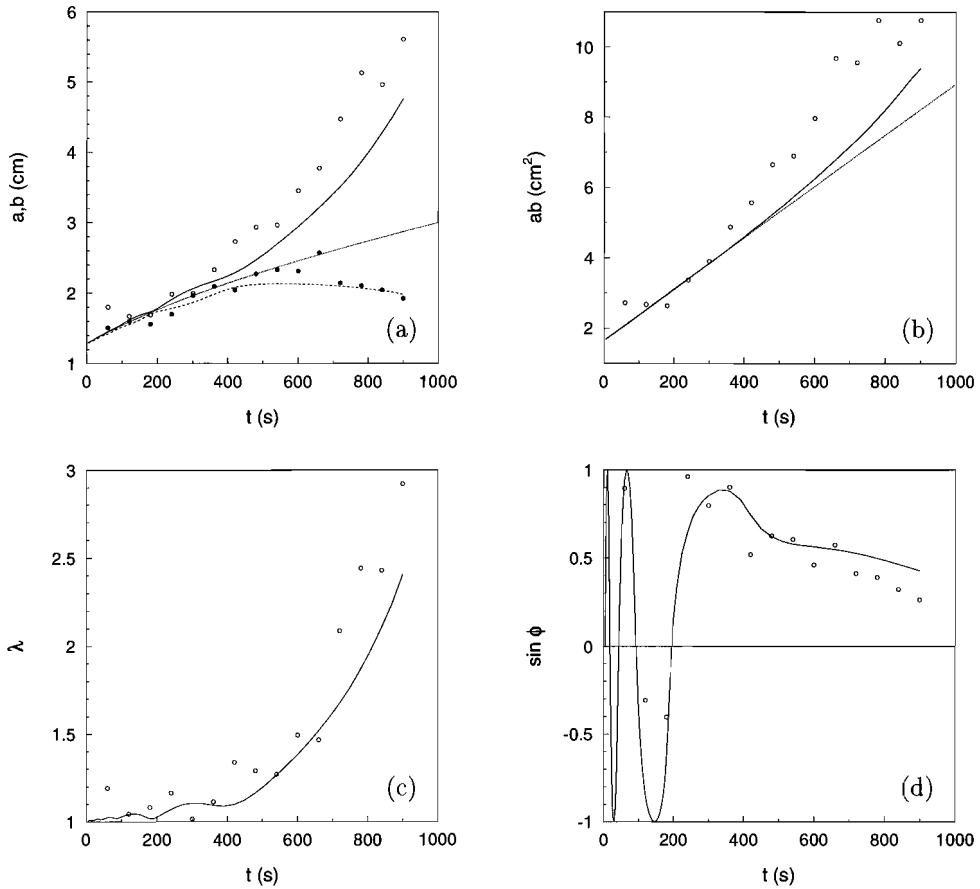


FIGURE 3.22: (a) Graph showing the calculated time-evolution of the principal axes a and b , which are represented by the solid and dashed line, respectively. The experimentally obtained evolutions of a and b are indicated by the open and filled circles, respectively. Also shown are the temporal evolution of the area ab (b), the aspect ratio λ (c), and the orientation ϕ (d) of the vortex. The calculated values are indicated by solid lines, whereas the observed data are represented by open circles. The dotted lines represents the radial expansion of a Gaussian vortex without background flow. All values have been obtained from the discretized vorticity contour $\omega = 0.697\omega_m$ and the same numerical parameters have been used as in figure 3.19.

monotonically and are very close to each other. However, at a later stage, an accelerated growth of a is observed, whereas b eventually decreases in time. In order to understand this behaviour, the product ab , which represents the area of the specific ellipse, is plotted in figure 3.22(b) (solid line) along with the evolution of the growing area r^2 of a vortex in a still ambient fluid (dotted line). To be more specific, r^2 represents the area enclosed by the circular vorticity contour $\omega = \bar{\omega}$, of which the radial expansion is exclusively caused by horizontal diffusion (note that $r^2 \sim r_m^2 = 2\nu t$, which can be derived from (3.4) and (3.8)).

Initially, the values of ab coincide with the curve $r^2(t)$, which means that the growth of the elliptic area is caused by pure horizontal diffusion. However, at a later stage ($t \approx 400$ s), ab increases faster than predicted by pure horizontal diffusion. This additional growth of ab may be due to an accelerated outward diffusive flux of vorticity. In figure 3.19 it was shown that the ring of negative vorticity is carried away by the strain flow. Since the presence of this ring opposes the radial expansion of the vortex, the accelerated diffusive flux is probably caused by the removal of surrounding negative vorticity. Similar results were obtained by Mariotti, Legras & Dritschel (1994) in their numerical study on monopolar vortices (of single-signed vorticity) in a shearing background flow.

In figure 3.22(a), the time-evolutions of a and b are compared with the radial growth $r(t)$ of a vortex in a still ambient fluid (dotted line). At first, both a and b are close to $r(t)$ and show weak-amplitude oscillations, but later on, the values of the principal axes diverge from the curve corresponding to pure viscous diffusion. By plotting the aspect ratio $\lambda = a/b$ against time in figure 3.22(c), it is obvious that this divergence is due to the elongation of the vortex. Likewise, the weak amplitude oscillations in a and b are related to the shape oscillations of the vortex. Hence, figure 3.22(a) shows the strain-induced evolution of the principal axes superimposed on the pure diffusive expansion of the vortex.

In figure 3.22(d), the calculated orientation of the vortex is plotted versus time (solid line). Initially, the vortex rotates around its centre until $t \approx 350$ s, at which time the rotation speed has decreased to zero ($\dot{\phi} = 0$). The rotational motion can be explained by the presence of the two satellites of negative vorticity which surround the vortex core. This situation is very similar to that of a tripolar vortex, as observed in the laboratory by Kloosterziel & van Heijst (1991), which rotates around its centre in a solid-body-like fashion. In the next stage, the vortex rotates backwards, though its orientations remains close to 45 degrees with respect to the horizontal strain axes. During this stage, the satellites are being separated from the vortex by the ambient flow. Finally, after $t \approx 700$ s, the rotation accelerates and the vortex turns towards the horizontal strain axis.

Figure 3.22(a) also shows the evolution of the axes a and b as observed in the laboratory (open circles). Initially, the measured data are in good agreement with the numerical results, but for larger times ($t > 300$ s), the observed data overshoots the numerically obtained values. In figure 3.22(b) a similar behaviour can be observed: after $t \approx 300$ s, the measured elliptic area ab increases faster than expected from the numerical model.

The measured values of λ and ϕ are plotted versus time in figure 3.22(c) and (d), respectively. Taking into account the experimental errors, which are estimated to be about 10–20% for both λ and ϕ , in each case a good agreement is obtained with the calculated evolution for a long time. In the final stage of the evolution, however, the vortex elongation

and vortex tumbling proceed faster than expected from the numerical model.

A few possible causes may be considered for the accelerated evolution of the laboratory vortex. First of all, the growing strain rate e was neglected in the numerical model, whereas the strain rate measurements (see figure 3.7) indicate that e increases about 5–10% during the whole vortex evolution (assuming that the growth of the strain rate is not affected by the presence of the vortex). However, a second numerical simulation, in which the strain rate was allowed to increase by 10% between $t = 0$ and $t = 960$ s, demonstrated that this effect gives only a minor contribution to the vortex evolution, and can not explain the deviations with the experiments completely.

Secondly, the dynamics in the computational domain may be different from that in an infinite plane: the numerical boundary conditions impose a pure strain flow along the boundaries, which is actually wrong if non-zero vorticity is present within the bounded domain. Therefore, another numerical simulation was performed in which the size of the computational domain was doubled and a 512×512 grid was used to retain the resolution. However, no significant difference could be observed with the former simulations.

It may also be that the three-dimensional evolution of the laboratory vortex is only partly represented by the source solution (3.31). Since detailed measurements about the vertical motion are lacking, it is difficult to conclude about the influence of additional three-dimensional effects. Nevertheless, the calculated decay of the maximum vorticity is in good agreement with the experimental data, as can be inferred from figure 3.14. Moreover, it was shown in chapter 2 that the evolution of a monopolar vortex in a still ambient fluid is accurately described by the present model.

The faster destruction of the laboratory vortex may be ascribed to the non-uniformity of the experimental strain flow. As can be inferred from figures 3.6(c) and (d), the local strain rates near the discs are larger than the uniform strain rate near the centre of the flow field. Consequently, the velocities near the discs are also larger than expected from the central part of the flow domain. This effect is illustrated most clearly by the accelerated advection of negative vorticity, as observed in the laboratory. Because of the horizontal expansion and the fast growing aspect ratio of the vortex, part of the vortex core may fall into the intensified strain rate region, which will result in both an accelerated elongation and a faster rotation of the vortex.

3.7 Discussion and conclusions

In this chapter, the dynamics of monopolar vortices in a strain flow was investigated based on laboratory experiments that were performed in a stratified fluid. The laboratory observations revealed that the evolution of shielded monopolar vortices in a strain flow is characterized by the initial deformation of the vortex into a tripolar-like structure, followed by the shedding of the accompanying satellites. In the next stage, the vortex was observed to evolve quasi-steadily, as evident from the (ω, ψ) -scatter plots. Finally, the vortex was torn apart along the horizontal strain axis owing to the diffusive decay of vorticity. This behaviour appeared to be independent of the absolute strain rate, which only determined

the speed of the vortex evolution, but not the evolution process itself.

The dynamics of the vortex core was very similar to that of an elliptic patch of uniform vorticity in a strain flow. At high vorticity amplitudes the instantaneous vorticity contours were close to ellipses with nearly the same aspect ratios and orientations. Moreover, the laboratory observations were generally in good qualitative agreement with the calculated vortex evolution according to the extended Kida model.

The preservation of the elliptic shape of the vortex core is consistent with the fact that elliptic shapes are preserved in a pure strain flow (see Kida (1981) and Legras & Dritschel (1991)). This assertion is supported by numerical simulations of non-uniform vortices in strain and shear flows (see Legras & Dritschel (1993, 1994)), in which the shapes of the higher vorticity contours were observed to remain close to elliptic. It is worth mentioning that nearly elliptic vortices were also found in numerical simulations by Melander, McWilliams & Zabusky (1987), who considered the relaxation of smooth elliptic vorticity distributions towards axisymmetry, and in laboratory experiments by Hernan & Jimenez (1982), who observed elliptic-like vortex structures in free-shear layers.

As a second approach, the quasi-two-dimensional vorticity equation was solved numerically by a finite-difference method to account for both the non-uniform vorticity distribution of the laboratory vortex and the horizontal diffusion of vorticity. The calculated vortex evolution was very similar to that observed in the laboratory. Furthermore, it was shown that the removal of the surrounding negative vorticity induces an accelerated horizontal growth of the vortex, which was also observed in a numerical study by Mariotti, Legras & Dritschel (1994). Owing to the non-uniformity of the experimental strain flow, the laboratory vortex evolved faster than in the numerical simulation.

Chapter 4

Kinematic properties of monopolar vortices in a strain flow

4.1 Introduction

The problem of an elliptic patch of uniform vorticity embedded in a uniform shear flow was solved analytically by Chaplygin (1899) and also by Kida (1981) (see Meleshko & van Heijst (1994a) for a review on Chaplygin's earlier work). In chapter 3, the Kida model was compared with laboratory observations and was found to describe the basic dynamical features of the observed flow very well. Since analytical solutions for distributed vortices in background flows are hard to obtain, attention has been focused mainly on numerical techniques. For example, the vortex may be represented by a stack of uniform vorticity patches, of which the corresponding boundaries are followed in time. This contour dynamics approach was used to study the evolution of distributed vortices in straining and shearing background flows (see for example Dritschel (1989)).

However, the strongest abstraction of a monopolar vortex is a point vortex, which is characterized by an irrotational velocity field with the vorticity concentrated in a singular point. Since the point vortex cannot be deformed by definition, it is an unsuitable model for describing the dynamics a monopolar vortex in strain and shear flows. This may explain why until now, not much attention has been paid to the problem of a point vortex embedded in an ambient flow, apart from the analytical study by Kimura & Hasimoto (1985) in which the motion of two identical point vortices in a uniform shear was considered. Nevertheless, the point vortex may be well suited for describing the kinematic features of monopolar vortices in a background flow.

In the present chapter, it will be examined whether the point-vortex model can explain the main advection properties of monopolar vortices in a strain flow. For this purpose, a comparison will be made with stratified fluid experiments, in which the strain flow and the monopolar vortex were generated with the same techniques as described in chapter 3. In order to measure the characteristics of the horizontal velocity field and to trace individual particles, the laboratory flow was visualized with passive tracers. In addition, the fluid

was coloured with dye to obtain qualitative information about the evolution of passive tracer distributions. Furthermore, the effect of the continuous vorticity distribution on the advection properties will be investigated by performing a full numerical simulation of the planar flow.

This chapter is organized as follows. In section 4.2, a description will be given of the devices used to generate the monopolar vortices and the strain flow, as well as a discussion of the method of analysis. Next, the laboratory observations presented in section 4.3 will be compared with the advection properties predicted by the point-vortex model (section 4.4). The effect of the spatial distribution of vorticity on the advection properties will be examined in section 4.5. Finally, the discussion and conclusions are presented in section 4.6.

4.2 Experimental set-up

The experiments were carried out in a perspex tank of horizontal dimensions 100×100 cm and depth 30 cm. The tank was filled with a two-layer fluid in which fresh water was lying over salty water. Typically after a few days, an almost linear density stratification was formed near the mid-plane of the tank within a layer of approximately 10 cm thickness. For the experiments presented in this chapter, the buoyancy frequency N at mid-depth was typically 3.0 rad s^{-1} .

The strain flow was generated with the same technique as introduced in chapter 3, i.e. at the mid-level of the tank, four horizontal discs (with diameter d and thickness h) were positioned at the corners of a square and were rotated with a constant angular speed Ω_d in the directions as indicated in figure 3.1. The diagonal distance D between the centres of the discs was either 40 or 50 cm.

Typically one hour after the onset of rotation, the strain flow was quasi-steady and the monopolar vortex was generated in the centre of the mid-plane, either by a small spinning sphere or by the so-called tangential-injection method. In an experimental study by Flór & van Heijst (1996), it was shown that the motion of these monopolar vortices was confined to a thin disk-shaped region, and that the decay of the vertical vorticity was dominated by vertical diffusion. Furthermore, it was demonstrated in chapter 2 that both generation methods give rise to monopolar vortices with equal spatial vorticity distributions.

The sphere (with diameter 2.5 cm) was spun about its vertical axis in the mid-plane of the tank with a rotation speed Ω_s during a short time period δt . After the forcing was stopped (at $t = 0$ s), the sphere was carefully raised and removed from the tank. According to the tangential-injection method, an open thin-walled cylinder (with inner diameter 9.8 cm, thickness 0.1 cm and height 3 cm) was positioned at the mid-plane of the tank. Parallel to the inner wall of the cylinder, fluid was injected through a nozzle (with diameter 0.6 cm) at a constant rate Q during a time period δt . Care was taken that the injected fluid matched the density of the ambient fluid at mid-depth. After the injection was stopped (at $t = 0$ s), the fluid within the cylinder was allowed to develop into an axisymmetric swirling motion, and finally (after typically 30–60 s) the cylinder was carefully removed.

Small polystyrene particles with density 1.04 g cm^{-3} were added to the mid-level of the tank in order to measure the horizontal velocity field and to perform long-term particle tracking. The passive tracers were monitored continuously by a video camera, which was mounted at some distance above the tank, and the video images were stored on video tape. After the experiment was finished, the video tape was processed by the image analysis system *DigImage* (see Dalziel (1992)), which uses a particle-tracking method to determine velocities and trajectories of individual particles. In order to determine the vorticity ω and the stream function ψ , the measured velocity field was calculated on a rectangular grid of 30×30 grid points by a spline interpolation method (see Paihua Montes (1978) and Nguyen Duc & Sommeria (1988)). After that, the vorticity and stream function could be calculated in each grid point by numerical differentiation and integration, respectively.

Qualitative information about the flow field was obtained by adding fluorescent dye in the mid-plane of the vortex. The evolution of the dye pattern was recorded photographically by taking pictures from above with a remote-controlled photo camera. The tangential-injection method enabled to add dye during the forcing. In contrast, when the vortex was generated by the spinning sphere, dye was added by hand with a syringe shortly after the sphere was removed from the tank.

4.3 Laboratory observations

In figure 4.1, a sequence of photographs is given which show dye visualizations of a monopolar vortex in a strain flow. The vortex was generated by the spinning sphere and part of the fluid was coloured with fluorescent dye between $t = 30 \text{ s}$ and $t = 60 \text{ s}$. Initially, an almost circular patch of dye is present near the centre of the flow field, as can be observed in figure 4.1(a), which gradually becomes more elliptic, see (b). In the next stage (see (c) and (d)), two filaments of dye are being shed from the vortex. Comparison of the photographs in figures 4.1(b)–(d) reveals that the elliptical vortex core remains oriented at an angle of approximately 45 degrees with respect to the horizontal strain axis. Also note that the vortex core becomes more elliptic when time increases. However, in the final stage (see (e) and (f)), the orientation of the elliptical vortex changes and the vortex is completely torn apart along the horizontal strain axis. The different intensities of dye concentration in the photographs of figure 4.1 are due to the initially non-uniform dye distribution and the fact that, unintentionally, fluid beneath and above the mid-plane was also coloured with dye.

Another sequence of photographs is presented in figure 4.2, which show the strain-induced evolution of a monopolar vortex that was generated by the tangential-injection method. It is important to note the vortex thus obtained has the same flow characteristics as the spinning sphere (see chapter 2). The tangential-injection method is particularly useful to colour the vortex in its entirety. The photograph in figure 4.2(a) displays the circular dye pattern just after the cylinder had been removed from the tank. Subsequently, two patches of dye are being detached from the vortex (see (b)–(d)), leaving behind an elliptic-like vortex core with a virtually fixed orientation. The asymmetric shedding of dye is probably due to small deviations from axisymmetry in the initial vorticity distribution.

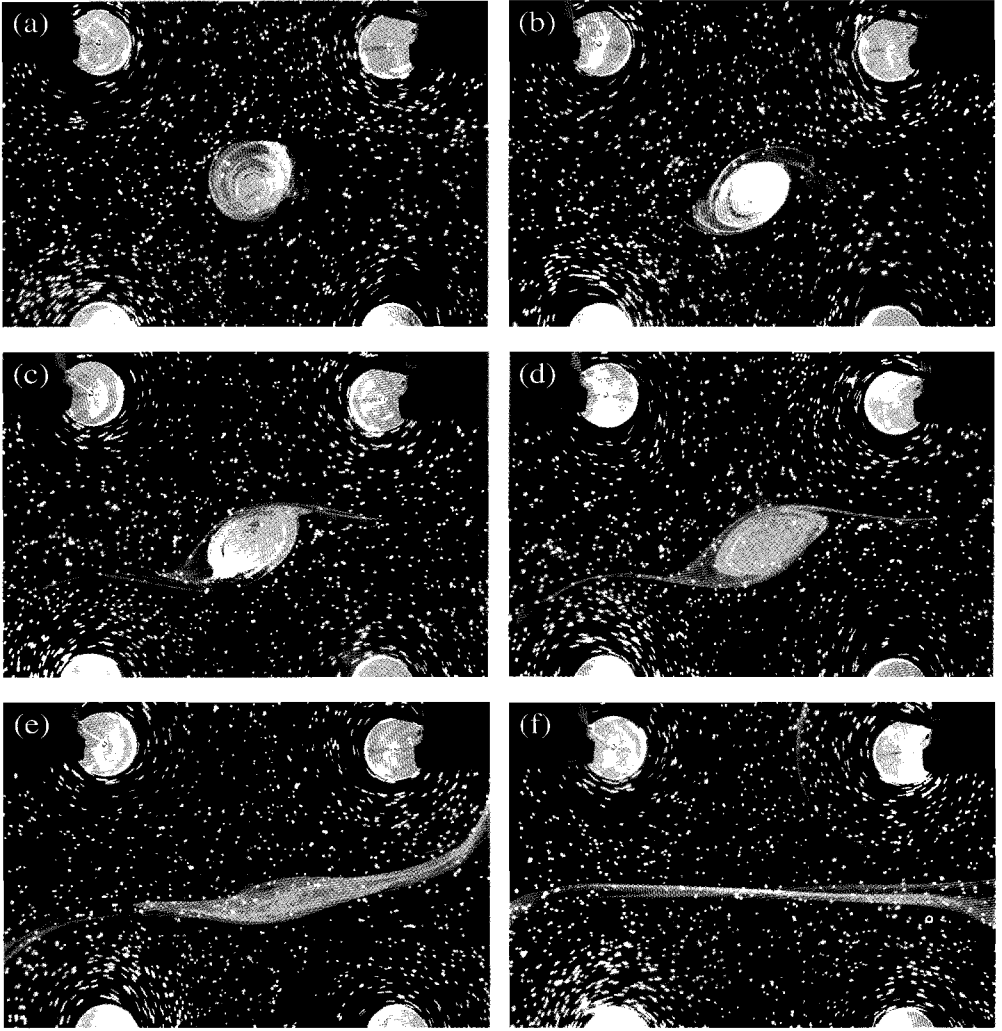


FIGURE 4.1: Evolution of a monopolar vortex in a strain flow with $e = 2.0 \times 10^{-2} \text{ s}^{-1}$. The vortex was generated by the spinning sphere. After the forcing was stopped and the sphere was removed, fluorescent dye was carefully injected in the mid-plane of the vortex. The photographs correspond with times (a) $t = 66$ s, (b) 115 s, (c) 160 s, (d) 180 s, (e) 280 s and (f) 430 s. Experimental parameters: $\Omega_d = 11.4$ rpm, $D = 40$ cm, $d = 6$ cm, $h = 1$ cm, $\Omega_s = 320$ rpm, $\delta t = 10$ s and $N = 3.2 \text{ rad s}^{-1}$.

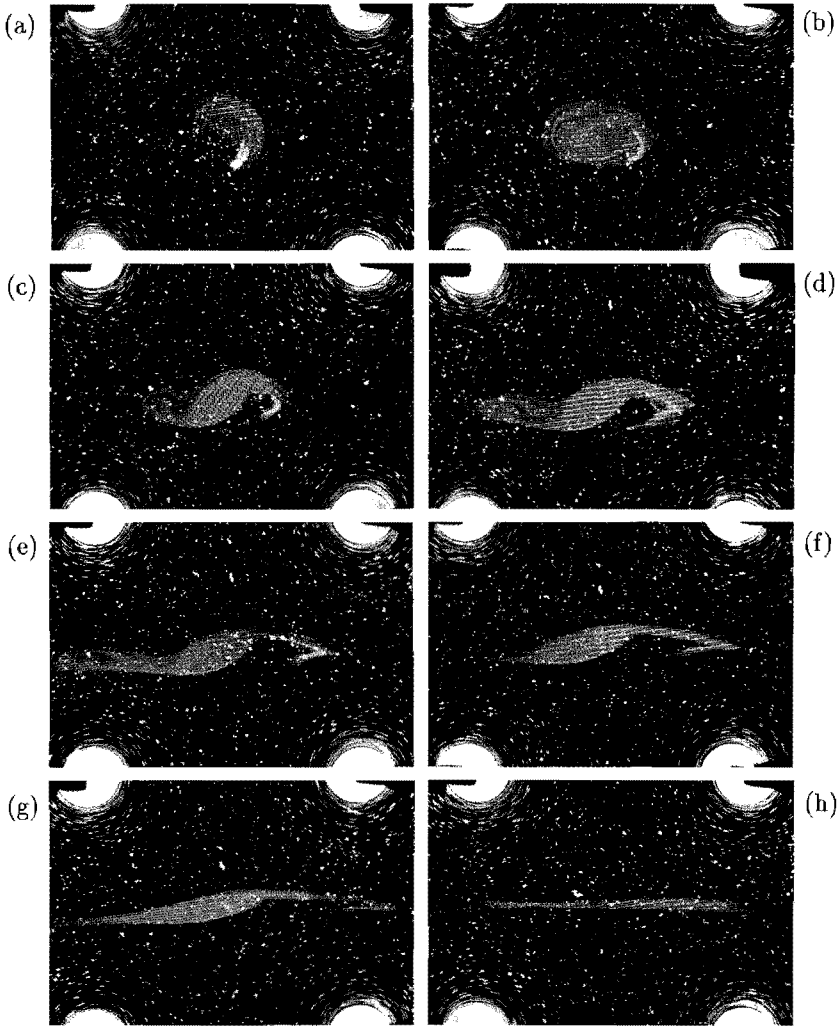


FIGURE 4.2: Dye visualization of a monopolar vortex in a strain flow with $e = 0.30 \times 10^{-2} \text{ s}^{-1}$. The vortex was generated by the tangential-injection method. The photographs correspond with times (a) $t = 103 \text{ s}$, (b) 273 s , (c) 393 s , (d) 513 s , (e) 633 s , (f) 753 s , (g) 873 s and (h) 1413 s . Experimental parameters: $\Omega_d = 1.9 \text{ rpm}$, $D = 50 \text{ cm}$, $d = 10 \text{ cm}$, $h = 0.5 \text{ cm}$, $Q = 2.0 \text{ ml s}^{-1}$, $\delta t = 10 \text{ s}$ and $N = 3.3 \text{ rad s}^{-1}$.

Another cause might be the presence of internal wave motions which inevitably emerged after the lifting of the cylinder. Finally, see (e)–(h), the elliptical vortex core rotates towards the horizontal strain axis and is completely torn apart into a thin horizontal filament.

Some more insight in the advection properties of passive scalars may be gained by considering some quantitative observations of the fluid motion. Figure 4.3(a) shows the digitized trajectories of tracer particles in the mid-plane of the tank during the intermediate stage of the vortex evolution. The basic straining flow and the swirling motion induced by the vortex are clearly visible. Apparently, near the centre of the flow field, fluid particles orbit along elliptic-like curves which are oriented at an angle of approximately 45 degrees with respect to the horizontal strain axis. Moreover, it can be observed from the lengths of the streaks that the flow field contains two stagnation points.

The velocity vector field associated with the instantaneous particle movements is given in figure 4.3(b), and again, the stagnation points are clearly visible. After interpolation of the measured velocity field on a rectangular grid, see figure 4.3(c), the stream function could be determined, as shown in figure 4.3(d). Close to the vortex centre, the streamline pattern is characterized by closed streamlines, whereas at larger radii, the contours are apparently ‘open’. If the flow were steady, the fluid contained in the region of closed streamlines would endlessly revolve around the vortex centre. Following Kelvin (see Thomson (1867)), this region of trapped fluid will be referred to as the ‘atmosphere’, which is bounded by two streamlines that pass through both stagnation points. The boundary of the atmosphere is usually called the ‘separatrix’.

Typical long-term particle trajectories are presented in figure 4.4. Figure 4.4(a) shows the path line of a tracer that was initially located well inside the atmosphere (indicated by the filled circle). During its first revolution, the tracer describes a nearly circular orbit. However, when time increases, the path line gradually becomes more elliptic, and in the final stage of the evolution, the tracer is advected into the ambient flow and moves away from the vortex. Figure 4.4(b) shows the trajectories of two particles that were initially located close to each other. Their positions at $t = 91$ s and at later times are marked by filled and open circles, respectively. At first, both particles follow nearly the same path, but later on, their path lines diverge. The tracer that was initially ahead of the other is soon sept away by the strain flow and leaves the bounding domain at $t = 691$ s. In the meantime, the remaining particle still continues its excursion around the vortex centre for a while, but in the final stage, this tracer is also carried away by the ambient flow and reaches the bounding box in figure 4.4(b) at $t = 1089$ s.

In order to explain the kinematic properties described above, in the next section the laboratory flow will be modelled by a simple point vortex placed in the centre of a pure strain flow. Also the viscous decay of the vortex will be reckoned with by this point-vortex model.

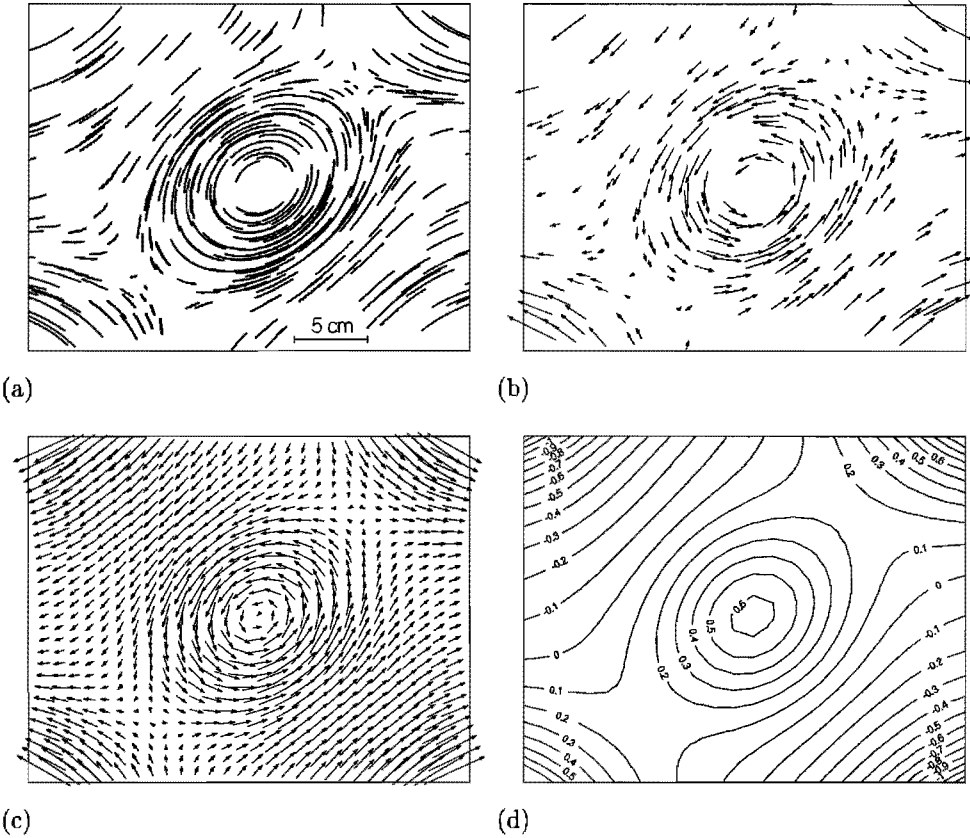


FIGURE 4.3: (a) Digitized particle paths corresponding to the quasi-stationary stage of a monopolar vortex embedded in a strain flow. The tracer particles were monitored for 40 s, starting at $t = 420$ s. Also shown are (b) the measured velocity vectors at $t = 420$ s as obtained by *DigImage*, (c) the interpolated velocity field, and (d) the corresponding streamline pattern. Experimental parameters: $\Omega_d = 1.9$ rpm, $D = 50$ cm, $d = 10$ cm, $h = 0.5$ cm, $\Omega_s = 150$ rpm, $\delta t = 15$ s and $N = 2.8$ rad s⁻¹.

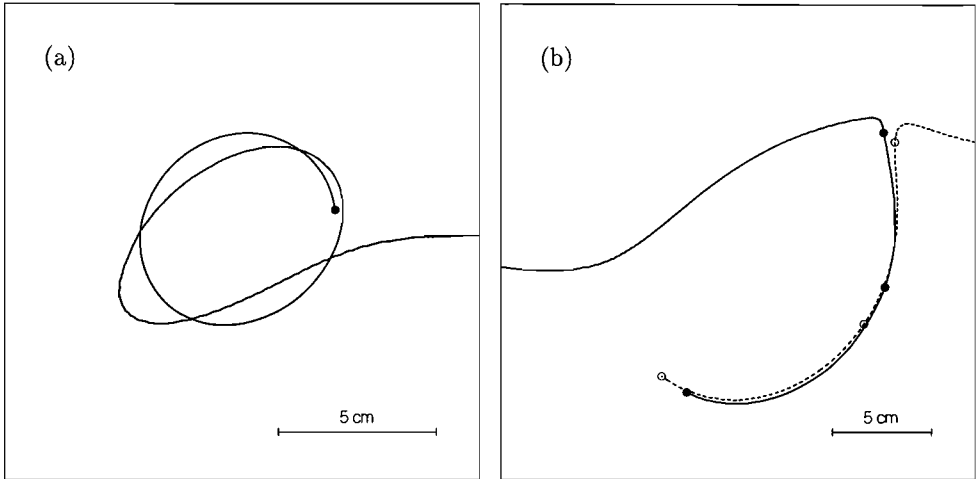


FIGURE 4.4: (a) Measured trajectory of a particle that was initially located in the core of the vortex. The starting point of the trajectory (at $t = 123$ s) is marked by a filled circle and the particle was followed up to $t = 791$ s. Experimental parameters: $\Omega_d = 3.0$ rpm, $D = 40$ cm, $d = 10$ cm, $h = 0.5$ cm, $\Omega_s = 162$ rpm, $\delta t = 15$ s and $N = 2.8$ rad s^{-1} . (b) Measured trajectories of two nearby particles that were initially located close to the separatrix. The positions of the tracers at $t = 91$ s, 225 s and 380 s are indicated by filled and open circles. The particles reach the edge of the bounding box at $t = 691$ s (dashed line) and $t = 1089$ s (solid line), respectively. Experimental parameters as in figure 4.3.

4.4 Advection properties of the point-vortex model

4.4.1 Point-vortex model

For a qualitative description of the laboratory observations shown in the preceding section, the monopolar vortex will be represented by a point vortex. Although this is a very crude abstraction of the actual flow, it will be shown the point-vortex model can explain the main features observed in the experiments. If the vortex is placed in the centre of the strain flow, the Eulerian velocity field is given by

$$u_r = er \cos 2\theta \quad (4.1)$$

$$u_\theta = -er \sin 2\theta + \frac{\gamma}{2\pi r}, \quad (4.2)$$

where u_r and u_θ are the radial and azimuthal velocity components, respectively, and polar coordinates (r, θ) have been used for convenience. The last term in (4.2) represents the contribution from the point vortex with strength γ , whereas the other terms in (4.1) and (4.2) represent the strain flow contribution, with e the rate of strain.

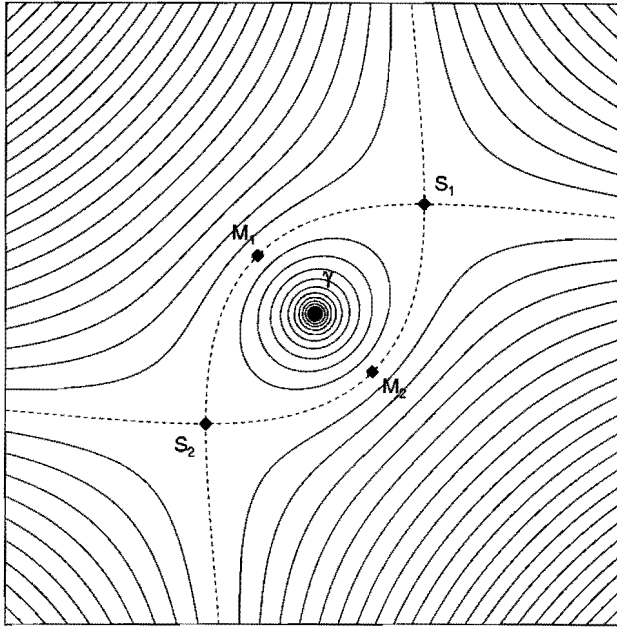


FIGURE 4.5: Streamline pattern associated with a point vortex located in the centre of a pure strain flow. The streamlines that intersect both stagnation points (marked by S_1 and S_2) are indicated by the dashed lines. At the points marked by M_1 and M_2 , the distance between the separatrix and the point vortex is minimum.

The stream function associated with this velocity field may be expressed as

$$\psi = \frac{1}{2}er^2 \sin 2\theta - \frac{\gamma}{2\pi} \ln r + C, \quad (4.3)$$

where C is a constant. The corresponding streamline pattern is plotted in figure 4.5, and has geometrically similar streamlines for all values of γ and e . The flow contains two stagnation points, marked S_1 and S_2 , respectively, which are the points of intersection of the dashed streamlines. Comparison with the experimentally obtained streamline plot in figure 4.3(d) reveals a good qualitative agreement. In both cases, the flow contains two stagnation points and a separatrix. Furthermore, the closed streamlines may be approximated by ellipses which are oriented at an angle of 45 degrees with respect to the horizontal strain axis.

Four extremal points may be identified on the boundary of the atmosphere: at the stagnation points S_1 and S_2 , the distance to the point vortex is largest, whereas at M_1 and M_2 , the distance to the centre of the flow field is minimum. The positions (r_S, θ_S) of the stagnation points can be calculated quite straightforwardly by equating both (4.1) and

(4.2) to zero, which yields

$$r_S = \left(\frac{\gamma}{2\pi e} \right)^{1/2} \quad (4.4)$$

$$\theta_S = \frac{\pi}{4} + k\pi, \quad (4.5)$$

with k being an integer.

This radial distance r_S will be used to nondimensionalize the radial coordinate, i.e. $\xi \equiv r/r_S$. Also a dimensionless stream function may be defined as $\Psi \equiv 4\pi\psi/\gamma$, with

$$\Psi(\xi, \theta) = \xi^2 \sin 2\theta - 2 \ln \xi - 1, \quad (4.6)$$

where the constant C in (4.3) has been chosen such that the separatrix is represented by $\Psi = 0$. Likewise, time is nondimensionalized as $t^* \equiv et$.

It can be reasoned from the symmetry in the flow pattern that an imaginary line through the extremal points M_1 and M_2 makes an angle θ_M of 135 degrees with the horizontal. In order to find this orientation θ_M analytically, it is convenient to calculate the derivative of ξ with respect to θ at the boundary of the atmosphere:

$$\left. \frac{d\xi}{d\theta} \right|_{sep.} = \frac{-\xi^3 \cos 2\theta}{2 \ln \xi}. \quad (4.7)$$

By equating (4.7) to zero, it follows indeed that $\theta_M = \frac{3\pi}{4} + k\pi$. Now, the minimum radial distance between the separatrix and the vortex centre can be found by substituting θ_M into (4.6), which yields

$$\xi_M^2 = \exp \left[- \left(1 + \xi_M^2 \right) \right]. \quad (4.8)$$

This transcendental equation can be solved iteratively and has the solution $\xi_M \approx 0.528$.

4.4.2 Contour kinematics

In order to investigate the deformation of an arbitrary patch of passive fluid, it suffices to only trace its boundary due to the conservation of area. The evolution of this bounding contour may be calculated numerically by applying the method of contour kinematics. This method was discussed in detail by Meleshko & van Heijst (1994b).

The passive contour is represented by a number of nodes (up to $M = 5000$), the positions of which are calculated by solving (4.1) and (4.2) with a Runge-Kutta method with variable time step and order (see Hairer, Nørset & Wanner (1987)). In general, this contour will be stretched and folded during the flow evolution, so that its length may increase considerably. Therefore, extra nodes will be added if the distance between two nodes becomes larger than a prescribed threshold value, or if the angle spanned by three adjacent tracers becomes smaller than 150° , i.e. the curvature of the contour becomes locally too large. The position of each new particle is calculated by first adding a node at $t = 0$ between the corresponding adjacent particles and then calculating its evolution until

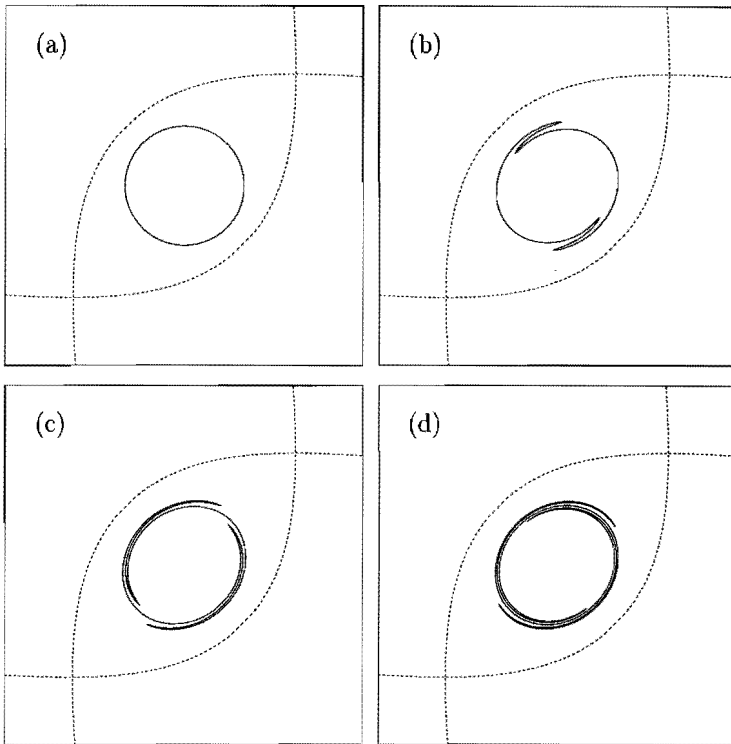


FIGURE 4.6: Calculated evolution of an initially circular contour of passive tracers (with radius $\xi_0 = 0.38$), which is located within the separatrix (dashed line): (a) $t^* = 0$, (b) 2.0, (c) 4.0 and (d) 6.0.

the time is reached at which the extra particle had to be added. Conversely, particles are removed if the distance between two adjacent tracers becomes too small so as to prevent them from being numerically indistinguishable and to speed up the numerical integration. The accuracy of the numerical algorithm was checked by calculating the area enclosed by the passive contour using Stokes' theorem.

In the laboratory experiments, the fluid was initially coloured within an almost circular region. Therefore, as an initial condition, a circular contour of radius ξ_0 is taken on which the nodes (typically 60) are distributed uniformly. For the moment, the viscous decay of the vortex will be excluded, so that ξ_0 is the only free parameter in the point-vortex model. Then, two different initial situations may be considered in which the enclosed area is either lying entirely inside the atmosphere (figure 4.6(a)) or is partly overlapping the separatrix (figure 4.7(a)).

Figure 4.6 shows the evolution of an initially circular contour with radius $\xi_0 = 0.38$.

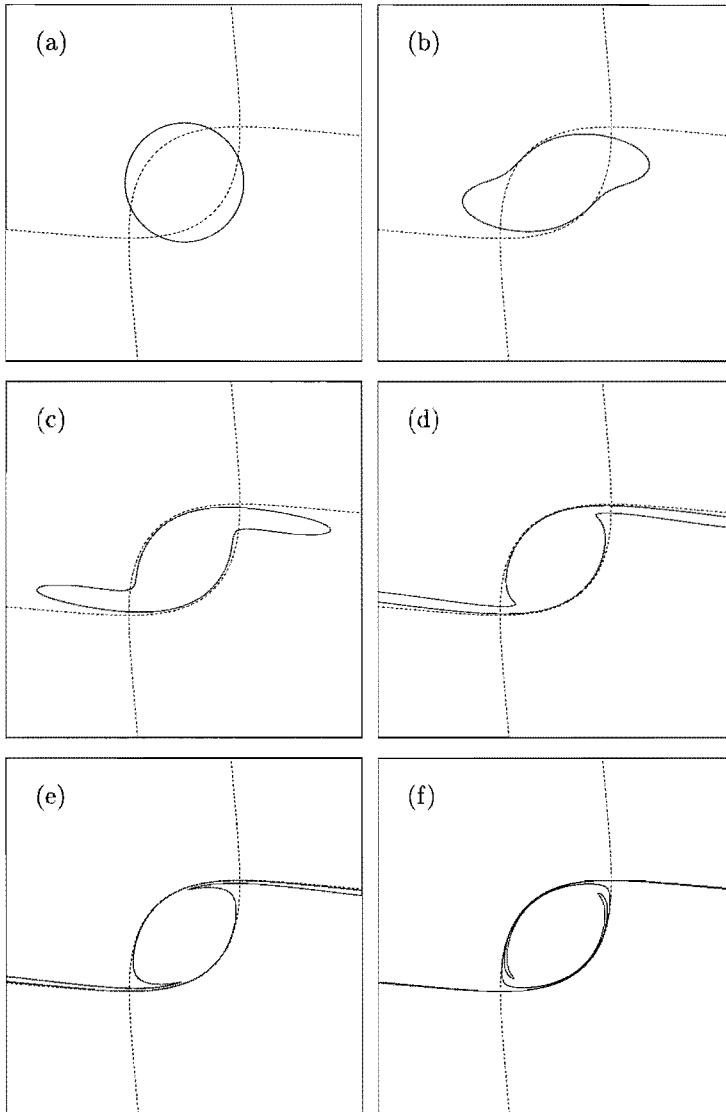


FIGURE 4.7: Calculated evolution of passive tracers, initially located on a circular contour of radius $\xi_0 = 0.76$, which are partly placed outside the separatrix (dashed line): (a) $t^* = 0$, (b) 0.5, (c) 1.0, (d) 1.5, (e) 2.0 and (f) 3.0.

Since $\xi_0 < \xi_M$, the entire contour is situated inside the atmosphere. When time increases, two tips arise (see (b)) which soon evolve into large spiral arms that are wrapped around the vortex (see (c)–(d)). The emergence of these filaments can be attributed to the elliptic-like shape of the streamlines (see figure 4.5). Furthermore, it is clear that in this case the passive tracers will never leave the atmosphere.

If part of the passive tracers is located outside the atmosphere, the material line evolves as displayed in figure 4.7 (with $\xi_0 = 0.76$). Tracers lying outside the atmosphere form two broad arms which are transported towards the stagnation points (see (b)–(c)). In the next stage, (d)–(f), these lobes are progressively elongated along the open streamlines, and consequently, the arms become thinner when time progresses. Inside the atmosphere a similar spiralled material contour arises like in figure 4.6, since only part of the atmosphere was initially enclosed by passive tracers. This spiral structure would not have been observed if the atmosphere were initially completely surrounded with passive tracers (e.g. $\xi_0 \geq 1$).

Since the monopolar vortex has a flat pancake-like shape, the circulation of the laboratory vortex (in the mid-plane) decays in time due to vertical diffusion of vorticity (see Flór & van Heijst (1996) and chapter 2). In order to model this effect, the strength of the point vortex is made time-dependent according to

$$\gamma(t) = \gamma_0 \exp\left(-\frac{t}{\tau}\right), \quad (4.9)$$

where γ_0 is the initial circulation and τ represents a characteristic e-folding time scale. In reality, the decay of circulation is not described by (4.9), but for a qualitative comparison with the experiments the exact functional relationship is not so important. The length scales will now be nondimensionalized by $r_{S,0} \equiv (\gamma_0/2\pi e)^{1/2}$, which is the radial distance to the stagnation points at $t^* = 0$.

In figure 4.8 the temporal evolution of passive tracers is shown for the decaying point vortex. Except for the condition $\tau^* = 4$, the same initial situation is taken as in figure 4.6 (i.e. $\xi_0 = 0.38$). Unlike the steady case, the area enclosed by the separatrix becomes smaller when time increases. Therefore, passive tracers which were initially trapped inside the atmosphere will eventually be forced to cross the bounding separatrix. As long as the passive tracers are lying inside the atmosphere, see figure 4.8(a,b), a similar qualitative behaviour can be observed as in figure 4.6. However, when time proceeds, the initially axisymmetric distribution of passive tracers becomes more elliptic. In the next stage, (c)–(f), the tracers leak through the separatrix and move away from the vortex. Eventually all tracers that were initially inside the atmosphere will be carried away by the ambient flow. Note that the filaments will not asymptotically coincide with the open streamlines that intersect both stagnation points (dashed lines). In fact, the filaments will cross these open streamlines due to the invariably changing streamline pattern.

Figure 4.9 displays the evolution of passive tracers for $\xi_0 = 0.76$ and $\tau^* = 4$. Initially, similar results are obtained as in the steady case (see figure 4.7). Again, two lobes of passive markers slide along the boundary of the atmosphere and are subsequently being elongated along the open streamlines. However, owing to the decay of circulation, the spiral structure inside the atmosphere does not show up and the expelled filaments cross the open

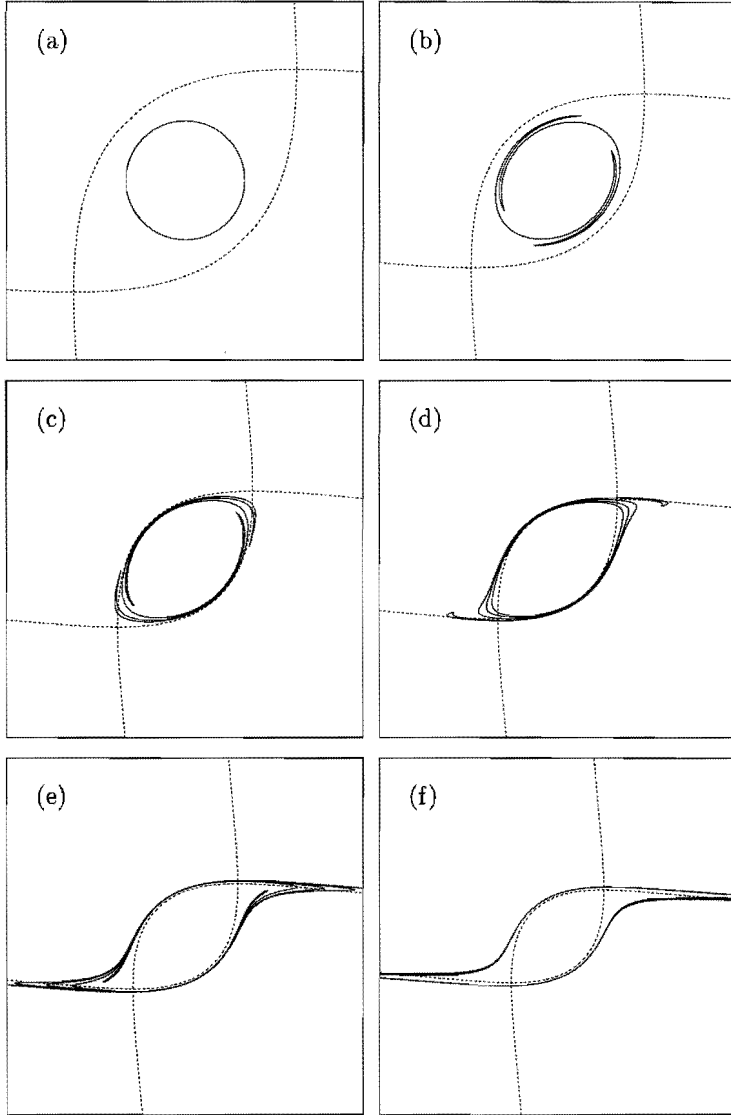


FIGURE 4.8: Temporal evolution of passive tracers for a decaying point vortex in a strain flow: (a) $t^* = 0$, (b) 2.0, (c) 4.0, (d) 5.0, (e) 6.0 and (f) 7.0. Numerical parameters: $\xi_0 = 0.38$ and $\tau^* = 4$.

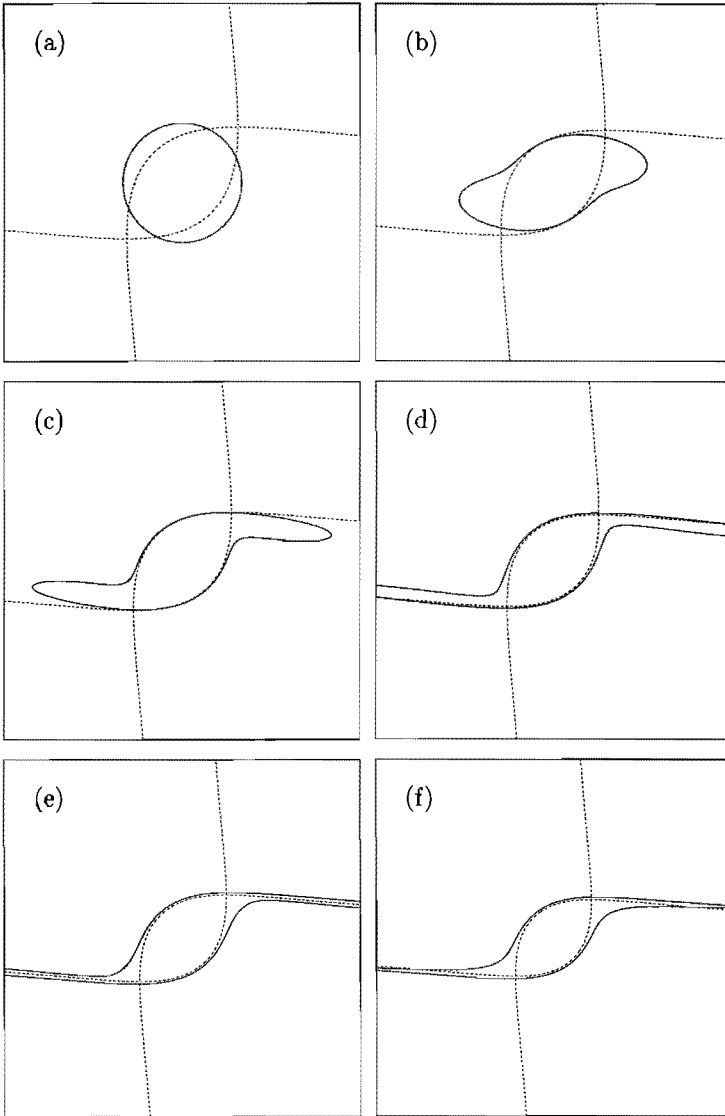


FIGURE 4.9: Temporal evolution of passive tracers for a decaying point vortex in a strain flow: (a) $t^* = 0$, (b) 0.5, (c) 1.0, (d) 1.5, (e) 2.0 and (f) 3.0. Numerical parameters: $\xi_0 = 0.76$ and $\tau^* = 4$.

streamlines indicated by the dashed lines in figure 4.9. When a larger e-folding time scale were taken, a similar tracer distribution would have been obtained inside the atmosphere as in figure 4.7. However, in the long run, these spiral arms would also disappear due to the decreasing area of the atmosphere.

4.4.3 Comparison with experimental results

Comparison of the numerical results depicted in figure 4.8 with the experimental observations shown in figure 4.1 reveals a very good qualitative agreement, at least until the final stage of the evolution. The similarity is obvious, given the deformation of the axisymmetric dye distribution into an ellipse shape, which is oriented at an angle of 45 degrees to the horizontal axis, and the shedding of thin filaments of passive tracers. Apparently, only fluid inside the atmosphere was initially coloured with dye. Likewise, the dye distributions shown in figure 4.2(a)–(d) are in excellent qualitative agreement with the numerical results presented in figure 4.9. Evidently, figure 4.2(a) corresponds to the case in which part of the fluid outside the atmosphere was coloured with dye.

However, the final stage of both observed evolution processes is not reproduced by the contour kinematics simulations. Experimentally, the elliptical vortex core rotates towards the horizontal strain axis, whereas the numerical results show that the core retains its orientation. The latter observation is not surprising, since the model flow contains geometrically similar streamlines at all times. The discrepancy between the point-vortex model and the laboratory observations can be attributed to the continuous spatial vorticity distribution of ‘real’ vortices, and this matter will be discussed in the next section, in which the passive tracer distributions of the laboratory experiments will be compared with those obtained by a full numerical simulation of the planar flow.

In order to investigate whether the point-vortex model can explain the experimentally observed behaviour of individual particles, a numerical simulation was performed in which two nearby tracers (labelled A and B) were followed in time. The time-evolution of the individual tracer positions was calculated by solving (4.1) and (4.2) with the same Runge-Kutta method as discussed before. Figure 4.10 shows the calculated trajectories of both tracers which were initially located inside the atmosphere at $(\xi, \theta) = (-1, \pi)$ and $(\xi, \theta) = (-0.993, \pi)$, respectively. The initial positions of both markers are indicated by the asterisk. The strength of the point vortex was allowed to decay in time with an e-folding time $\tau^* = 4$. Owing to the decay of circulation, the boundary of the atmosphere approaches the passive tracers, and consequently, the streamlines at the location of the tracers become more elliptic. As a result, the particle orbits also become more elliptic.

Although in the beginning both tracers follow virtually the same path, tracer A (which follows the dashed line) will move slower than tracer B (which moves along the solid line), because tracer A comes closest to the stagnation points. This can be observed in figure 4.10, where the locations of both particles have been marked at $t^* = 2.9, 3.6$ and 4.2 by open and filled circles, respectively. In the final stage, the curves diverge: tracer A is swept away by the ambient flow, whereas tracer B makes a final half loop around the point vortex before ending its periodic motion. Apparently, tracer B was still located inside the atmosphere

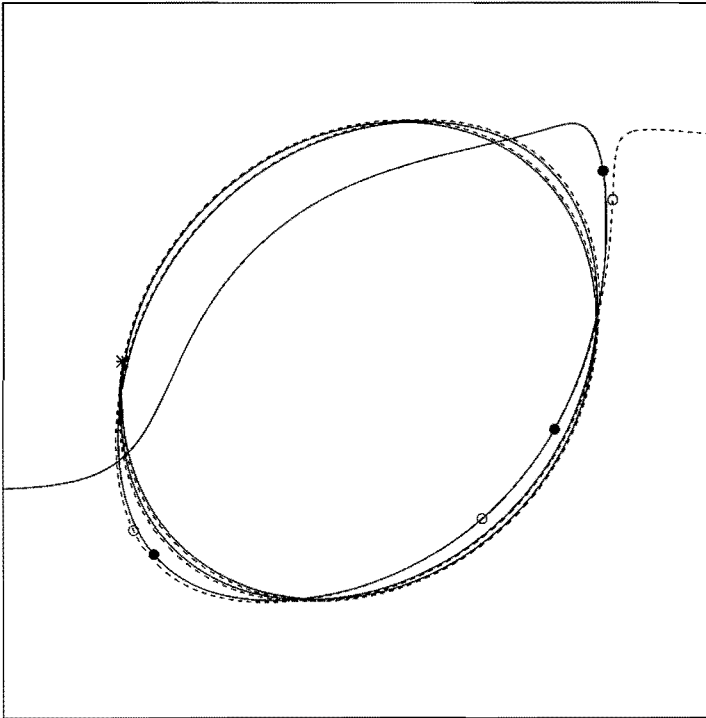


FIGURE 4.10: Trajectories of passive tracers initially located at $(\xi, \theta) = (-1, \pi)$ (dashed line) and $(\xi, \theta) = (-0.993, \pi)$ (solid line), respectively. The e-folding decay time is $\tau^* = 4$. The asterisk indicates the initial positions of both tracers, whereas the open and filled circles mark the locations of the tracers at $t^* = 2.9, 3.6$ and 4.2 .

when tracer *A* was shed into the ambient flow. It can be concluded from figure 4.10 that a small change in the initial position of passive tracers may have a dramatic effect on their subsequent movement.

Experimentally, the passive tracers behave quite similar to those indicated in figure 4.10. Both the increasing ellipticity of the particle orbits and the diverging particle trajectories of nearby tracers are apparent in figure 4.4. Note that in the final stage of the evolution, the particle followed in figure 4.4(a) moves asymptotically towards the horizontal strain axis, although it is expected from the point-vortex model that the tracer will first cross the horizontal strain axis before moving away from the vortex. This dissimilarity between the experimental observations and the point-vortex model can again be ascribed to the continuous spatial vorticity distribution of the laboratory vortices.

4.5 Effect of distributed vorticity on the advection properties

The final tilting and elongation of the coloured fluid as observed in the laboratory may be attributed to the fact that the vorticity of the laboratory vortex has a continuous spatial distribution. Contour dynamics simulations by Legras & Dritschel (1993) have shown that, after reaching a critical breaking value $(e/\omega_m)_c$, the vortex is rotated towards the horizontal strain axis and is simultaneously torn apart while the core is still of finite size. Similar results were found in chapter 3, in which the dynamics of monopolar vortices in a strain flow was studied.

In this section, the above scenario will be illustrated by a full numerical simulation of the strain-induced evolution of the monopolar vortex. In order to make a quantitative comparison with the dye-visualized laboratory observations, viscous effects will be accounted for.

It was shown in chapter 3 that in the mid-plane of a stratified fluid the strain-induced evolution of monopolar vortices can be described satisfactorily by the quasi-2D vorticity equation

$$\frac{\partial \omega}{\partial t} + J(\omega, \psi) = \nu \nabla_h^2 \omega - \frac{\omega}{2t} \quad (4.10)$$

and the relation

$$\omega = -\nabla_h^2 \psi, \quad (4.11)$$

with ω the vertical component of vorticity, ν the kinematic viscosity, ∇_h^2 the Laplace operator acting in horizontal directions, and J the Jacobian. The last term in (4.10) was added to mimic the diffusion of vorticity in the vertical direction, and is based on the assumption that at $t = 0$ the vorticity is confined in an infinitesimal thin region according to $\omega = \omega(x, y)\delta(z)$, with δ the Dirac delta function (see chapter 3 for more details).

Both (4.10) and (4.11) have been solved by a finite-difference method which is second-order accurate both in space and in time. The time-integration was performed with a variable time step, such that $CFL = 0.5$, and the computational domain was represented by a 256×256 grid. The numerical scheme is based on that of Orlandi (1990) and has been slightly adapted to account for the damping term in (4.10) and the strain flow contribution (see chapter 3). The external velocity field was imposed by the boundary condition $\psi|_b = exy|_b$, with b representing the boundary of the computational domain.

Furthermore, the advection of passive tracers was calculated to make a comparison with the dye distributions as observed in the laboratory. Initially, these tracers were distributed uniformly along a circular contour. Owing to the general deformation (stretching and folding) of the material contour during the flow evolution, the tracers had to be redistributed in order to maintain an accurate representation of the passive contour. For that reason, after each time step the contour was represented by a cubic spline on which the tracers were redistributed uniformly with the same initial spatial interval. Unfortunately, thin filaments as shown in figure 4.1(c,d) could not be resolved by the computational grid. Therefore, only a comparison was made with the dye visualizations shown in figure 4.2.

As an initial condition, an axisymmetric vorticity profile was taken according to the Gaussian vortex model:

$$\frac{\omega}{\omega_m} = \left[1 - \frac{1}{2} \left(\frac{r}{r_m} \right)^2 \right] \exp \left\{ -\frac{1}{2} \left(\frac{r}{r_m} \right)^2 \right\}, \quad (4.12)$$

where ω_m is the maximum vorticity and r_m represents the radius of peak velocity. Detailed laboratory observations presented in chapter 2 have demonstrated that this model can be accurately applied to vortices which are generated either by the spinning sphere or by the tangential-injection method (see section 4.2).

In order to determine the initial parameters of the Gaussian vortex, the mid-plane velocity field was measured at $t = 103$ s, shortly after the cylinder had been removed from the tank (see figure 4.2(a)). Then, the values of ω_m and r_m could be obtained from the cross-sectional distributions of vorticity and azimuthal velocity, respectively, which were taken through the centre of the vortex. The radius of the nearly circular dye pattern was measured by hand from the photograph depicted in figure 4.2(a), and was used as an initial condition for the circular material line in the numerical model. This radius was found to be equal to 6.7 cm, which is somewhat larger than the inner radius of the cylinder (4.9 cm). The larger value may be due to the collapse of the injected fluid after the lifting of the cylinder. The rate of strain ϵ was obtained from the horizontal velocity field just before the cylinder was placed in the mid-plane of the tank (see chapter 3 for more details).

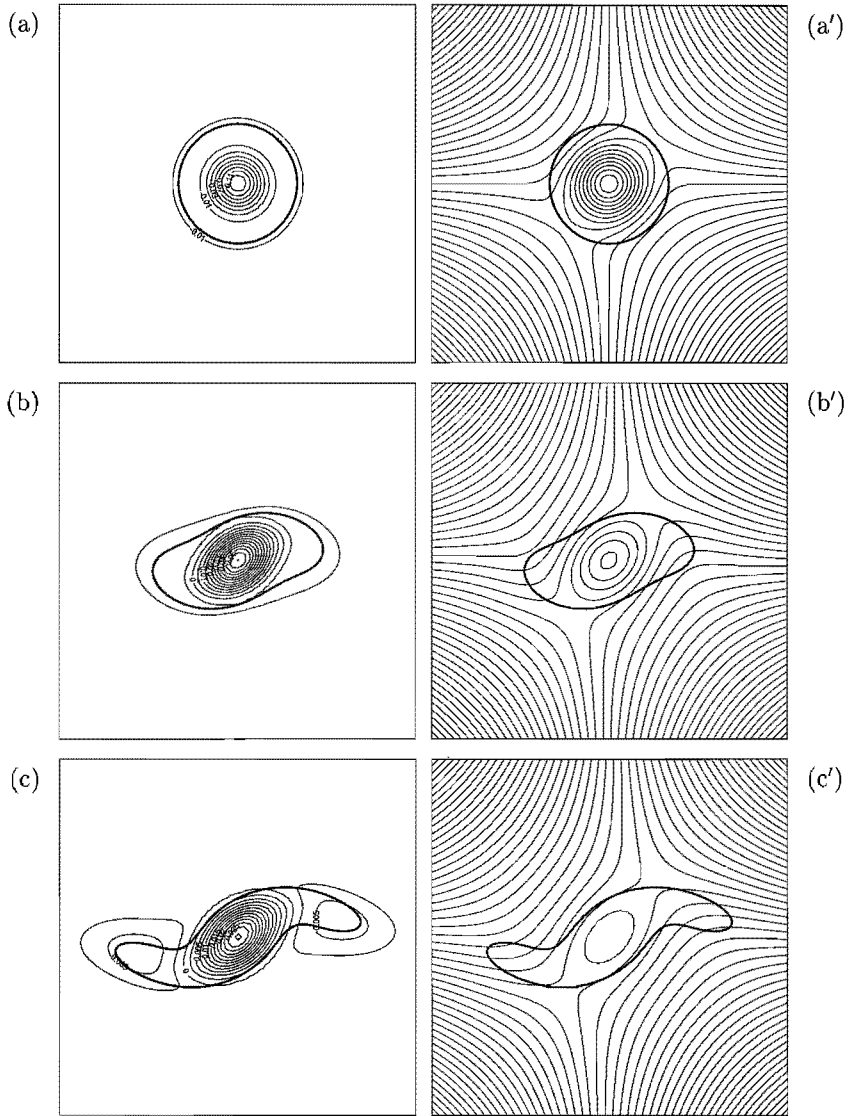


FIGURE 4.11: Contour plots of vorticity (left column) and stream function (right column) as obtained numerically by the finite-difference method. The heavy marked contour represents a contour of passive tracers. The simulation was started at $t = 103$ s. As an initial condition, the vortex was represented by a Gaussian vortex with $\omega_m = 0.15 \text{ s}^{-1}$ and $r_m = 2.7$ cm. A circular contour of passive tracers was taken with a radius of 6.7 cm. Other numerical parameters are: $e = 0.3 \times 10^{-2} \text{ s}^{-1}$, $\nu = 1.065 \times 10^{-2} \text{ cm}^2 \text{ s}^{-1}$ and $CFL = 0.5$. (a,a') $t = 103$ s, (b,b') 273 s, (c,c') 393 s, (d,d') 513 s, (e,e') 633 s, (f,f') 753 s, (g,g') 873 s and (h,h') 1413 s. The passive contours may be compared with the observed dye distributions in figure 4.2.

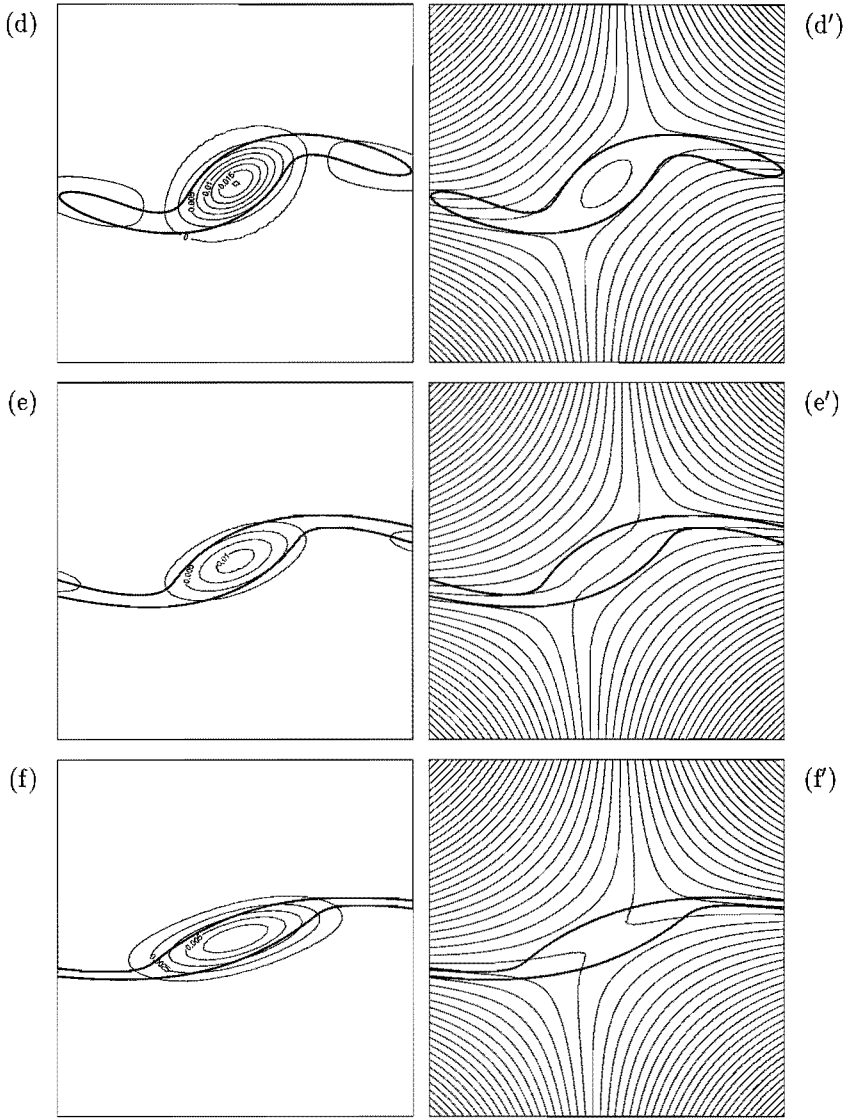


FIGURE 4.11: Continued.

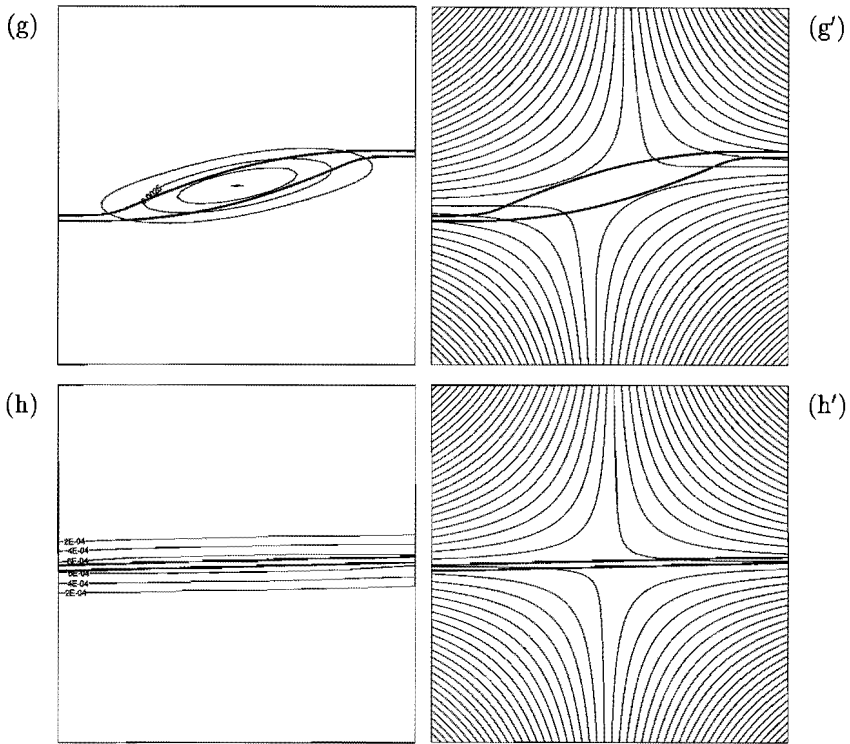


FIGURE 4.11: Continued.

The results obtained by the numerical simulation are given in figure 4.11 by the sequence of vorticity and stream function contour plots. The passive tracer distributions are indicated by the heavy solid lines. It can be seen that until about $t = 513$ s (see (a)–(d)), low-amplitude (negative) vorticity is being removed from the edge of the vortex while the vortex core retains an approximately fixed orientation. The corresponding stream function contour plots (see (a')–(d')) are in good qualitative agreement with the streamline pattern associated with the point-vortex model (see figure 4.5). In the final stage of the evolution, the rotation and elongational deformation of the vortex core are obvious (see figure 4.11(e)–(h)). Simultaneously, the stagnation points vanish, the atmosphere breaks, and a pure strain flow pattern returns, which can be inferred from the streamline patterns in figure 4.11(e')–(h'). In contrast, the velocity field induced by a point vortex submitted to strain flow will always contain two stagnation points.

Next, the evolution of the material contour will be examined. Initially, at $t = 103$ s, the contour of passive tracers encloses most of part the atmosphere, as can be inferred from figure 4.11(a'). In the next stage, see figure 4.11(b')–(d'), similar passive scalar distributions

are obtained as calculated by the contour kinematics approach (see figure 4.9(b)–(d)) and observed in the laboratory (see figure 4.2(b)–(d)). The similarity is obvious, given the broad arms of passive scalars that are being expelled into the ambient fluid, and the orientation of the central part of the tracer distribution. In the final stage of the evolution, the finite-difference calculation shows that the region enclosed by the passive tracers rotates towards the horizontal strain axis while continuously being elongated (see figure 4.11(e′)–(h′)). The latter results are in excellent agreement with the dye visualizations displayed in figure 4.2(e)–(h). Although the vorticity of individual fluid particles is not conserved due to horizontal diffusion, the dyed fluid being shed is clearly associated with negative vorticity, as can be confirmed by comparing the isolines of vorticity with the contours of passive tracers in figure 4.11(a)–(h).

The final breaking of the atmosphere may also explain why the traced particle in figure 4.4(a) is expelled along the horizontal strain axis. In figure 4.4(b), the vortex is apparently still in quasi-equilibrium with the strain flow when tracer *A* leaves the atmosphere. After that, however, the vortex breaks, the point-vortex model is not valid anymore, and tracer *B* is then advected close to the horizontal strain axis.

4.6 Discussion and conclusions

In this chapter, the kinematic properties of monopolar vortices submitted to a straining velocity field have been investigated. Dye-visualization experiments in a stratified fluid have revealed the removal of passive tracers from the edge of the vortex. This phenomenon was also nicely illustrated by the long-term particle trajectories, which were obtained by tracking passive tracers that were distributed in the mid-plane of the stratified fluid.

It was shown that for the main part of the flow evolution, the point-vortex model gives a good qualitative description of the observed advection properties. However, in order to describe the final stage of the passive tracer evolution and to make a quantitative comparison with the laboratory observations, the continuous spatial vorticity distribution of the laboratory vortex must be taken into account. This was confirmed by a full numerical simulation of the quasi-2D vorticity equation.

The qualitative agreement between the point-vortex model and the laboratory observations is quite surprising, since real vortices are characterized by a continuous vorticity distribution, whereas the flow represented by the point vortex is irrotational everywhere except at the origin where vorticity is infinite. The agreement is even more striking because, in contrast to the point vortex, the laboratory vortex has zero net circulation. This paradox may be clarified by noting that the laboratory vortex is characterized by a compact core of positive vorticity and a wide ring of oppositely-signed vorticity which extends to infinity. Therefore, close to the vortex centre, the advection properties will be dominated by the circulation contained in the vortex core.

Point vortices have also been used in related studies to model laboratory-vortex flows. In a study on interacting 2D monopolar and dipolar vortex structures by Meleshko & van Heijst (1994b), the monopolar vortex was represented by a single point vortex, whereas the

dipolar vortex was modelled by a vortex pair, i.e. two point vortices of equal but opposite strength which are separated at some distance. Furthermore, point vortices also proved very useful in describing the motion of tripolar and triangular vortices (see van Heijst & Kloosterziel (1989), Kloosterziel (1990) and Flór & van Heijst (1996)).

Chapter 5

Monopolar vortices in an irrotational annular shear flow

5.1 Introduction

Two-dimensional vortices may be distorted due to mutual interaction. Owing to their generally compact shape, vorticity is mainly concentrated in the core of each vortex. If these vortices come close to each other, they will inevitably merge (see e.g. Overman & Zabusky (1982) and Melander, Zabusky & McWilliams (1988)). However, as long as they are relatively far apart, they may feel a shearing background flow that is essentially irrotational.

Recently, the behaviour of two-dimensional vortices in shear flows has been investigated intensively, especially in numerical studies. Contour dynamics simulations by Dritschel (1989) and Legras & Dritschel (1993, 1994) have revealed the so-called ‘stripping’ of distributed vortices in uniform shear flows, i.e. the removal of weak vorticity from the edge of the vortex, leading to the appearance of thin vorticity filaments which are carried away by the ambient flow. However, not much attention has been paid so far to the behaviour of a monopolar vortex in an irrotational shear flow.

Therefore, in the present chapter, the evolution of a monopolar vortex in an irrotational annular shear flow will be investigated, both experimentally and theoretically. The laboratory experiments were performed in a rotating tank. The ambient flow was generated by an appropriate source-sink configuration, whereas the monopolar vortex was created by locally withdrawing fluid for a short time. Apart from flow-visualization studies, which were necessary to observe the qualitative behaviour of the flow field, quantitative information was obtained by video recordings of small tracer particles. Image analysis techniques were used to measure vorticity distributions and to follow individual particles.

It will be shown that the vortex evolution is characterized by the asymmetric shedding of thin filaments. Theoretically, this behaviour can be explained by applying a contour kinematics method, in which the monopolar vortex is modelled by a single point-vortex surrounded by a contour of passive tracers. Since the point-vortex contains only vorticity

in one singular point, whereas real vortices have essentially distributed vorticity, the effect of the distributed vorticity was investigated by adopting the contour dynamics approach.

This chapter is organized as follows. In section 5.2, a theoretical description will be given of the irrotational shear flow induced by the source-sink arrangement, followed by a description of the laboratory set-up in section 5.3. After that, the laboratory observations will be presented in section 5.4, in which the characteristics of both the shear flow and the monopolar vortex will be investigated separately. In this section, also the evolution of the monopolar vortex in the annular shear flow will be discussed. In section 5.5, the observed vortex stripping will be explained kinematically by the contour kinematics model. In addition, the effect of distributed vorticity will be discussed in section 5.6, where the results obtained by the contour kinematics model will be compared with those obtained by contour dynamics calculations. Finally, in section 5.7, the main results will be discussed and the conclusions will be given.

5.2 Theoretical description of the source-sink flow

Consider the following source-sink configuration in a system that rotates at an angular velocity Ω about the vertical axis of symmetry (figure 5.1). Fluid is injected axisymmetrically at a flow rate Q through a ring-shaped line source in the bottom corner, whereas the same amount of fluid is withdrawn through a sink which is positioned in the centre of the tank.

In view of the axisymmetric shape of the flow domain, it is useful to refer to a cylindrical coordinate system (r, θ, z) , with the corresponding velocity components (u, v, w) . The rotation vector Ω is taken along the z -axis. For convenience, the lengths and velocities will be nondimensionalized by a typical length scale L and some characteristic velocity U , respectively, whereas the dimensionless volumetric flow rate Q^* is defined by:

$$Q^* = QUL^2E^{1/2}. \quad (5.1)$$

Relative to a co-rotating reference frame, with constant angular velocity Ω , the stationary flow is governed by the equations of momentum and conservation of mass, which are given in dimensionless form by:

$$Ro(\bar{v}^* \cdot \nabla^*)\bar{v}^* + 2\bar{k}^* \times \bar{v}^* = -\nabla^* p^* + E(\nabla^*)^2\bar{v}^* \quad (5.2)$$

$$\nabla^* \cdot \bar{v}^* = 0, \quad (5.3)$$

with \bar{v}^* the velocity vector in the rotating frame, p^* the reduced pressure and $\bar{k}^* = \bar{\Omega}/\Omega$ a unit vector in axial direction. The dimensionless parameters Ro and E in (5.2) are the Rossby number and the Ekman number, defined as

$$Ro = \frac{U}{\Omega L} \quad (5.4)$$

$$E = \frac{\nu}{\Omega L^2}, \quad (5.5)$$

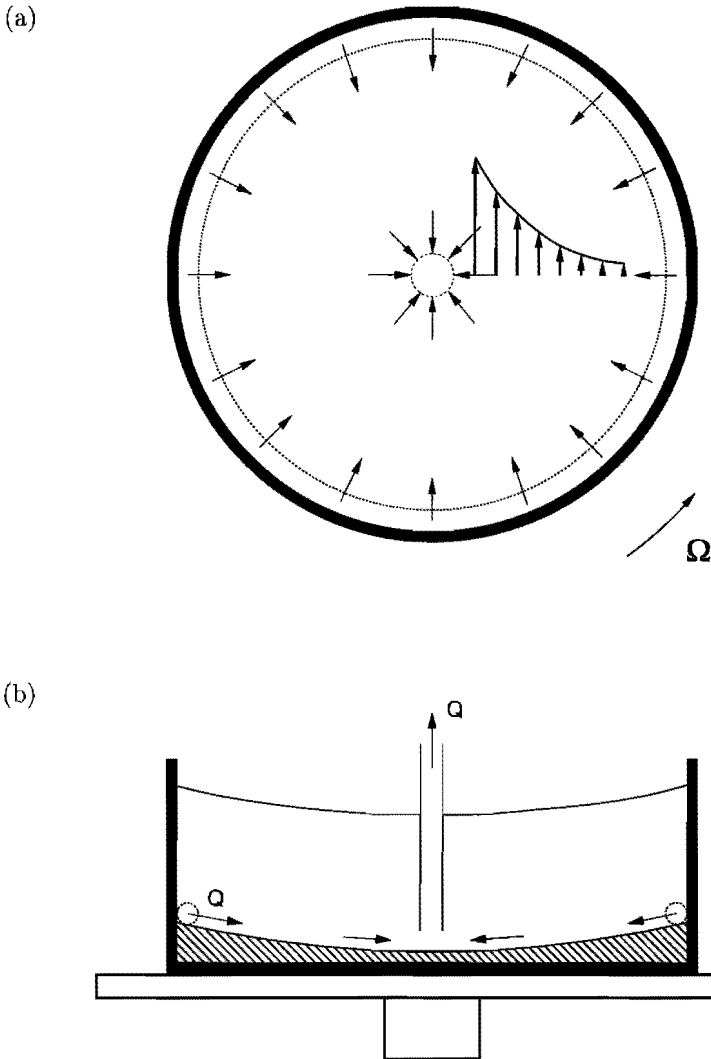


FIGURE 5.1: Schematic drawing of the experimental set-up for the generation of the annular shear flow: (a) top view and (b) side view. The container is placed on a turntable, which rotates with an angular velocity Ω . Fluid is injected axisymmetrically with a constant flow rate Q through a ring-shaped line source in the bottom corner, whereas the same amount of fluid is withdrawn by a source in the centre of the tank. The thin arrows indicate the direction of the $O(E^{1/2})$ transport, whereas the heavy arrows denote the $O(1)$ interior velocity field. The parabolic bottom is indicated by the hatched area.

respectively.

It is assumed that the fluid motion is slow compared to the angular velocity of the system, so that the non-linear terms in (5.2) can be neglected, i.e. $Ro \ll 1$. Moreover, viscous effects are assumed to be small ($E \ll 1$), which implies that the system is rapidly rotating.

In this system, three different regions may be distinguished. At some distance from the solid walls, the fluid is not affected by viscosity, and is governed by a geostrophic balance of forces:

$$2\vec{k}^* \times \vec{v}_I^* = -\nabla p_I^*, \quad (5.6)$$

where the index I refers to the ‘interior’ domain. In order to satisfy the no-slip boundary conditions, an Ekman layer of thickness $\delta_E^* = E^{1/2}$ arises at the bottom wall, whereas a Stewartson layer of thickness $\delta_S^* = E^{1/4}$ is present at the sidewall (see Stewartson (1957)). It will be assumed that the air-drag is identically zero, so that no boundary layer is present at the free surface.

From the azimuthal component of (5.6), with $\partial/\partial\theta = 0$ it follows that $u_I^* = 0$. Moreover, the normal velocity at the free surface requires that $w_I^* = 0$. Therefore, the interior flow is characterized by a purely azimuthal motion. This implies that the radial $O(E^{1/2})$ transport from the source to the sink has to be carried completely by the Ekman layer at the bottom wall. From linear Ekman dynamics (see e.g. Greenspan (1968)) it can be derived that in the Ekman layer the local radial $O(E^{1/2})$ flux per unit length of circumference is given by

$$\tilde{Q}_E^* = \frac{1}{2}v_I^*. \quad (5.7)$$

Consequently, the azimuthal interior velocity field is given by

$$v_I^* = \frac{Q^*}{\pi r^*}, \quad (5.8)$$

or in dimensional form:

$$v_I = \frac{\gamma_s}{2\pi r}, \quad (5.9)$$

where

$$\gamma_s \equiv 2Q \left(\frac{\Omega}{\nu} \right)^{1/2} \quad (5.10)$$

Obviously, the induced motion in the interior domain is equivalent to a potential vortex of strength γ_s . It is also apparent that the strength γ_s is proportional to the flow rate Q . In the subsequent analysis, the index I will be omitted.

5.3 Experimental arrangement

The experiments were performed in a cylindrical tank that was placed on top of a rotating table (see figure 5.1). The tank was filled with water, with a typical fluid depth of 18

cm, and the angular velocity Ω of the turntable was set to 0.70 rad s^{-1} . Either a flat-bottomed container was used (inner diameter 92 cm and depth 35 cm) or a tank with a parabolic bottom (inner diameter 98 cm and depth 25 cm). The parabolic bottom was applied to mimic the shape of the free-surface. In this way, a uniform fluid depth was established in order to avoid topographic vorticity production (by stretching or squeezing of fluid columns). Since a parabolic bottom is not required for purely azimuthal flows (see Hide (1977)), the shear flow measurements were carried out in the flat-bottomed container.

5.3.1 Shear flow generation

Fluid was injected axisymmetrically at the side wall through a ring-shaped tube (of inner diameter 8 mm), which was positioned in the bottom corner of the tank. The tube was perforated with small holes of diameter 1–1.5 mm, every 2 cm along the circumference. Fluid was withdrawn through a narrow perspex tube of inner diameter 10 mm, which was placed vertically along the rotation axis at the centre of the tank. The open end of the sink tube was positioned typically 10 mm above the tank bottom. A pump was used to circulate the fluid through the container with a constant flow rate Q . The flow rate was varied between 1.0 and 10.5 ml s^{-1} , and the fluctuations in Q were measured to be less than 0.2 ml s^{-1} . A similar generation technique was used in a detailed experimental study by Hide (1968), in which a variety of source-sink configurations were discussed. Source-sink flows have also been investigated, either analytically or experimentally, by e.g. Kuo & Veronis (1971), van Heijst (1984) and Brickman & Ruddick (1990).

5.3.2 Monopole generation

A cyclonic vortex was created by locally withdrawing fluid through a (second) perforated perspex tube, with inner diameter 10 mm and outer diameter 15 mm, which was positioned vertically in the fluid. The tube contained 248 small holes of diameter 2 mm, which were distributed uniformly over a length of 15 cm. The fluid was removed by syphoning with a typical flow rate $q = 40 \text{ ml s}^{-1}$ and a typical forcing period $\delta t = 10 \text{ s}$. Owing to the presence of the Coriolis force, the radial motion induced by the sink was deflected in cyclonic direction. After the forcing was stopped and the tube was removed from the tank, a well-defined swirling motion was established within a few rotation periods.

5.3.3 Flow visualization and measurements

The free surface of the fluid was seeded with small tracer particles in order to obtain quantitative information about the interior velocity field. The motion of the floating particles was monitored continuously by a video camera, which was mounted in the rotating frame at some distance above the tank. After the experiment was finished, the velocity field could be determined at successive times by the particle-tracking package *DigImage*, developed by Dalziel (1992). Next, the measured velocity field was interpolated on a mesh of 30×30 grid points (see Paihua Montes (1978) and Nguyen Duc & Sommeria (1988)), which was

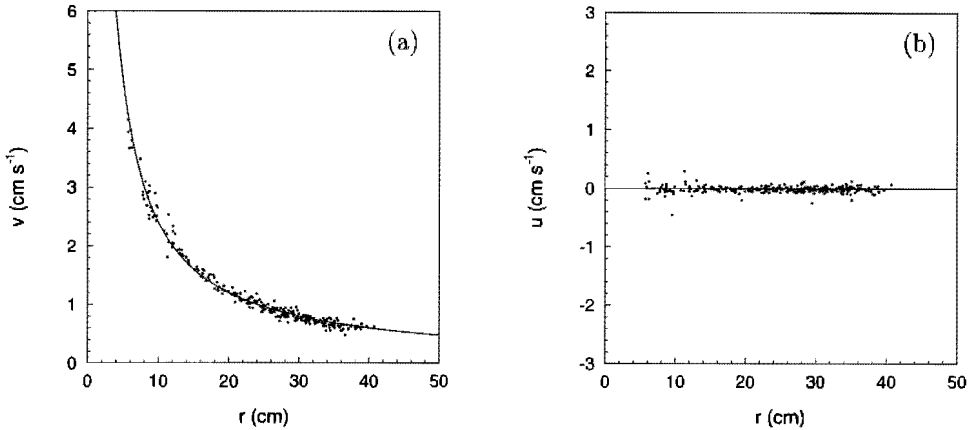


FIGURE 5.2: Radial distributions of the interior velocity components associated with the annular shear flow, 23 min after the forcing was started: (a) azimuthal component v and (b) radial component u . The experimental data are indicated by dots, whereas the least-square fit with (5.9) is represented by the curved solid line. Based on (5.9), the strength of the shear flow was found to be equal to $24.1 \pm 0.1 \text{ cm}^2 \text{ s}^{-1}$. Experimental parameters: $Q = 10.0 \text{ ml s}^{-1}$ and $H = 17.5 \text{ cm}$.

convenient to calculate numerically the distributions of both the vorticity and the stream function. Furthermore, fluorescent dye was added to the fluid to study the qualitative behaviour of the flow field.

5.4 Laboratory observations

5.4.1 Shear flow characteristics

In figure 5.2, the interior velocity components are plotted versus the radial distance r for a typical annular shear flow which was generated by the source-sink arrangement as described in section 5.3. Each data point corresponds to a velocity vector as obtained by the digitized particle streaks. Only velocity vectors corresponding to the interior region were considered, i.e. the flow within the Stewartson layers was neglected. The scatter in the observed data is probably due to the measurement inaccuracy and small disturbances at the free surface, as well as deviations from axisymmetry of the shear flow. The observed distribution of azimuthal velocity, see figure 5.2(a), was least-square fitted with (5.9) (solid line), where $\hat{\gamma}_s$ was taken as a free parameter, and a very good agreement was obtained. (Here, the hat-symbol is added in order to distinguish between the instantaneous shear flow strength $\hat{\gamma}_s$ and the stationary value γ_s). Furthermore, it can be inferred from figure 5.2(b) that the radial velocity is of the same order as the scatter in the experimental data, which is in agreement with the theoretical relation $u = 0$.

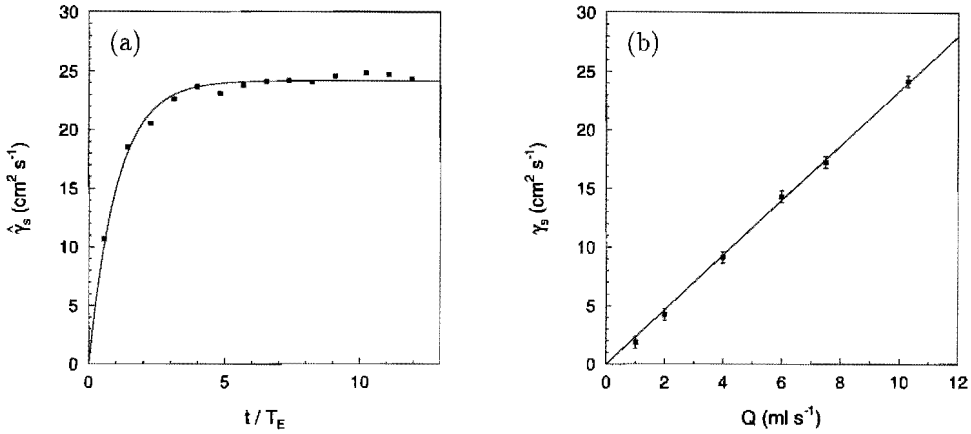


FIGURE 5.3: (a) Time-evolution of the instantaneous shear flow strength $\hat{\gamma}_s$ with $T_E = 211$ s. The measured data (squares) are least-square fitted with (5.11). (b) Relationship between the strength γ_s of the stationary shear flow and the volumetric flux rate Q . The measured data (indicated by the squares) are least-square fitted with the relation $\gamma_s = \alpha Q$. Experimental parameters: $Q = 10.0 \text{ ml s}^{-1}$ (frame (a)) and $H = 17.5 \text{ cm}$.

The spin-up behaviour of the shear flow was investigated by calculating the strength $\hat{\gamma}_s$ at successive times with a least-square fit as shown in figure 5.2(a). Based on these individual fits, the experimental error in $\hat{\gamma}_s$ was estimated to be $0.1 \text{ cm}^2 \text{ s}^{-1}$. The measured time-evolution of $\hat{\gamma}_s$ is plotted in figure 5.3(a) as well as a least-square fit according to

$$\hat{\gamma}_s = \gamma_s \left[1 - \exp\left(-\frac{t}{\tau_s}\right) \right], \quad (5.11)$$

where the free parameters γ_s and τ_s represent the stationary strength and the characteristic time scale, respectively. It can be seen that the curve closely matches the experimental data. The corresponding time scale τ_s was found to be equal to 218 ± 10 s. The deviations from (5.11) are probably due to small fluctuations in Q , since the error in $\hat{\gamma}_s$ is by far too small to account for these deviations. According to linear Ekman dynamics (see e.g. Greenspan (1968)), the time-evolution in rotating flow systems is characterized by the e-folding Ekman time

$$T_E = H/\sqrt{\nu\Omega}, \quad (5.12)$$

where H represents the (mean) fluid depth. Taking the experimental values $H = 17.5 \text{ cm}$, $\Omega = 0.70 \text{ rad s}^{-1}$ and $\nu = 0.98 \times 10^{-2} \text{ cm}^2 \text{ s}^{-1}$ (for a temperature of 21°C) yields $T_E = 211$ s, which is very close to the observed time scale τ_s . It can be derived from figure 5.3(a) that the flow has reached a stationary state after typically $t = 6T_E \approx 20$ min.

According to (5.10), the stationary strength γ_s is proportional to the volumetric flux rate Q . This assertion was checked by generating several shear flows with different flux rates Q , while the angular velocity Ω was held constant at 0.70 rad s^{-1} and the temperature was

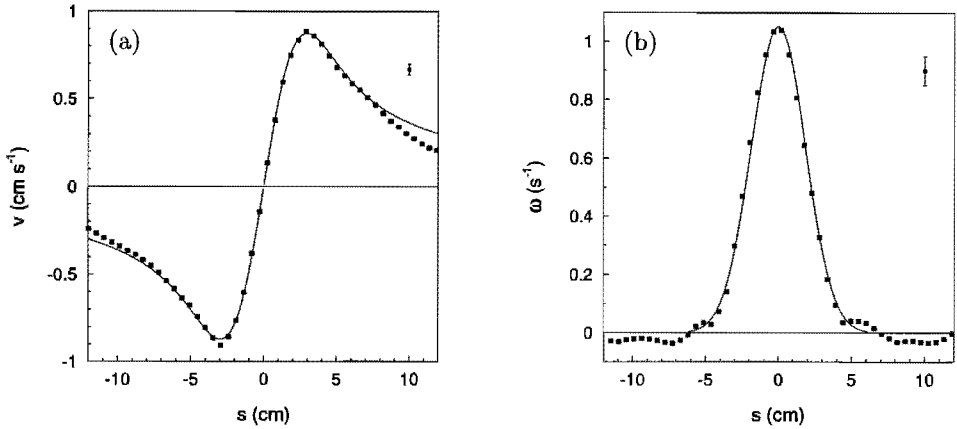


FIGURE 5.4: Radial cross-sectional distributions of (a) the velocity v directed perpendicularly to the cross-section and (b) the vorticity ω of a sink-induced cyclonic vortex, at $t/T_E = 0.27$ with $T_E = 220$ s (the forcing was stopped at $t = 0$). The experimental data (squares) are least-square fitted with (5.15) and (5.14), respectively, which yields $\gamma_v = 22.7 \pm 0.5$ cm² s⁻¹ and $r_m = 2.9 \pm 0.1$ cm. Experimental parameters: $q = 40$ ml s⁻¹, $\delta t = 10$ s and $H = 19.0$ cm.

close to 20°C. The strength γ_s was obtained by taking the average of three instantaneous strengths $\hat{\gamma}_s$ which were determined at $t = 30$ min, 35 min and 40 min, respectively. In figure 5.3(b), γ_s is plotted as a function of Q , and the linear relationship is obvious. A linear least-square fit (solid line) was applied to the observed data with the relation $\gamma_s = \alpha Q$. The experimental value $\alpha = 2.33 \pm 0.02$ cm⁻¹ is close to the corresponding theoretical value $\alpha = 2\sqrt{\Omega/\nu} = 2.66$ cm⁻¹. The systematic deviation may be explained by the shear stress at the free surface. Owing to the rapid rotation of the container, air drag may slow down the motion of the tracer particles at the free surface.

Also an anticyclonic shear flow was generated by simply reversing the direction of flow through the tank, i.e. fluid was injected through a source in the centre of the tank and withdrawn through a sink at the side wall. Apart from the direction of the azimuthal flow, similar results were obtained as in the case of the cyclonic shear flow.

5.4.2 Monopolar vortex characteristics

In figure 5.4, typical measured distributions of vorticity ω and velocity v are plotted along a line through the centre of the monopolar vortex, where s denotes the spatial coordinate and $s = 0$ is defined as the vortex centre. The experimental data are indicated by the markers. The velocity v corresponds to the velocity component directed perpendicularly to the cross-section. It is apparent that the vortex is characterized by a core of single-signed vorticity, which is maximum in the centre, with hardly any negative vorticity around it, i.e. the induced flow has net circulation. This observation can be easily understood from the

generation method. Consider the change in the circulation Γ around a material contour C which encloses the sink tube by which the vortex is generated. For a barotropic and inviscid fluid, the change in the circulation can be written as

$$\frac{D\Gamma}{Dt} = -2 \oint_C (\vec{\Omega} \times \vec{v}) \cdot d\vec{s} = -2\Omega Q, \quad (5.13)$$

with $d\vec{s}$ an infinitesimal segment of the contour C . This equation expresses the production of vorticity by the presence of the Coriolis force. Since the sink initially induces a radially-inward motion, Q will be negative so that $D\Gamma/Dt > 0$, until a quasi-geostrophic motion is established after the forcing is stopped.

The measured velocity profile is observed to be approximately linear in the core of the vortex, whereas at larger radii the velocity decreases relatively slowly towards zero. In figure 5.4, the measured distributions in the vortex core ($|s| \leq 5$ cm) can be accurately fitted by the instantaneous profiles (solid lines) of the so-called Lamb-vortex:

$$\omega = \frac{\gamma_v}{\pi L_v^2} \exp(-s^2/L_v^2) \quad (5.14)$$

and

$$v = \frac{\gamma_v}{2\pi s} \left[1 - \exp(-s^2/L_v^2) \right], \quad (5.15)$$

respectively, where γ_v represents the total circulation of the vortex. In fact, this solution can be considered as a 'snap-shot' of a viscously decaying point vortex at some time t , which was already analysed by Oseen in 1911 (for details, see Lamb (1932)). The characteristic length scale L_v is a measure of the vortex radius and can be related to the radius of peak velocity r_m by the relation $r_m = 1.12L_v$.

The time-evolution of stable barotropic vortices has been accurately described by Kloosterziel & van Heijst (1992). Based on their rotating fluid experiments, it was found that for small Rossby numbers the decay of the vortex velocity field is close to exponential, as expected from linear Ekman dynamics. However, their experiments also showed that under typical laboratory circumstances the initial Rossby number is $O(1)$, so that nonlinear effects are important then: the initial stage of the vortex evolution was characterized by steepening of the velocity profiles and a faster decay rate as compared to linear Ekman decay.

Despite this initial steepening, the results in figure 5.4 show that in the vortex core the velocity and vorticity distributions can be accurately fitted with (5.14) and (5.15). Similar observations were made for later times.

5.4.3 Evolution of the monopolar vortex in the shear flow

The typical evolution of the sink vortex in the annular shear flow is illustrated by the series of video images in figure 5.5. The vortex was created halfway between the centre and the side wall of the tank. Shortly after the vortex forcing was stopped and the tube was removed from the tank, the vortex was visualized with fluorescent dye. It is clear

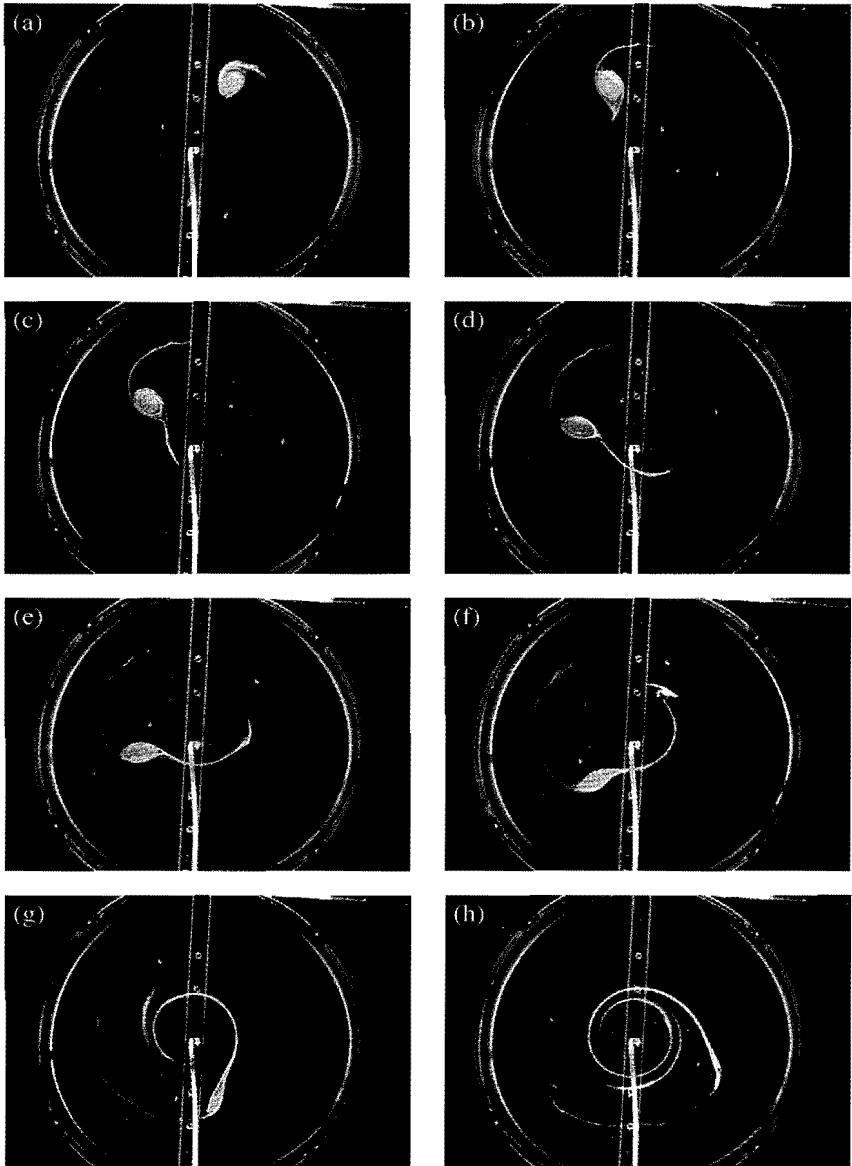


FIGURE 5.5: Dye visualization of a monopolar vortex in an annular shear flow at successive times after the removal of the sink-tube: (a) $t/T_E = 0.13$, (b) 0.24, (c) 0.29, (d) 0.34, (e) 0.39, (f) 0.45, (g) 0.55 and (h) 0.71, where the Ekman time $T_E = 190$ s. The vortex was coloured with dye between $t/T_E = 0$ and 0.10. Experimental parameters: $Q = 10.5$ ml s $^{-1}$, $q = 40$ ml s $^{-1}$, $\delta t = 10$ s and $H = 16$ cm.

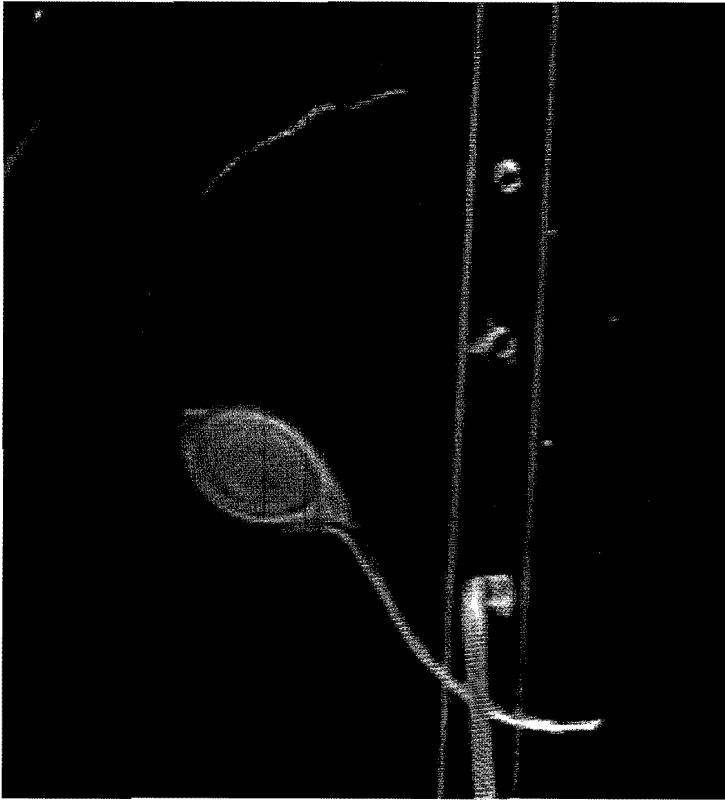


FIGURE 5.6: Enlarged digitized video image showing the asymmetric stripping of the monopolar vortex at $t/T_E = 0.32$, with $T_E = 190$ s. Experimental parameters as in figure 5.5.

from figure 5.5 that the vortex is advected in cyclonic direction, while in the meantime the vortex is being deformed into an oval-like shape. Moreover, the evolution is characterized by the appearance of dye filaments on both sides of the vortex. In the initial stage, see (a), one filament is expelled into the ambient fluid, followed by a second filament which arises on the front side of the vortex (see (b,c)). Close inspection of the flow pattern reveals that the filament at the rear of the vortex extends towards the second filament at the front. This can also be observed in figure 5.6, where a detailed video image is shown of the deformed vortex, along with the two filaments. As time proceeds, a right-angled cusp shows up in the dye pattern associated with the vortex core, see (d), which soon develops into a third filament that is later swept away along the first one (see (e,f)). Note that until this stage, the vortex core is oriented perpendicularly to the flow direction of the annular shear. In the final stage, however, the vortex is completely torn apart while being wrapped around the sink in the centre of the tank, as can be observed in (g,h).

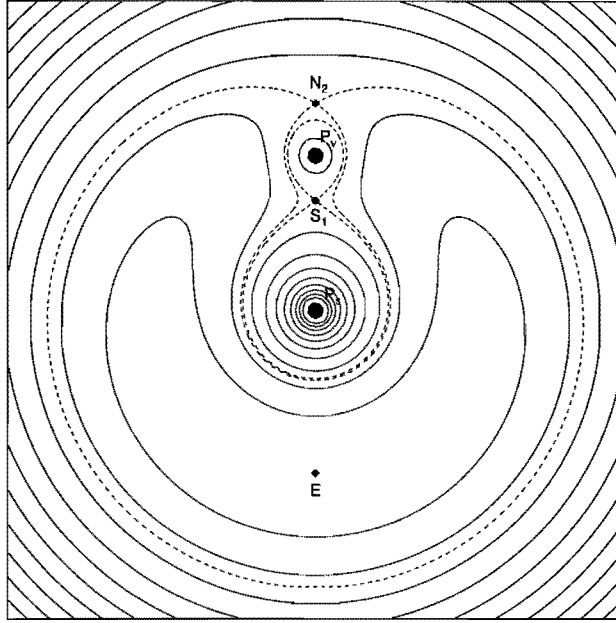


FIGURE 5.7: Characteristic streamline pattern associated with two point vortices (marked P_v and P_s , respectively) in a co-rotating reference frame for the case $\gamma_v/\gamma_s = 0.2$ (see text for more details). The separatrices are indicated by the dashed lines. The hyperbolic points are marked by S_1 and N_2 , respectively, whereas the elliptic point is marked by E .

5.5 Kinematic description of vortex stripping

In order to explain the observed stripping process discussed in section 5.4, the monopolar vortex will be modelled by a point vortex (P_v) with strength γ_v . Moreover, it was shown in section 5.2 that the interior velocity field induced by the source-sink configuration is equivalent to that of a potential vortex, of which the strength γ_s is determined by (5.10). Therefore, the ambient shear flow can also be represented by a point vortex (P_s) which is forced to remain fixed in the origin (see figure 5.7). Point vortex P_v is located at (x_0, y_0) and is passively advected under the action of P_s .

When a co-rotating coordinate system is taken, in which the motion is steady, the Eulerian velocity field is given by

$$u(x, y) = -\frac{\gamma_s y}{x^2 + y^2} - \frac{\gamma_v (y - y_0)}{(x - x_0)^2 + (y - y_0)^2} + \frac{\gamma_s y}{x_0^2 + y_0^2}, \quad (5.16)$$

$$v(x, y) = \frac{\gamma_s x}{x^2 + y^2} + \frac{\gamma_v (x - x_0)}{(x - x_0)^2 + (y - y_0)^2} - \frac{\gamma_s x}{x_0^2 + y_0^2}, \quad (5.17)$$

with u and v the velocity components in the x - and y -direction, respectively. The factors 2π have been included in the definitions of γ_v and γ_s . The first term in each of the above equations corresponds to the shear flow, whereas the second term contains the contribution of the monopolar vortex. The third term arises due to the rotation of the reference system. From (5.16) and (5.17) the stream function can be derived, which may be written as

$$\psi(x, y) = -\frac{\gamma_s}{2} \ln \left[\frac{x^2 + y^2}{x_0^2 + y_0^2} \right] - \frac{\gamma_v}{2} \ln \left[\frac{(x - x_0)^2 + (y - y_0)^2}{x_0^2 + y_0^2} \right] + \frac{\gamma_s x^2 + y^2}{2 x_0^2 + y_0^2}. \quad (5.18)$$

Figure 5.7 shows a contour plot of the co-rotating stream function for the case $\gamma_v/\gamma_s = 0.2$. Two hyperbolic points (or stagnation points) can be identified, viz. at S_1 and N_2 , and one elliptic point, E . Each hyperbolic point is associated with the self-intersection of a streamline: the inner separatrix Ψ_1 , which has an eight-like shape and encloses each point vortex separately, and the outer separatrix Ψ_2 , which surrounds both point vortices.

In order to determine the stream function values $\psi = \Psi_1$ and $\psi = \Psi_2$ at the separatrices, the positions of the hyperbolic points S_1 and N_2 have to be determined. When it is assumed that $x_0 = 0$, the hyperbolic points will lie on the y -axis due to the symmetry of the flow (see figure 5.7). The position of S_1 and N_2 can then be determined by putting both (5.16) and (5.17) equal to zero, which yields

$$u = -\frac{\gamma_s}{y} - \frac{\gamma_v}{(y - y_0)} + \frac{\gamma_s y}{y_0^2} = 0. \quad (5.19)$$

$$v \equiv 0. \quad (5.20)$$

When the singular points $(0, 0)$ and $(0, y_0)$ are excluded and the vortices do not coincide, (5.19) can be written as a cubic equation

$$\left(\frac{y}{y_0} \right)^3 - \left(\frac{y}{y_0} \right)^2 - \left(1 + \frac{\gamma_v}{\gamma_s} \right) \left(\frac{y}{y_0} \right) + 1 = 0, \quad (5.21)$$

which has three real and unequal roots (assuming that $\gamma_v/\gamma_s > 0$):

$$\frac{y_1}{y_0} = 2 \left(\frac{4}{9} + \frac{1}{3} \frac{\gamma_v}{\gamma_s} \right)^{1/2} \cos \left(\frac{\alpha}{3} - \frac{2}{3} \pi \right) + \frac{1}{3}, \quad (5.22)$$

$$\frac{y_2}{y_0} = 2 \left(\frac{4}{9} + \frac{1}{3} \frac{\gamma_v}{\gamma_s} \right)^{1/2} \cos \left(\frac{\alpha}{3} \right) + \frac{1}{3}, \quad (5.23)$$

$$\frac{y_3}{y_0} = 2 \left(\frac{4}{9} + \frac{1}{3} \frac{\gamma_v}{\gamma_s} \right)^{1/2} \cos \left(\frac{\alpha}{3} + \frac{2}{3} \pi \right) + \frac{1}{3}, \quad (5.24)$$

in which

$$\cos \alpha = \frac{9\gamma_v - 16}{6\sqrt{3} \left(\frac{4}{3} + \frac{\gamma_v}{\gamma_s} \right)^{3/2}}. \quad (5.25)$$

The positions $(0, y_1)$ and $(0, y_2)$ correspond to the hyperbolic points S_1 and N_2 , respectively, whereas the position $(0, y_3)$ is related to the elliptic point E . The stream function values Ψ_i ($i = 1, 2$) can be determined by substituting the values y_i ($i = 1, 2$) into (5.18) and by setting $x_0 = 0$:

$$\Psi_i \equiv \psi(0, y_i) = -\gamma_s \ln \left| \frac{y_i}{y_0} \right| - \gamma_v \ln \left| \frac{y_i}{y_0} - 1 \right| + \frac{\gamma_s}{2} \left(\frac{y_i}{y_0} \right)^2, \quad i = 1, 2 \quad (5.26)$$

In order to get an idea of the shape of both separatrices, the stream function (5.18) will be rewritten as

$$\psi = -\gamma_s \ln \left(\frac{r}{r_0} \right) - \gamma_v \ln \left(\frac{R}{r_0} \right) + \frac{\gamma_s}{2} \left(\frac{r}{r_0} \right)^2, \quad (5.27)$$

in which r is the radial distance to point vortex P_s and R is defined as in figure 5.8(a).

Now, for each separatrix, the extrema of R can be found by substituting $\psi = \Psi_i$ into (5.27) and by taking the derivative of (5.27) with respect to θ (defined as in figure 5.8(a)), which yields:

$$\frac{\gamma_v}{R_i} \frac{dR_i}{d\theta} = \frac{\gamma_s}{2} \left[\frac{r_i^2 - r_0^2}{r_i^2 r_0^2} \right] \frac{d(r_i^2)}{d\theta}, \quad (5.28)$$

where R_i ($i = 1, 2$) is the radial distance between P_v and an arbitrary point (x_i, y_i) on the separatrix Ψ_i . Likewise, r_i represents the radial distance between P_s and (x_i, y_i) . By using the trigonometric relation $r_i^2 = R_i^2 + r_0^2 + 2R_i r_0 \sin \theta$ and setting $dR_i/d\theta = 0$, it can be derived that

$$\left[\left(\frac{r_0}{r_i} \right)^2 - 1 \right] \cos \theta = 0. \quad (5.29)$$

In other words, the extrema of R_i should satisfy

$$r_i = r_0 \quad (5.30)$$

or

$$\theta = \frac{\pi}{2} + n\pi, \quad (5.31)$$

respectively, where n is an integer. Combination with (5.27) leads to the following relevant solutions for the extrema of R on the separatrices:

$$\frac{R_i^W}{r_0} = \frac{R_i^E}{r_0} = \exp \left\{ -\frac{\gamma_s}{\gamma_v} \left(\Psi_i - \frac{1}{2} \right) \right\}, \quad (5.32)$$

$$\frac{R_i^N}{r_0} = \exp \left\{ -\frac{\gamma_s}{\gamma_v} \left[\Psi_i + \ln \left(1 + \frac{R_i^N}{r_0} \right) - \frac{1}{2} \left(1 + \frac{R_i^N}{r_0} \right)^2 \right] \right\}, \quad (5.33)$$

where the indices ($i = 1, 2$) and the superscripts refer to the positions as indicated in figure 5.8(a). Relation (5.33) is a transcendental equation which can be solved iteratively by common numerical techniques. Note that R_2^N refers to the same position as y_2 in (5.23).

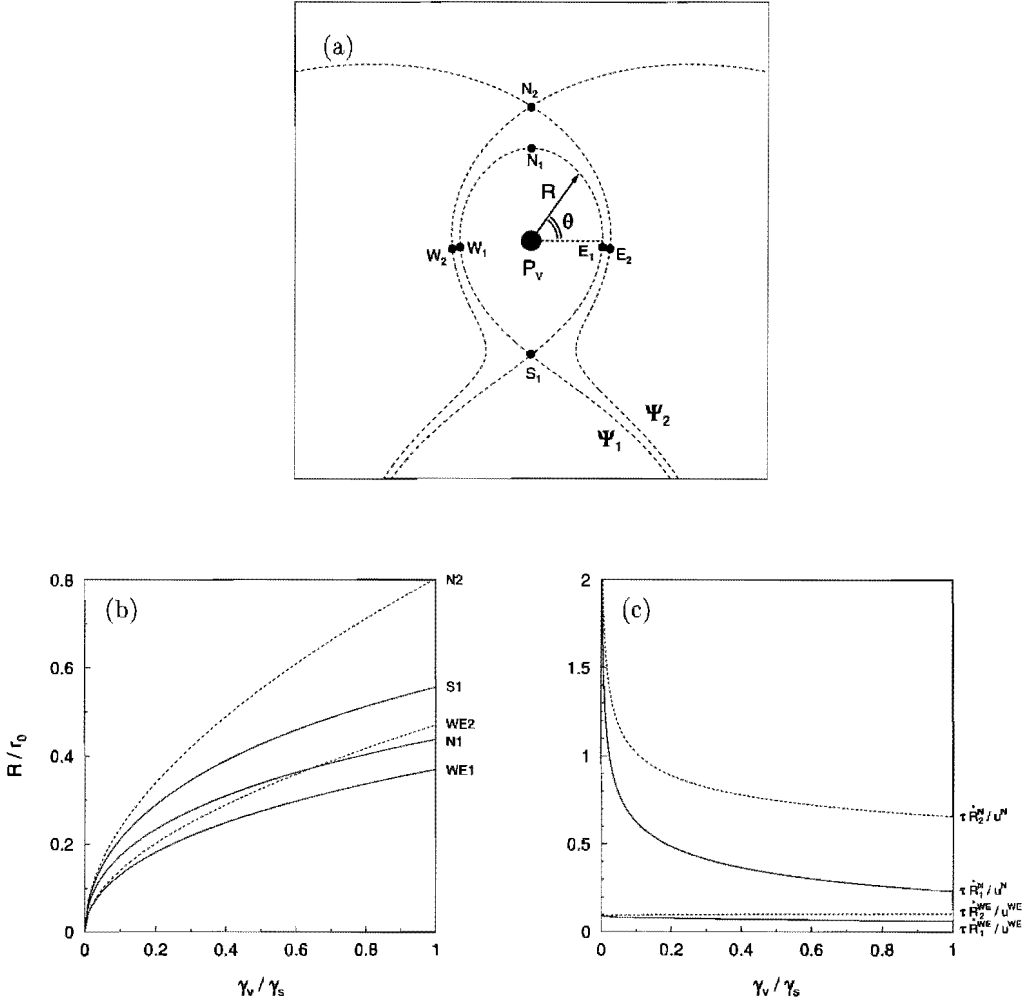


FIGURE 5.8: (a) Location of the extrema on the separatrices, along with the definitions of R and θ . (b) The relative radial distance R/r_0 of the extrema versus γ_v/γ_s . (c) Characteristic parameters at the extremal points as a function of γ_v/γ_s (see text).

In figure 5.8(b), the radial positions of the extrema are plotted as a function of γ_v/γ_s . The solid lines correspond to the inner separatrix (Ψ_1), whereas the dashed lines are related to the outer separatrix (Ψ_2). It is obvious that on the interval $0 \leq \gamma_v/\gamma_s < 0.65$

$$R_1^{WE} < R_2^{WE} < R_1^N < R_1^S < R_2^N, \quad (5.34)$$

whereas in the range $\gamma_v/\gamma_s > 0.65$

$$R_1^{WE} < R_1^N < R_2^{WE} < R_1^S < R_2^N. \quad (5.35)$$

Laboratory observations presented in section 5.4 have revealed that the monopolar vortex is characterized by a continuous spatial vorticity distribution and net circulation. Furthermore, it was observed that the vortex was deformed due to the presence of the background shear flow. Since the vorticity of a point vortex is concentrated in a singular point, the point vortex can essentially not be deformed. Therefore, a passive contour is defined around the point vortex in order to model the shape of the laboratory vortex. Initially, a circular contour may be chosen with radius R_v , which is large enough to ensure that for the corresponding distributed vortex $\omega(R_v)/\omega_m \ll 1$. The area enclosed by this passive contour will now be part of the model vortex.

Suppose that R_v is defined such that $\omega(R_v)/\omega_m = \beta$, where β is a constant that is much smaller than one. Then, depending on the values of R_v and γ_v/γ_s , three different initial situations may be considered, as shown in the upper row of figure 5.9, with the dashed lines denoting the separatrices. In situation A, the passive contour lies entirely inside separatrix Ψ_1 , whereas in situation B, part of the model vortex is located between separatrices Ψ_1 and Ψ_2 . In situation C, the vortex partly overlaps both separatrices. These three different situations that arise for different values of R_v and γ_v/γ_s can also be identified in figure 5.8(b). Case A corresponds to the area below the curve $R_1^{WE}(\gamma_v/\gamma_s)$, whereas situation B corresponds to the area enclosed by the curves $R_1^{WE}(\gamma_v/\gamma_s)$ and $R_2^{WE}(\gamma_v/\gamma_s)$. Finally, the remaining area corresponds to situation C.

In order to investigate the behaviour of the vortex for the three different cases described above, the contour kinematics method was applied here, which allows to follow passive tracers (or nodes) that are positioned on a material contour. The displacement of each tracer was calculated by solving (5.16) and (5.17) with a Runge-Kutta method with variable time step and order (see Hairer, Nørset & Wanner (1987)). In order to maintain an accurate representation of the material contour, extra tracers were added during the time-integration. Likewise, tracers were removed whenever possible to speed up the calculations. For a detailed description of this method, see Meleshko & van Heijst (1994b). In the numerical simulations, the dimensionless time $t^* = t/T$ will be used, with $T = 2\pi r_0^2/\gamma_s$ the orbit period of point vortex P_v around the centre of the flow field.

The typical calculated time-evolution of the vortex is shown in the first column of figure 5.9, where situation A is taken as an initial condition. Since in a steady flow the separatrix acts as a barrier for passive fluid particles, the vortex is trapped within the area enclosed by Ψ_1 . Due to the elliptic-like shape of the streamlines, the blob of passive fluid

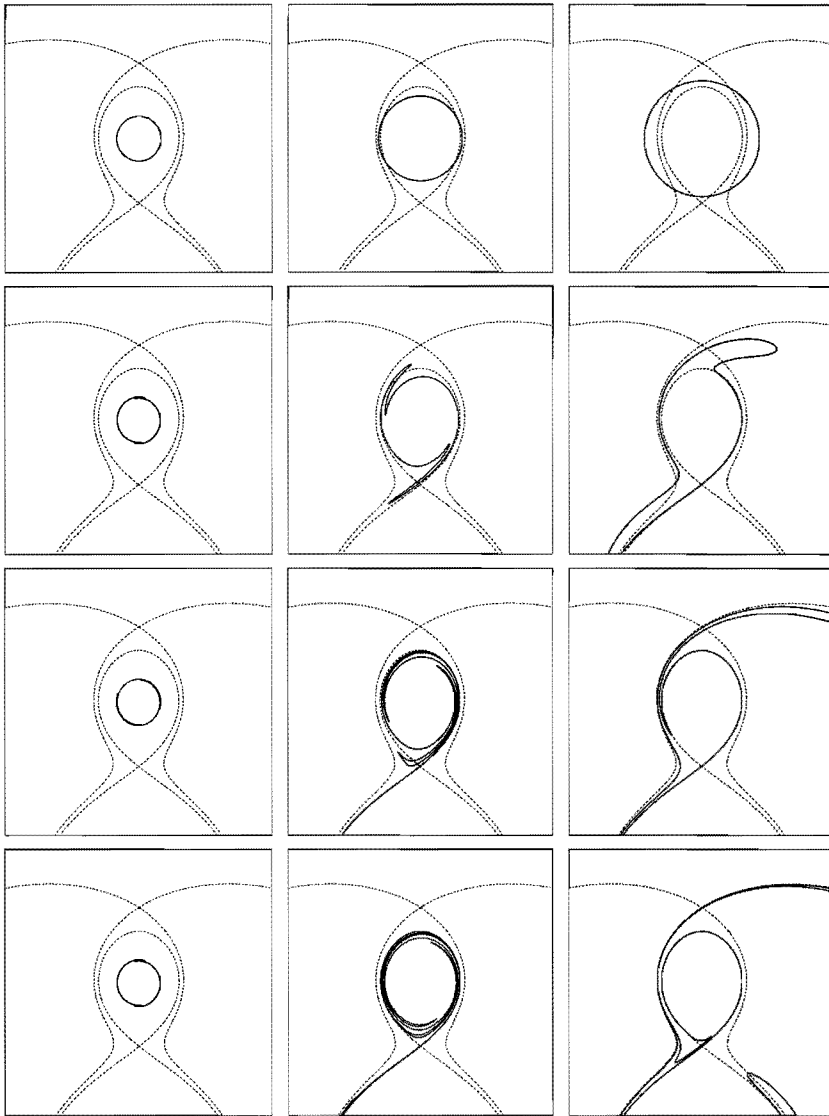


FIGURE 5.9: Calculated time-evolution of passive tracers that are initially located on a circular contour for three different cases: $R_v/r_0 = 0.10$ (left column), $R_v/r_0 = 0.19$ (middle column) and $R_v/r_0 = 0.26$ (right column). For each time-series, $\gamma_v/\gamma_s = 0.2$ and the time interval between successive plots is $1/4$ dimensionless time units.

is slightly deformed and two filaments arise which are being wrapped around the vortex. These filaments, however, never escape from the region bounded by the inner separatrix.

The advection of fluid with situation B as an initial condition is illustrated by the sequence of plots shown in the second column of figure 5.9. While most of the vortex area is still trapped inside the region enclosed by separatrix Ψ_1 , both parts of the vortex which are located outside Ψ_1 are advected towards stagnation point S_1 , giving rise to two tails which are expelled into the ambient flow.

When the vortex partly covers both separatrices (situation C), tracers that are located in between both separatrices will be transported towards stagnation point S_1 (see right column in figure 5.9). This is also true for the tracers lying in the exterior region on the left-hand side of Ψ_2 . However, the edge of the vortex on the right-hand side of separatrix Ψ_2 will be advected towards stagnation point N_2 , and hence form an additional tail.

Thus far, attention has been restricted to steady flows. However, according to linear Ekman dynamics, monopolar vortices in rotating fluids decay exponentially in time, which was confirmed experimentally by Kloosterziel & van Heijst (1992). In order to examine the effect of the exponential decay of vorticity, γ ($\equiv \gamma_v/\gamma_s$) will be made time-dependent according to

$$\gamma(t) = \gamma_0 \exp(-t/\tau), \quad (5.36)$$

where γ_0 represents the initial ratio between γ_v and γ_s (the latter being a constant due to the continuous forcing), and τ is the characteristic decay time.

Figure 5.10 shows the typical calculated evolution of the model vortex in the time-dependent velocity field, with situation C taken as an initial condition. In the initial stage of the evolution, the material contour is deformed in a similar manner as in the stationary case (see right column of figure 5.9). However, due to the decay of γ the area enclosed by separatrix Ψ_1 will shrink, which leads to the continuous feeding of the filament near stagnation point S_1 . Also both separatrices will come closer together, which can be derived from figure 5.8(b), so that the distance between the filaments and the core becomes smaller. Moreover, when time increases, a third filament appears close to stagnation point N_2 , which is entirely absent in the stationary case. Apparently, the expulsion of the third filament is a property of the decaying vortex. The final stage of the evolution is characterized by the continuous depletion of the vortex core, while the area of the vortex core progressively decreases. Note that during the entire stripping process, the vortex core retains its perpendicular orientation to the shear flow direction.

In order to explain the appearance of the third filament, it is convenient to define some average velocities in the narrow 'canal' between both separatrices:

$$u^E = \frac{\Psi_2 - \Psi_1}{R_2^E - R_1^E} \quad (5.37)$$

$$u^N = \frac{\Psi_2 - \Psi_1}{R_2^N - R_1^N} \quad (5.38)$$

$$u^W = \frac{\Psi_2 - \Psi_1}{R_2^W - R_1^W}. \quad (5.39)$$

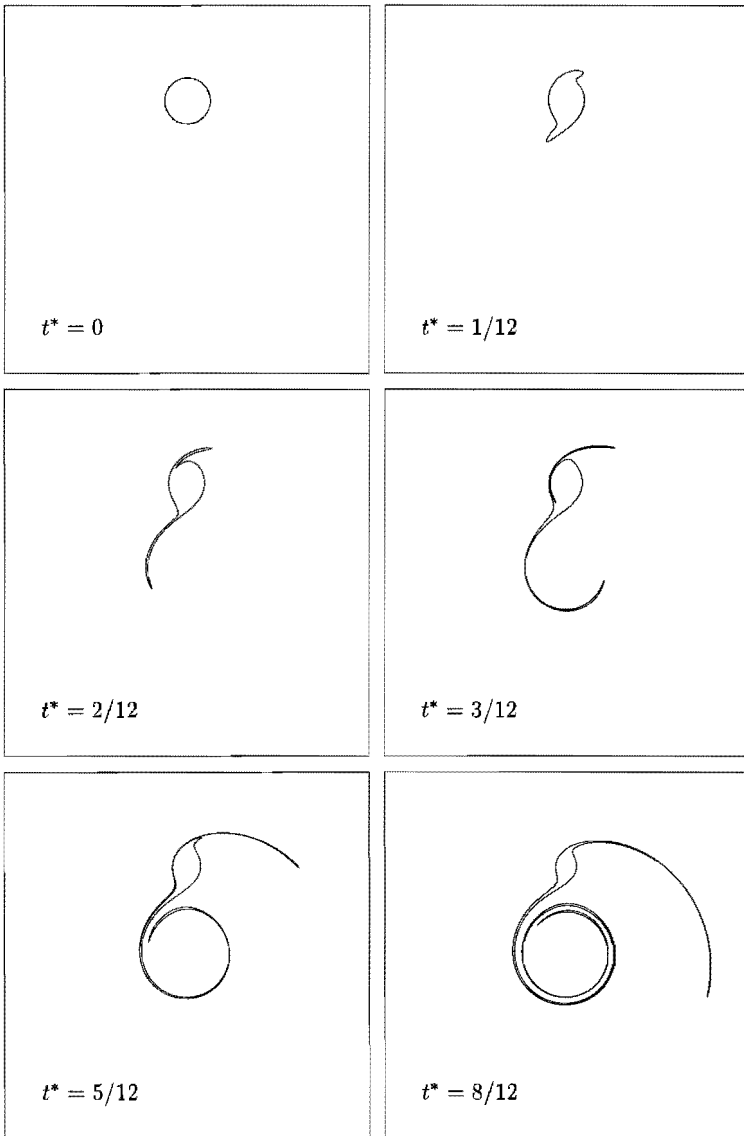


FIGURE 5.10: Temporal evolution of passive tracers for an exponentially decaying point vortex in an annular shear flow. Numerical parameters: $R_v/r_0 = 0.26$, $\gamma_0 = 0.32$ and $\tau^* = 2.72$.

These velocities can easily be calculated numerically by using (5.26), (5.32) and (5.33). Owing to the symmetry of the flow field, $u^E = u^W (\equiv u^{WE})$.

Furthermore, the time derivatives of the extremal radii R_i^{WE} and R_i^N can be written as

$$\dot{R}_i^{WE} = \frac{dR_i^{WE}}{d\gamma} \dot{\gamma} \quad (5.40)$$

$$\dot{R}_i^N = \frac{dR_i^N}{d\gamma} \dot{\gamma}, \quad (5.41)$$

respectively, where the dot represents differentiation with respect to time, and $\dot{\gamma} = -\gamma/\tau$ according to (5.36).

It may now be anticipated that all the fluid that crosses separatrix Ψ_1 will be carried away along stagnation point S_1 as long as $\dot{R}_1^{WE} \ll u^{WE}$ and $\dot{R}_1^N \ll u^N$, i.e. passive fluid is being advected quasi-steadily around separatrix Ψ_1 . However, when one of these conditions is not satisfied, fluid may leak through separatrix Ψ_2 . In order to investigate whether these conditions are fulfilled during the decay process, the ratios $\tau \dot{R}_i^{WE}/u^{WE}$ and $\tau \dot{R}_i^N/u^N$ have been plotted versus γ in figure 5.8(c) for $i = 1, 2$.

Owing to the decay of γ , fluid will continuously leak through separatrix Ψ_1 . Supposing that $\tau \approx O(1)$ (which is the case for the numerical results shown in figure 5.10), it is clear from figure 5.8(c) that fluid crossing the inner separatrix near one of the extremal points W_1 or E_1 is advected adiabatically towards the stagnation point S_1 for all values of γ . Also near extremum N_1 the fluid is removed in a quasi-steady way, except for small values of γ . The latter restriction explains the occurrence of the third filament in the contour kinematics simulation: owing to the smallness of velocity u^N compared to both \dot{R}_1^N and \dot{R}_2^N , stagnation point N_2 penetrates into the core of the model vortex, which consequently leads to the expulsion of the third filament. Although $\dot{R}_2^N/u^N \approx O(1)$ for the entire range of γ , stagnation point N_2 can never reach the boundary of the vortex as long as the fluid near separatrix Ψ_1 is advected quasi-adiabatically, i.e. $\dot{R}_1^N/u^N \ll 1$.

Additional numerical simulations were carried out with situation A or B as an initial condition; apart from the absence of the first filament near stagnation point N_2 , similar results are obtained as those shown in figure 5.10.

The experimental observations shown in figure 5.5 are in very good qualitative agreement with the numerical results presented in figure 5.10 throughout the major part of the vortex evolution. This is evident from the filaments that appear on both sides of the vortex, and the shape and orientation of the vortex core. This similarity is quite striking, keeping in mind that real vortices are characterized by a continuous spatial vorticity distribution, whereas this is not the case for a point vortex. Similar long vorticity filaments have been observed in numerical studies on the interaction of two monopolar vortices of like-signed vorticity (see e.g. Melander, Zabusky & McWilliams (1987) and Dritschel & Waugh (1992)). Even so, the final breaking of the laboratory vortex cannot be explained by the simple point-vortex model. Therefore, in the next section, the effect of the continuous vorticity distribution will be examined.

5.6 The influence of distributed vorticity

The effect of the vorticity distribution on the evolution of the monopolar vortex in the annular shear flow was investigated by applying the contour dynamics approach. The contour dynamics method is based on the Euler equations in two dimensions and requires a discretization of the spatial vorticity distribution, i.e. the spatial vorticity profile is represented by concentric contours between which the vorticity is uniform (see Zabusky, Hughes & Roberts (1979)). The contours are modelled by nodes and can be followed in time by performing a time-integration of the total velocity field which consists of two contributions: the velocity field associated with the discretized vortex, which can be found by solving Poisson's equation, and the background velocity field, which may be calculated analytically. Like in the contour kinematics approach, nodes are being added and removed in the course of the calculation, depending on the local deformation of the contours.

As an initial condition, the vorticity profile (5.14) was taken, which was represented by 7 equidistant vorticity contours. The uniform vorticity ω_i at each vorticity level i was chosen such that $\omega_i = \Gamma_i/A_i$, where A_i represents the area enclosed by the bounding contours i and $i - 1$, and Γ_i is the corresponding circulation associated with the distributed vortex (it should be noted that $i = 0$ corresponds to the centre of the vortex). The radius of the third contour was taken equal to L_v (the characteristic length scale of the vortex), whereas the radius of the exterior contour R_v was chosen equal to $2.6L_v$. The flow surrounding the exterior contour was assumed irrotational. As a result, the total circulation of the discretized vortex is 0.9988γ , which is almost equal to the strength γ of the distributed vortex. The linear Ekman decay was mimicked by allowing each level of uniform vorticity to decay according to $\omega_i(t) = \omega_i(0) \exp(-t/\tau)$, where $\omega_i(0)$ represents the initial vorticity value.

The typical evolution of the vorticity contours is shown in figure 5.11, where the same initial parameters γ_0 and τ^* have been used as in the contour kinematics calculations. These parameters are based on quantitative measurements of the sink-vortex characteristics in a still ambient fluid just after the forcing device was removed from the tank. Since the radius of the exterior vorticity contour is equal to that of the material contour shown in figure 5.10, both contours may be compared with each other, and one can observe a remarkable resemblance during most part of the evolution. Apparently, the filaments being detached from the discretized vortex contain a negligible amount of vorticity, because otherwise, the circulation of the remaining vortex would decrease faster than exponential. In the final stage of the evolution, however, the contour dynamics results show that the vortex is torn apart by the shear flow, while the stripping process around the point vortex continues indefinitely. This discrepancy may be understood by noting that in general, vortices with a finite vorticity distribution are overcome by the shear flow at some critical value $(e/\omega_m)_c$; that is, when the local strain rate e (which is equal to γ_s/r_0^2 for the annular shear flow described in this chapter) is sufficiently large compared to the maximum vorticity ω_m of the vortex. When the ratio e/ω_m exceeds this critical breaking value the stagnation points will vanish, resulting in the final elongation of the entire vortex. On the other hand, the point vortex cannot be broken by definition, since it contains infinite vorticity in a

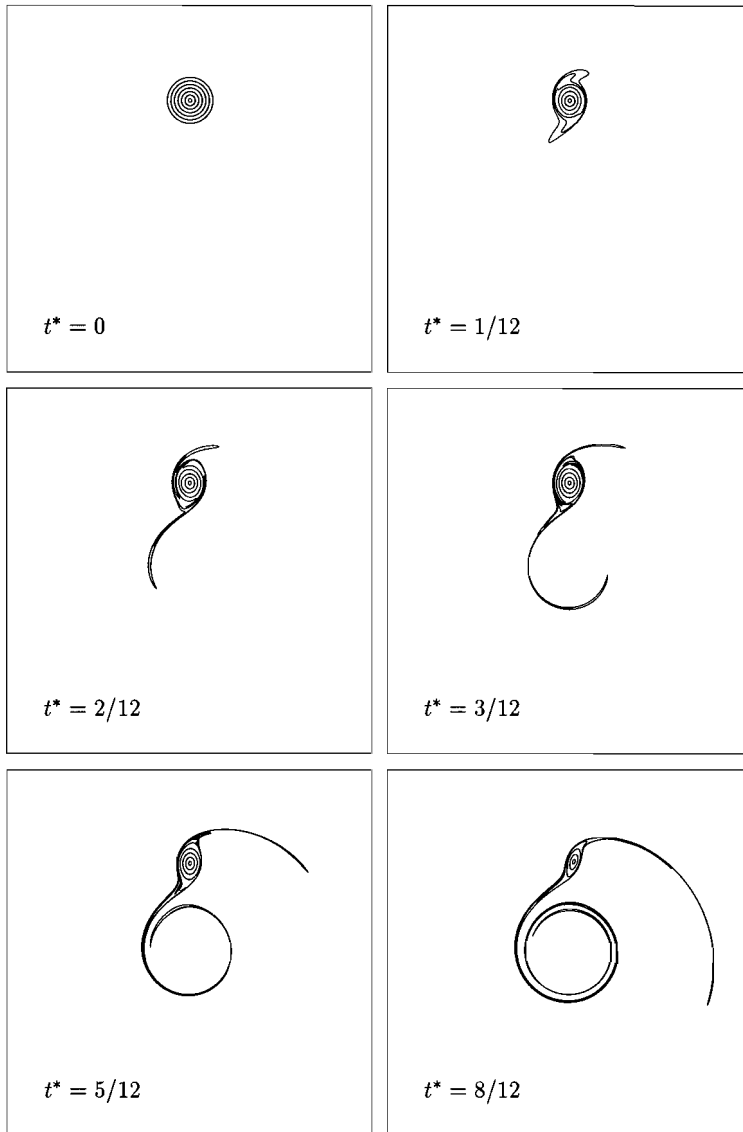


FIGURE 5.11: Time series of the evolving vorticity contours in an annular shear flow as obtained by the contour dynamics method (see text for more details). Numerical parameters: $R_v/r_0 = 0.26$ ($L_v/r_0 = 0.10$), $\gamma_0 = 0.32$ and $\tau^* = 2.72$.

singular point. Consequently, the stripping process persists forever.

The contour dynamics results are also in very good qualitative agreement with the laboratory observations depicted in figure 5.5 during the entire evolution of the vortex. It is observed that both experimentally and numerically, the vortex remains oriented perpendicularly to the shear flow direction for a considerable time. In an analytical study by Kida (1981), it was shown that this orientation corresponds to the steady state of an elliptic patch of uniform vorticity embedded in a linear shear flow. Moreover, contour dynamics simulations by Legras & Dritschel (1993, 1994) have revealed that in a slowly growing linear shear flow, distributed vortices evolve along quasi-stationary states for a considerable time until the vortex is torn apart by the ambient flow. Although the annular shear as described in the present study is characterized by a nonlinear radial velocity distribution, the vortex core is apparently insensitive to the exact shape of the background velocity profile. The reason for this may be that locally, the velocity profile of an arbitrary shear flow is always close to linear.

The quasi-adiabatic stripping process described above is very similar to that observed in the laboratory for a monopolar vortex submitted to a pure strain flow (see chapter 3), in which case the vortex is oriented at an angle of 45 degrees with respect to the horizontal strain axis. The similarity is not surprising since in both cases the vortex is oriented at 45 degrees with respect to the principal axes of the strain. This may also explain the final orientation of the vortex as shown in figure 5.5 and 5.11, which corresponds to the elongation of the vortex along one of these principle axes.

Although the evolution of the numerically obtained vorticity contours is very similar to the evolving dye pattern as observed in the laboratory, the Ekman time T_E is about twice as large as the e-folding decay time τ corresponding to the numerical results depicted in figures 5.10 and 5.11. Therefore, similar numerical simulations were performed with $\tau = T_E$. Again, the results obtained by the contour kinematics technique were in excellent agreement with the contour dynamics calculations for a considerable time. However, the laboratory observations revealed a much faster evolution compared with these latter numerical results.

Since the initial Rossby number was $O(1)$ in the rotating fluid experiments, it is very likely that the accelerated evolution of the laboratory vortex is due to nonlinear effects, as discussed in section 5.4. Accordingly, the evolution of the vortex is initially much faster than expected from an exponential vorticity decay. Furthermore, the Ekman layer at the bottom wall drives a secondary motion that will result in an additional radial growth of the vortex. Although this effect may be neglected in the linear case, it is important when nonlinear effects come about. Both the faster decay of vorticity and the growing vortex size may enhance the advection of vorticity across the inner separatrix, which leads to an accelerated erosive decay of the vortex.

Another reason for the accelerated evolution of the laboratory vortex might be that the vorticity decay is enhanced by viscous effects. Indeed, it was shown in a numerical study by Mariotti, Legras & Dritschel (1994) that the combination of vortex stripping and diffusion may speed up the stripping process and consequently the decay of the vortex. However, considering the initial ratio of the Ekman decay time and the characteristic diffusive time

$T_E/T_d \approx 0.2$, where $T_d \equiv r_m^2/\nu$, diffusion will only be of secondary importance.

Furthermore, it should be stressed that the initial vortex parameters used in the numerical calculations have been obtained from measurements in a still ambient fluid. It may well be that the generation of the sink-vortex is affected by the shear flow. However, close inspection of the spiralling dye structure revealed that in the initial stage Ro is still $O(1)$. Quantitative measurements of the flow field have confirmed this assertion. Finally, the effect of the sidewall may probably be neglected, since the core of the vortex is being advected with the local velocity associated with the shear flow.

5.7 Conclusions

Rotating fluid experiments described in this chapter have revealed the stripping of a monopolar vortex in an irrotational annular shear flow. In contrast to uniform shear flows, the vorticity filaments were observed to be asymmetrically attached to the vortex core. Theoretically, the asymmetric stripping process can be explained in terms of the streamlines in a co-rotating frame, as obtained by modelling both the monopolar vortex and the irrotational shear flow simply by point vortices. The co-rotating streamline pattern is characterized by two nested separatrices, each of which contains one stagnation point. Combination of the point-vortex model with the contour kinematics technique revealed a very good qualitative agreement with the laboratory observations for the quasi-stationary part of the vortex evolution. Contour dynamics simulations have shown that the final breaking of the vortex is caused by the continuous spatial vorticity distribution of the laboratory vortex. The temporal evolution of the vortex may be accelerated by nonlinearities and lateral diffusion, effects which were not incorporated in the contour dynamics model. However, it is expected that these mechanisms do not affect the basic evolution characteristics of the monopolar vortex in an irrotational annular shear flow.

Chapter 6

Dipolar vortices in a strain flow

6.1 Introduction

In contrast to monopolar vortices, the evolution characteristics of dipolar vortex structures in ambient flows have hardly been addressed. In a numerical study by Kida, Takaoka & Hussain (1991), it was observed that the front-back symmetry of a two-dimensional dipolar vortex is broken when the vortex is submitted to a strain flow that pushes both dipole halves together. As a result, a head-tail structure was formed. However, this behaviour has as yet not been confirmed by experimental observations. For that reason, the strain-induced evolution of dipolar vortices is investigated in the present study. In fact, two different cases are considered in which the vortex centres of the dipole are either compressed or separated by the ambient flow. In the former situation, see figure 6.1(a), the strain flow will be referred to as ‘cooperative’, in view of its progressive effect on the translational motion of the dipole, whereas in the latter case, see figure 6.1(b), the strain flow will be termed ‘adverse’, since it opposes the dipole’s self-induced motion. So far, the evolution of a dipolar vortex in an adverse strain flow has not been considered before, neither in numerical studies nor in experimental work.

The laboratory experiments described in this chapter were carried out in a stratified fluid; the dipolar vortex was generated by a pulsed horizontal injection of a small amount of fluid, whereas the strain flow was continuously forced through four rotating discs (see chapter 3). The horizontal flow characteristics were measured by tracking small passive tracer particles which were floating at a specific level in the stratified fluid. Furthermore, dye-visualization studies were used to obtain qualitative information about the dipole evolution.

The laboratory observations are compared with two numerical models. As a first approach, the contour kinematics method is used, in which the dipolar vortex is modelled by two point vortices of equal strength, but opposite in sign, surrounded by a single contour of passive tracers. This technique has been applied successfully by Meleshko & van Heijst (1994b) to study the stirring properties of interacting monopolar and dipolar vortices. As a second approach, both the spatial distribution of vorticity and the effect of viscous dif-

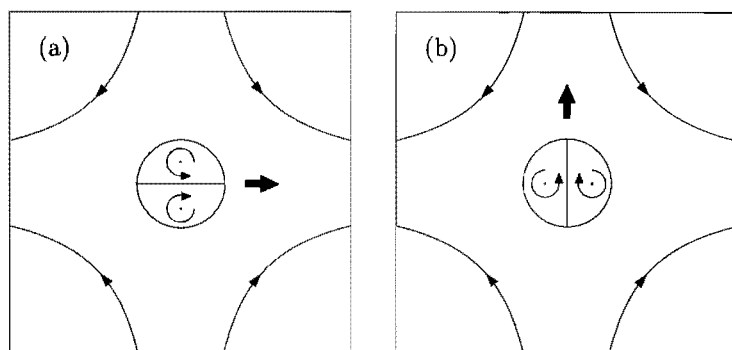


FIGURE 6.1: Schematic drawing of a dipolar vortex in (a) a cooperative and (b) an adverse strain flow.

fusion are taken into account by solving the full quasi-two-dimensional vorticity equation with a finite-difference method.

This chapter is organized as follows. In section 6.2, a description of the experimental set-up is given. After that, the observed evolution of the dipolar vortex in a cooperative strain flow is discussed in section 6.3. Furthermore, a kinematic explanation of the head-tail formation is given, followed by a comparison with the numerical results obtained by the different calculation techniques. Likewise, the behaviour of the dipolar vortex in an adverse strain flow is examined in section 6.4. Finally, the main conclusions are given in section 6.5.

6.2 Experimental arrangement

The experiments were carried out in a perspex tank with horizontal dimensions 100×100 cm and depth 30 cm. The tank was filled with a two-layer salt stratification. The average buoyancy frequency N in the diffused interface (near the mid-plane of the tank) was varied between 3.5 and 4.5 rad s^{-1} .

The strain flow was realized with four rotating horizontal discs (diameter 10 cm, thickness 0.5 cm), which were positioned at the corners of a square in the mid-plane of the tank (see figure 3.1). The diagonal distance between the centres of the discs was 60 cm, and the discs were rotated with a constant rotation speed of typically 3.0 rpm. This generation method is identical to that described in chapter 3. Typically one hour after the forcing was started, a quasi-steady strain flow was formed that was close to uniform near the centre of the tank.

The dipolar vortex was created by a pulsed injection of a small amount of fluid through a thin nozzle (see e.g. van Heijst & Flór (1989)). The injection nozzle was positioned in the same plane as the rotating discs, along one of the strain axes. The density of the injected fluid was chosen equal to that of the ambient fluid at the plane of injection. The injection

rate Q ($= 5.6 \text{ ml s}^{-1}$) and forcing period δt ($= 1.2 \text{ s}$) could be accurately controlled by a computer-driven injection mechanism. The Reynolds number $Re = U_{inj}d/\nu$ was equal to 2400, and was based on the injection speed U_{inj} , the nozzle diameter d ($= 2 \text{ mm}$), and the kinematic viscosity ν of the injected fluid (which was equal to $1.085 \times 10^{-2} \text{ cm}^2 \text{ s}^{-1}$ with the temperature being 19°C). As a result, a three-dimensional turbulent cloud was created by the injected fluid. It was shown by van Heijst & Flór (1989) and Flór & van Heijst (1994) that in the subsequent stage, the turbulent region quickly collapsed under gravity, leading to the gradual formation of a flat dipolar vortex structure.

Qualitative information about the horizontal flow characteristics was obtained by monitoring small polystyrene particles of density 1.04 g cm^{-3} with a video camera, which was mounted at some distance above the tank. The passive particles were distributed around the injection level within a layer of approximately 1 cm thickness. After the entire experiment was recorded on video tape, the video images were digitized and subsequently processed by the image analysis system *DigImage* developed by Dalziel (1992). A particle-tracking technique, which is part of this system, was used to obtain the local velocity vectors at successive times. As a next step, the velocity field was calculated on a rectangular 65×65 grid by a spline-interpolation method (see Paihua Montes (1978) and Nguyen Duc & Sommeria (1988)), from which the values of the vorticity ω and the stream function ψ could be calculated in each grid point. In other cases, the flow was visualized by adding fluorescent dye of matching density to the injection fluid.

6.3 Dipolar vortex in cooperative strain flow

6.3.1 Qualitative observations

The typical evolution of the dipolar vortex in a cooperative strain flow is shown by the sequence of video images presented in figure 6.2. Initially, the motion of the injected fluid is essentially three-dimensional turbulent, as can be observed in (a). Owing to the gravitational collapse and the merging of like-signed eddies (see Flór & van Heijst (1994)), this turbulent region eventually transforms into a dipolar vortex structure (see (b)–(d)). Although special care was taken that the injection nozzle was accurately aligned with one of the strain axes, a slightly asymmetric dipole was formed in this case. Symmetric dipoles were obtained in only very few occasions, which is most likely due to the irregular distribution of vorticity during the dipole formation. The deforming effect of the straining flow can be observed in frames (e)–(h): the dipole is compressed and elongated as a whole, resulting in the formation of two tails at its rear. Because the dipole was slightly asymmetric, the right-hand tail was more developed than the other.

Note that the long dye filaments behind the dipole are just remnants of the formation process of the vortex, and should not be confused with the tails of the dipole. In fact, these filamentary structures have also been observed behind dipolar vortices in a quiescent ambient fluid (see Flór & van Heijst (1994)). Furthermore, it can be seen that shortly after the dipole formation, considerable entrainment of (irrotational) ambient fluid occurs

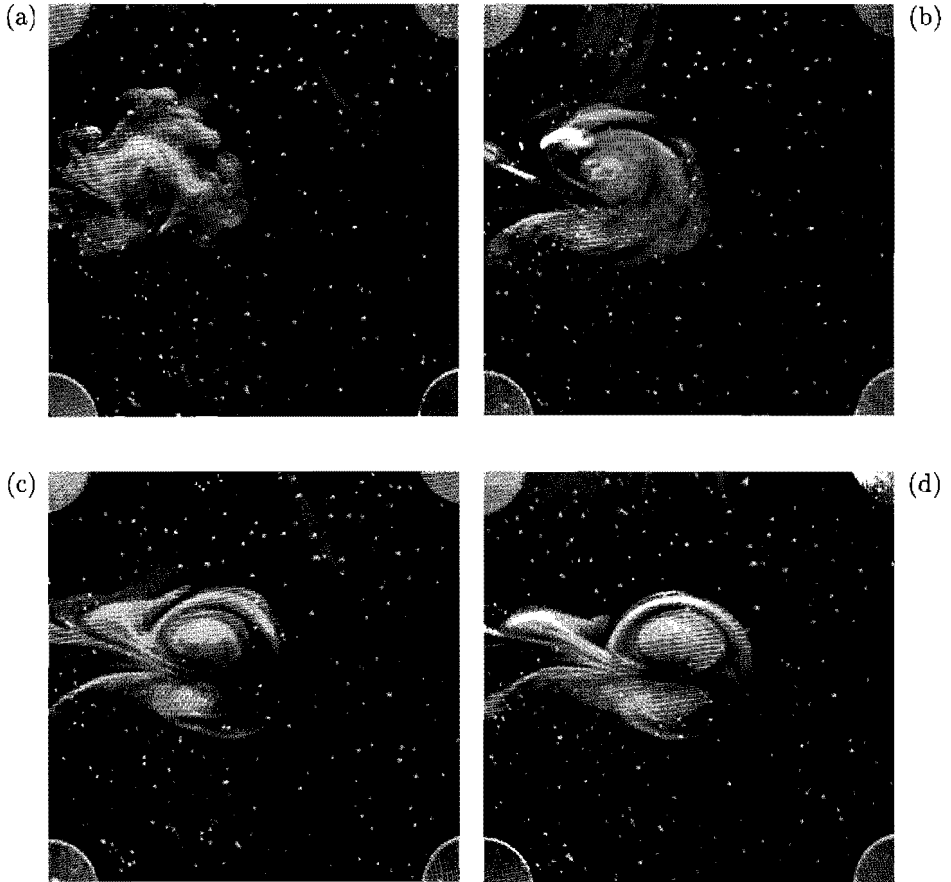


FIGURE 6.2: Sequence of video images showing the evolution of a dye-visualized dipolar vortex in a cooperative strain flow, with $e = 0.45 \times 10^{-2} \text{ s}^{-1}$. The images were taken at (a) $t = 10 \text{ s}$, (b) 20 s , (c) 30 s , (d) 40 s , (e) 50 s , (f) 60 s , (g) 70 s and (h) 80 s . Experimental parameters: $Q = 5.6 \text{ ml s}^{-1}$, $\delta t = 1.2 \text{ s}$, and $N = 3.5 \text{ rad s}^{-1}$.

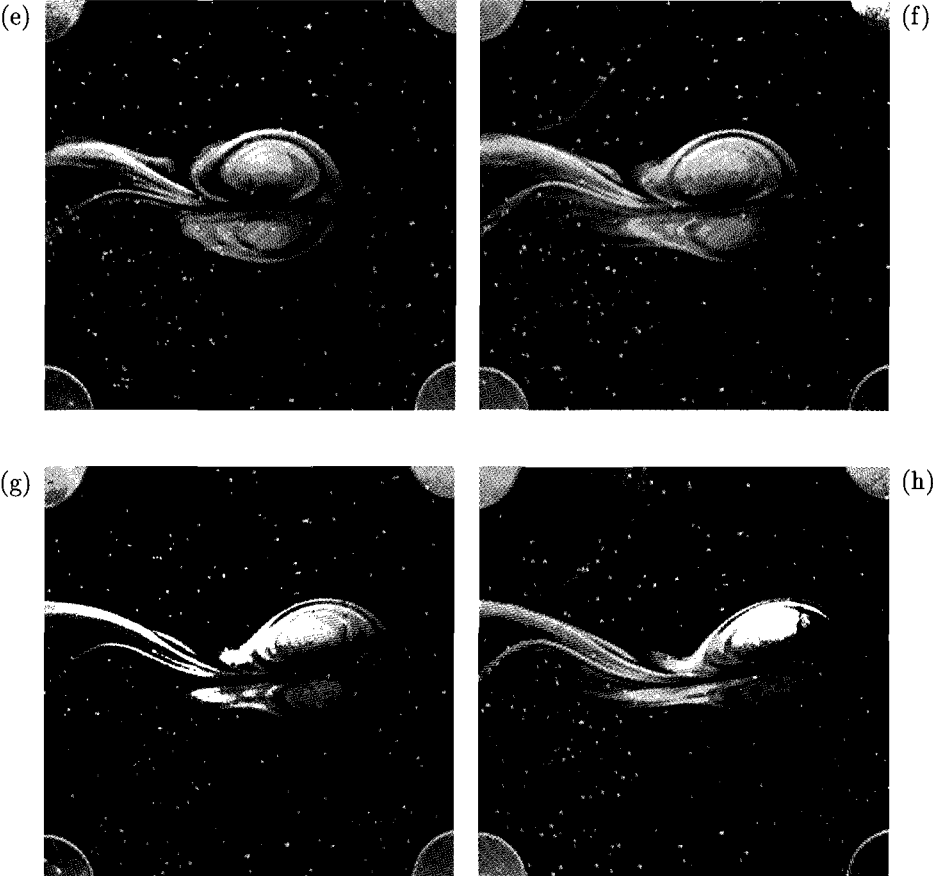


FIGURE 6.2: Continued.

at the rear side of the dipole, which leads to the spiral shape in the dye distributions. In the subsequent stage, however, the entrainment process is counteracted by the detrainment of dyed fluid.

6.3.2 Kinematic explanation of the head-tail formation

The formation of a head-tail structure can be explained by a simple kinematic approach. For this, the dipolar vortex is represented by a configuration of two point vortices of equal strengths, but opposite in sign. Supposing that these point vortices with strengths $-\gamma$ and γ are located at $(x, y) = (0, -b)$ and $(x, y) = (0, b)$, respectively, the point-vortex dipole will move steadily along the x -axis with a translation speed $U = \gamma/4\pi b$. Relative to a co-moving frame with velocity U (in which the flow is steady), the stream function associated with the vortex pair is given by

$$\psi(x, y) = \frac{\gamma}{4\pi} \ln \left[\frac{x^2 + (y - b)^2}{x^2 + (y + b)^2} \right] - Uy. \quad (6.1)$$

Figure 6.3(a) shows the steady flow pattern of the point-vortex dipole, in which two types of streamlines may be distinguished: closed streamlines, which surround one of the point vortices, and open streamlines, which extend to infinity. It is obvious that fluid particles are trapped inside the region of closed streamlines. This region of trapped fluid is usually called the ‘atmosphere’ of the dipole. The shape of the atmosphere boundary is given by the expression (see Thomson (1867))

$$x^2 = 2yb \coth \left(\frac{y}{2b} \right) - y^2 - b^2, \quad (6.2)$$

and can be approximated by an ellipse with axes $2.09b$ and $1.73b$. Furthermore, the flow contains two stagnation points located at $(x, y) = (-b\sqrt{3}, 0)$ and $(x, y) = (b\sqrt{3}, 0)$, respectively, which are the points of intersection of the atmosphere boundary and the streamline $y = 0$.

When the point-vortex dipole is exposed to a pure strain flow, the analytical velocity field in a co-moving reference frame is given by

$$u(x, y) = -\frac{\gamma}{2\pi} \frac{y - b}{x^2 + (y - b)^2} + \frac{\gamma}{2\pi} \frac{y + b}{x^2 + (y + b)^2} + ex - Uy \quad (6.3)$$

$$v(x, y) = \frac{\gamma}{2\pi} \frac{x}{x^2 + (y - b)^2} - \frac{\gamma}{2\pi} \frac{x}{x^2 + (y + b)^2} - ey, \quad (6.4)$$

where e represents the rate of strain. It should be noted that the relations (6.3) and (6.4) contain an implicit time dependence: owing to the interaction between the point-vortex dipole and the strain flow, the value of b varies according to $\dot{b} = -eb$, or

$$b(t) = b_0 \exp(-et), \quad (6.5)$$

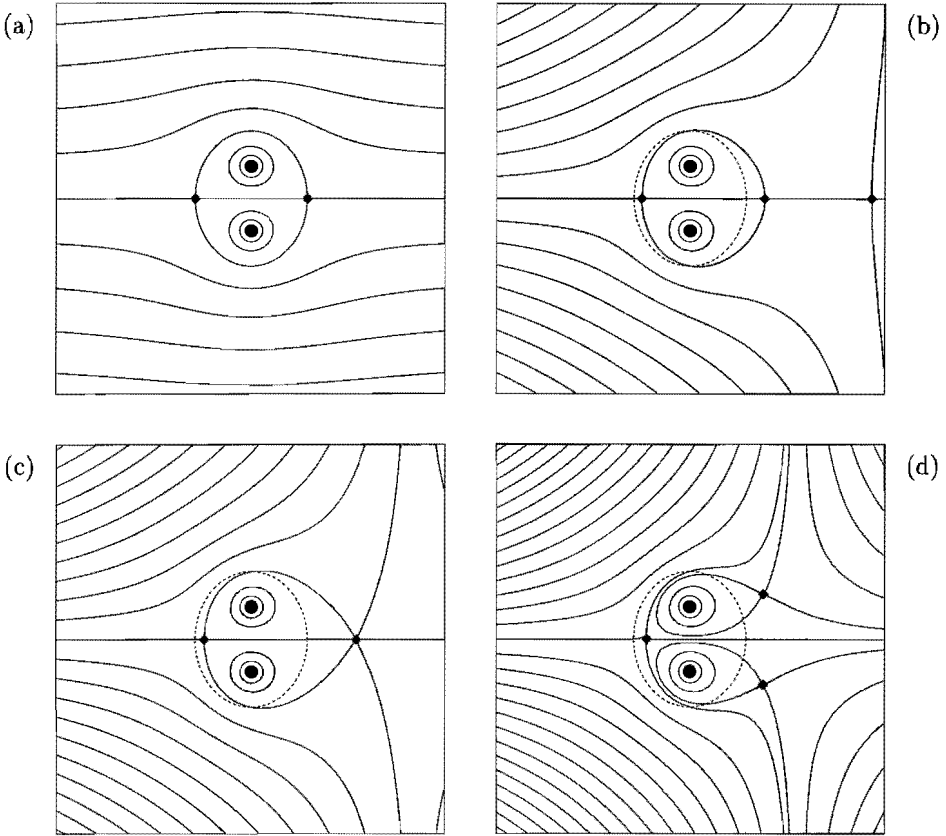


FIGURE 6.3: Streamline patterns associated with a point-vortex dipole in a co-moving reference frame for four different values of κ (see text): (a) $\kappa = \infty$ (no strain flow), (b) $\kappa = 80$, (c) $\kappa = \kappa_0 = 62.4$, and (d) $\kappa = 40$. The dashed lines correspond to the atmosphere boundary of the point-vortex dipole without the presence of a strain flow. The stagnation points are marked by a diamond.

with $b_0 = b(0)$. As a consequence, the distance $2b$ between the point vortices will decrease in a cooperative strain flow ($\epsilon > 0$). The stream function associated with (6.3) and (6.4) can be written as

$$\psi(x, y) = \frac{\gamma}{4\pi} \ln \left[\frac{x^2 + (y-b)^2}{x^2 + (y+b)^2} \right] + \epsilon xy - \frac{\gamma y}{4\pi b}, \quad (6.6)$$

where $U = \gamma/4\pi b$ has been used.

In order to find the corresponding stagnation points, it is convenient to introduce the complex velocity $V \equiv u + iv$, so that relations (6.3) and (6.4) can be combined into

$$V^* = -\frac{1}{2\pi i} \frac{\gamma}{z - ib} + \frac{1}{2\pi i} \frac{\gamma}{z + ib} - \frac{\gamma}{4\pi b} + \epsilon z, \quad (6.7)$$

where V^* represents the complex conjugate of V . On putting $V = 0$, and defining the dimensionless values $\zeta = z/b$ and $\kappa = \gamma/4\pi\epsilon b^2$, a cubic equation is obtained of the form

$$\zeta^3 - \kappa\zeta^2 - \zeta + 2\kappa = 0, \quad (6.8)$$

of which the three roots can be found by standard algebra. It is worth mentioning that the dimensionless parameter κ represents the ratio between the dipole translation speed U and the characteristic velocity ϵb induced by the strain flow. By defining

$$\kappa_0 = \pi \left(\frac{592}{3} + \frac{32}{3} (343)^{1/2} \right)^{1/2} \approx 62.4, \quad (6.9)$$

three different cases can be considered. If $\kappa > \kappa_0$, then the roots are real and unequal, which means that the three stagnation points are located at the symmetry axis (see figure 6.3(b)). If $\kappa = \kappa_0$, there will be three real roots of which two are equal. In other words, the symmetry axis will contain all stagnation points, of which two are degenerate (see figure 6.3(c)). Finally, if $\kappa < \kappa_0$ there will be one real root and two conjugate imaginary roots, i.e. one stagnation point will lie on the symmetry axis, whereas the two others are mirrored with respect to the symmetry axis (see figure 6.3(d)). Note that each conjugate imaginary root is associated with the self-intersection of a streamline.

Also shown in figures 6.3(b)–(d) is the boundary of the atmosphere associated with the point-vortex dipole in an otherwise quiescent fluid (dashed lines). If the strain flow were absent, all fluid particles inside this atmosphere would be trapped and consequently move along with the dipole. However, if the point-vortex pair is submitted to a strain flow, part of the tracers enclosed by the original atmosphere (i.e. with the strain flow being absent) will be located in the exterior region. In other words, a new ‘atmosphere’ is formed which only partly catches the tracers enclosed by the dashed line. Consequently, additional external fluid is present at the rear of the point-vortex dipole. It is important to note that the velocity field (6.7) is unsteady, so that the streamline patterns as shown in figures 6.3(b)–(d) only indicate the instantaneous direction of particle movement. Nevertheless, the streamline patterns depicted in figures 6.3(b)–(d) clearly explain the formation of a head-tail structure.

6.3.3 Quantitative observations

The formation of the head-tail structure is also nicely illustrated by the vorticity contour plots presented in figure 6.4(a)–(d), in which the vorticity contours around the rotating discs have been eliminated for clarity. Note that in this case, and those that follow, the translational motion of the dipole has been chosen along the vertical axis. Like in the dye-visualization experiment, the dipole is elongated in the axial direction, while simultaneously a tail is being formed at the rear side of each dipole half. These results are in good qualitative agreement with the numerical simulations as obtained by Kida, Takaoka & Hussain (1991). Likewise, a similar head-tail asymmetry was observed by Flór & van Heijst (1994) in their study on laminar-injection dipoles in a quiescent ambient fluid. However, in their case, the asymmetry and the deformation of the vortex were due to the initial forcing with a jet. Moreover, their experiments revealed that the dipole gradually relaxed towards an approximately circular shape, whereas the present results show the opposite.

Figure 6.5(a) shows a sequence of cross-sectional distributions of vorticity which correspond to the experimental observations depicted in figure 6.4(b)–(d). The vorticity profile associated with figure 6.4(a) was excluded since the dipole was not completely developed by that time. The cross-sections were taken along a line intersecting both vortex centres, and the vorticity values in between the grid points were obtained by bilinear interpolation. The vorticity has been scaled with the maximum vorticity value ω_0 at $t = 40$ s (figure 6.4(b)), whereas the spatial coordinate has been normalized with the initial distance d_0 between the vortex centres. It can be seen that the profiles are approximately self-similar in time. Moreover, the instantaneous distance d between the vortex centres remains nearly constant until about $t = 70$ s, as can be inferred from figure 6.6. If the vortex centres were passively advected by the strain flow, d would approximately decrease by a factor 1.6 during the course of the experiment (i.e. $d/d_0 \approx 0.64$, based on the strain rate constant $\epsilon = 0.45 \times 10^{-2} \text{ s}^{-1}$ and the typical duration of the experiment, which is 100 s). It is therefore most likely that the compressive effect of the straining flow is counteracted by lateral diffusion of vorticity, and also by the initial entrainment of irrotational ambient fluid at the rear side of the dipole. In the final stage, however, the distance between the vortex centres decreases significantly as a result of the nonuniformity of the strain flow: it was shown in chapter 3 that the local rate of strain increases at larger radii from the centre of the tank. Apparently, the strain rate is eventually large enough to overcome the effect of lateral diffusion.

Additional cross-sectional distributions of vorticity were taken across the tails of the dipolar vortex. A typical vorticity profile is shown in figure 6.7(a), where the cross-section was taken along the horizontal line depicted in figure 6.4(d). Obviously, the left and right tail are associated with positive and negative vorticity, respectively. The asymmetry in the vorticity distributions is due to the asymmetric shedding of vorticity at the rear side of the vortex.

Some more information about the dipolar vortex characteristics can be obtained by plotting the vorticity ω against the stream function ψ in a so-called scatter plot for a large number of grid points. Figure 6.8(a) shows the scatter plot corresponding to the head of

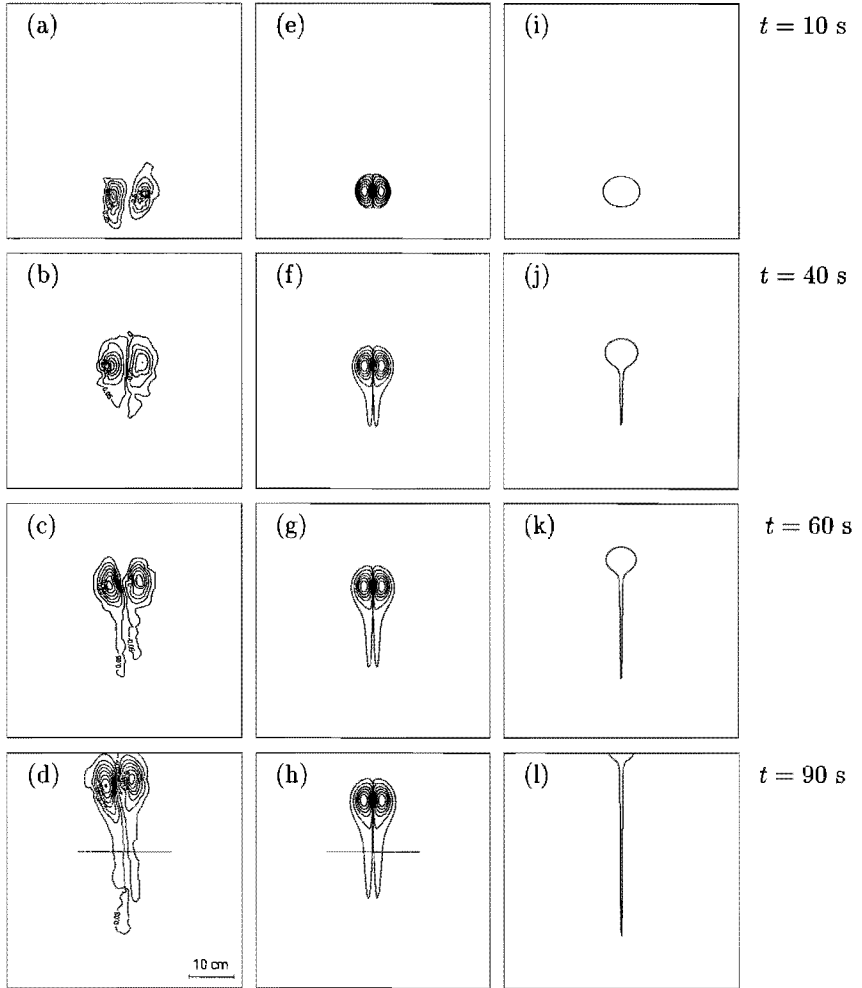


FIGURE 6.4: Experimental and numerical results for a dipolar vortex in a cooperative strain flow. Panels (a)–(d) show the observed evolution of the spatial vorticity distribution. The time-evolution of the Lamb-Chaplygin vortex as calculated by the finite-difference method is depicted in panels (e)–(h); for each plot, the contour levels correspond to 1%, 10%, 30%, 50%, 70% and 90% of the instantaneous extremal vorticity, respectively. Numerical parameters: $a = 3.7$ cm, $U_0 = 0.98$ cm s $^{-1}$ and $\epsilon = 0.45 \times 10^{-2}$ s $^{-1}$. Along the horizontal lines depicted in frames (d) and (h), the cross-sectional distributions of vorticity were determined (see figure 6.7). Panels (i)–(l) show the time-evolution of passive tracers as obtained by the contour kinematics technique. The tracers were initially located at the boundary of the vortex-pair atmosphere, see (i). The numerical parameters are: $a = 2b = 3.7$ cm, $C = 173/1.09$ cm 2 s $^{-1/2}$, and $\tau = 85$ s.

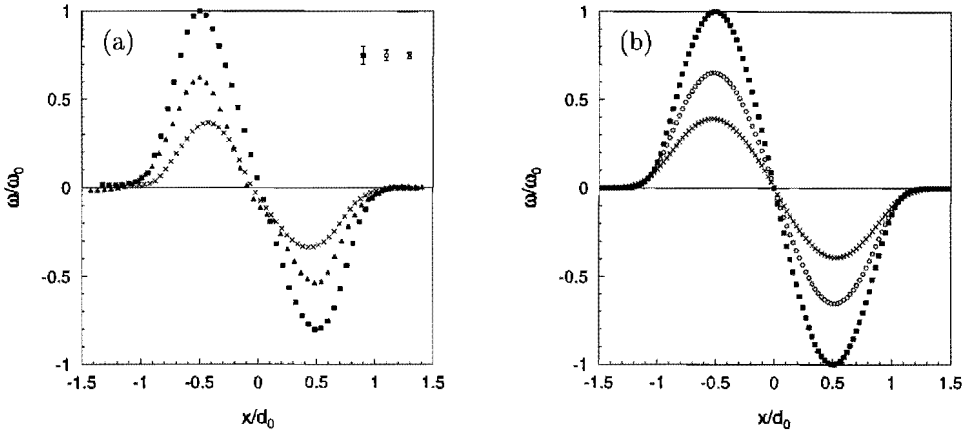


FIGURE 6.5: Experimental and numerical results for a dipolar vortex in a cooperative strain flow. Panel (a) shows the cross-sectional distributions of vorticity along a horizontal line through the vortex centres of the laboratory dipoles which are shown in figure 6.4(b)–(d). The vorticity has been scaled with the initial maximum vorticity $\omega_0 = 1.04 \text{ s}^{-1}$ (at $t = 40 \text{ s}$), whereas the spatial coordinate has been normalized by the corresponding distance between the vortex centres $d_0 = 6.58 \text{ cm}$ (see figure 6.4(b)). Panel (b) shows similar vorticity profiles which are based on the finite-difference results depicted in figure 6.4(f)–(h), with $\omega_0 = 1.03 \text{ s}^{-1}$ and $d_0 = 3.70 \text{ cm}$ at $t = 40 \text{ s}$ (see figure 6.4(f)).

the dipolar vortex depicted in figure 6.4(d). The stream function ψ has been corrected for the translation speed (U_x, U_y) of the dipolar vortex according to $\psi' = \psi - U_x y + U_y x$, where U_x and U_y have been obtained from the displacements of the vortex centres. Furthermore, the vorticity and the stream function have been scaled with their extremal values ω_m and ψ'_m , respectively. Obviously, the positive and negative branches are related to one of the dipole halves, whereas the horizontal band around $\omega = 0$ is associated with the exterior potential flow. The scatter is more pronounced for weaker vorticity values, indicating that the scatter is mainly caused by the continuous deformation of the dipole by the strain flow, i.e. most part of the scatter is related to the edge of the dipole where vorticity is being removed and being shed in the form of two tails. Despite the scatter, an approximately linear relationship is present inside the dipolar vortex.

A theoretical model of a dipolar vortex with a linear (ω, ψ') -relationship is the so-called Lamb-Chaplygin dipole model (see Lamb (1932), Batchelor (1967) and Meleshko & van Heijst (1994a)). This model is based on the steady Euler equations, and assumes a linear relationship $\omega = k^2 \psi'$ (with k being a constant) inside a circular region with radius a , while in the exterior region ($r > a$) an irrotational flow is assumed. The stream function

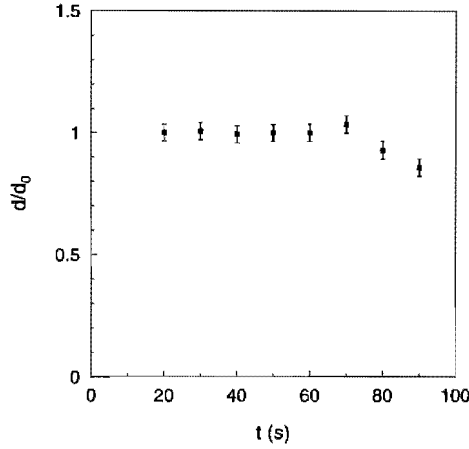


FIGURE 6.6: The measured distance d/d_0 plotted as a function of time. The distance d between the points of maximum and minimum vorticity has been scaled with the initial distance $d_0 = 6.58$ cm (at $t = 20$ s). The experimental data are based on the experiment depicted in figure 6.4(a)–(d).

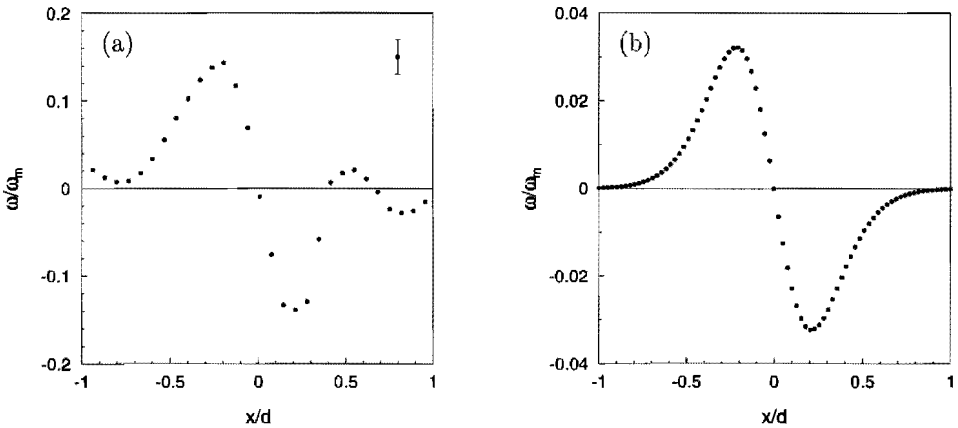


FIGURE 6.7: (a) Measured cross-sectional distribution of vorticity across the tails of the dipolar vortex depicted in figure 6.4(d). The vorticity has been scaled with its extremal value $\omega_m = 0.38 \text{ s}^{-1}$ (corresponding to one of the vortex centres), whereas the spatial coordinate has been normalized by the distance between the vortex centres $d = 5.62$ cm. (b) Corresponding calculated profiles, see figure 6.4(h), with $\omega_m = 0.40 \text{ s}^{-1}$ and $d = 3.90$ cm.

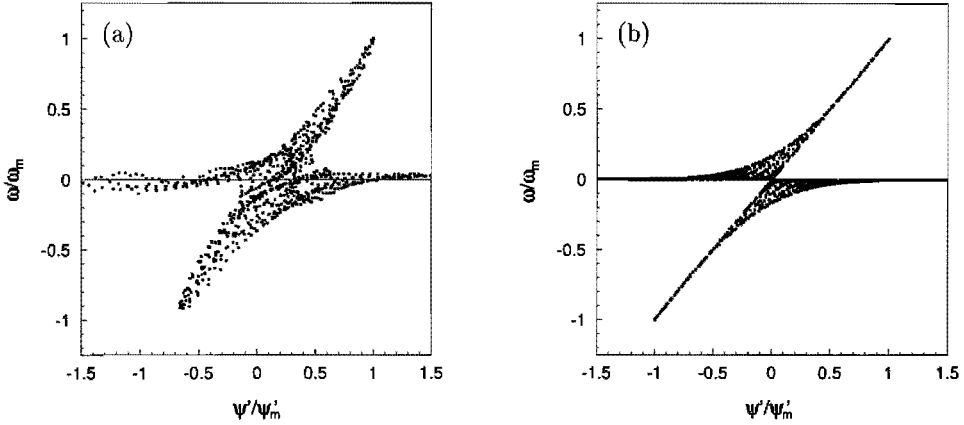


FIGURE 6.8: (a) Characteristic (ω, ψ') -scatter plot of the laboratory vortex shown in figure 6.4(d), where the stream function ψ has been corrected according to $\psi' = \psi - U_x y + U_y x$, with (U_x, U_y) the translation speed of the dipole. The vorticity and the stream function have been scaled by their extremal values ω_m and ψ'_m , respectively. Experimental values: $\omega_m = 0.39 \text{ s}^{-1}$, $\psi'_m = 1.09 \text{ cm}^2 \text{ s}^{-1}$, $(U_x, U_y) = (-0.03, 0.32) \text{ cm s}^{-1}$. (b) Numerically obtained (ω, ψ') -scatter plot corresponding to figure 6.4(h). Numerical values: $\omega_m = 0.40 \text{ s}^{-1}$, $\psi'_m = 1.61 \text{ cm}^2 \text{ s}^{-1}$, $(U_x, U_y) = (0, 0.235) \text{ cm s}^{-1}$.

and the vorticity associated with the Lamb-Chaplygin dipole are given by

$$\psi'(r, \theta) = \begin{cases} -\frac{2U_{LC}}{kJ_0(ka)} J_1(kr) \sin \theta & \text{if } r \leq a \\ U_{LC} \left(r - \frac{a^2}{r} \right) \sin \theta & \text{if } r > a \end{cases} \quad (6.10)$$

$$\omega(r, \theta) = \begin{cases} -\frac{2U_{LC}k}{J_0(ka)} J_1(kr) \sin \theta & \text{if } r \leq a \\ 0 & \text{if } r > a, \end{cases} \quad (6.11)$$

respectively, where polar coordinates (r, θ) have been used for convenience. The functions J_0 and J_1 are the first- and second-order Bessel function of the first kind, respectively, and U_{LC} represents the uniform fluid velocity at infinity (which is equal to the dipole's translation speed in a fixed frame of reference). Continuity of velocity at $r = a$ requires that $J_1(ka) = 0$, i.e. $ka = 3.83$. Furthermore, it can be derived from (6.11) that the circulation γ_{LC} in each dipole half is equal to $6.83U_{LC}a$, and that the distance d between the points of extremal vorticity is equal to $0.96a$ (so that $kd = 3.68$).

In figure 6.8(a), the data points associated with the positive and negative branches were least-square fitted with the linear relationship $\omega = k^2 \psi'$, which yielded the slope $k^2 = 0.40 \pm 0.10 \text{ cm}^{-2}$. By measuring the corresponding distance d between the vortex centres from the vorticity profile in figure 6.5(a) (indicated by the crosses), the value

$kd = 3.6 \pm 0.6$ was obtained, which is close to the theoretical value $kd = 3.68$ related with the Lamb-Chaplygin model. Thus, despite the deformation of the dipolar vortex, the Lamb-Chaplygin model apparently still applies to the main part of the dipolar vortex.

It was shown by Flór & van Heijst (1994) that dipolar vortices generated by turbulent injection are characterized by a sinh-like (ω, ψ') -relationship. In their experimental study, this nonlinear relationship was ascribed to the weak linking between the positive and negative vorticity patches; that is, the vortex centres were further apart than expected from the Lamb-Chaplygin model. Since the cross-sectional distributions in figure 6.5(a) show a strong linking between the vortex centres, and the nonlinearity of the (ω, ψ') -relationship in figure 6.8(a) is less pronounced than in the experimental observations by Flór & van Heijst (1994), it may be concluded that the (ω, ψ') -relationship of turbulent-injected dipoles in a cooperative strain flow is more linear due to the compressive action of the ambient flow.

6.3.4 Numerical simulations

Finite-difference method

Stratified fluid experiments by Flór & van Heijst (1994) have shown that dipolar vortices are characterized by a pancake-like shape. The same authors demonstrated by a scaling analysis that in a thin region around the mid-plane ($z = 0$) vortex tilting by the vertical shear is negligible, and that the vertical vorticity ω is to leading order governed by

$$\frac{\partial \omega}{\partial t} + J(\omega, \psi) = \nu \nabla_h^2 \omega + \nu \frac{\partial^2 \omega}{\partial z^2}, \quad (6.12)$$

where $\omega = -\nabla_h^2 \psi$, ∇_h^2 is the Laplace operator acting in the horizontal directions, and J represents the Jacobian.

In the present study, the quasi-two-dimensional vorticity equation (6.12) was solved in the horizontal plane $z = 0$ by a finite-difference method that is second-order accurate both in space and in time (see Orlandi (1990)). The same numerical method has been used successfully in chapter 3 and 4 to model the evolution of monopolar vortices in a strain flow. The time-integration was performed with a variable time step, such that $CFL = 0.5$, and the computational domain was represented by a 256×256 grid. The strain flow was included as a boundary condition for the Poisson equation. Furthermore, it was assumed that at $t = 0$ the vorticity is distributed according to $\omega = \omega(x, y)\delta(z)$, with $\omega(x, y)$ the horizontal distribution of the vertical vorticity and δ the Dirac delta function (see Flór & van Heijst (1994)). Hence, the vertical diffusion term in (6.12) could be written as

$$\left. \frac{\partial^2 \omega}{\partial z^2} \right|_{z=0} = -\frac{\omega}{2t}, \quad (6.13)$$

which applies for $t > 0$ and $z = 0$ (see chapter 3). As a result, the vorticity equation (6.12) is independent of z and can be easily treated by the finite-difference code.

As an initial condition, the vorticity distribution associated with Lamb-Chaplygin dipole model was used, where the relevant initial parameters (i.e. the distance d and the wavenumber k) were based on typical laboratory values. Considering the singularity at $t = 0$ and the typical time scale on which the dipole was formed, the simulation was initiated at $t = 10$ s.

The calculated evolution of the Lamb-Chaplygin dipole in a cooperative strain flow is shown by the vorticity contours plotted in figure 6.4(e)–(h), and the formation of the head-tail structure is obvious. Figure 6.5(b) shows the distributions of vorticity along the line intersecting both vortex centres, which correspond to figures 6.4(f)–(h). The numerically obtained vorticity distributions are in very good qualitative agreement with the observed profiles given in figure 6.5(a). In both cases, the profiles have similar shapes, and the distance d between the positions of extremal vorticity remains virtually constant. Additional numerical simulations have shown that the balance between advection and lateral diffusion of vorticity does not hold for all values of e : for larger strain rates e , the vortex centres were observed to approach each other. Similar numerical results were obtained by Kida, Takaoka & Hussain (1991).

The calculated cross-sectional distribution of vorticity across the tails of the dipolar vortex are shown in figure 6.7(b), and are in good qualitative agreement with the laboratory observations (figure 6.7(a)). The magnitude of vorticity is experimentally larger than in the numerical simulation: owing to the nonuniformity of the experimental strain flow the shedding of vorticity at the dipole boundary is intensified, leading to higher vorticity values in the tails of the dipole.

In figure 6.8(b), the numerically obtained scatter plot is provided for the dipolar vortex shown in figure 6.4(h), and a good qualitative agreement is obtained with the laboratory observations depicted in figure 6.8(a). Close to the vortex centres the (ω, ψ) -relation is linear, whereas at lower levels of vorticity considerable scatter occurs due to the shedding of low-level vorticity. Besides experimental errors, the scatter in figure 6.8(a) is more pronounced because the laboratory vortex experienced a larger strain rate (due to the nonuniformity of the experimental strain flow) than in the numerical simulation.

The scatter in figures 6.8(a) and (b) may also be caused by viscous effects. Since the initially imposed Lamb-Chaplygin dipole is discontinuous in $\partial\omega/\partial\theta$ on the circle $r = a$, the kink in the vorticity profile will be smoothed out by viscous diffusion. As a result, the Jacobian becomes non-zero in a thin layer near the circular boundary $r = a$. However, it was shown by Kida, Takaoka & Hussain (1991) that this nonlinear effect is small as long as $t \ll T_d$, with $T_d = a^2/\nu$ the characteristic time scale on which the viscous layer spreads over the whole vortex structure. In the present study, the dipole radius a was typically 5 cm, implying that $T_d \approx 2500$ s, which is much larger than both the duration of the experiment and that of the numerical simulation. Moreover, additional finite-difference simulations have revealed much less scatter at the weaker vorticity levels when the strain flow was absent. Nevertheless, the continuous removal of the weaker vorticity levels may increase the spatial vorticity gradient at the boundary, leading to an accelerated outward diffusion flux (see Mariotti, Legras & Dritschel (1994)).

Contour kinematics method

It was shown above that the formation of a head-tail structure can be explained by considering the strain-induced evolution of a point-vortex dipole and its original atmosphere. For that reason it is interesting to calculate the deformation of the atmosphere boundary and to make a comparison with both the experimental and full-numerical results. For this, the contour kinematics method is adopted here, which implies that a material contour is followed in an analytically prescribed velocity field. The material line is composed of a large number of markers, which are displaced in time by a Runge-Kutta method with variable time step and order (see Hairer, Nørset & Wanner (1987)). For a detailed description of the contour kinematics technique, the reader is referred to the paper by Meleshko & van Heijst (1994b). In the present study, the analytical velocity field is represented by that of a point-vortex dipole in a straining flow (see (6.3) and (6.4)).

In order to compare the point-vortex pair with the Lamb-Chaplygin dipole, two important physical quantities were taken the same: the total impulse (being $2b\gamma\rho$ and $2\pi a^2\rho U_{LC}$, respectively) and the translation speed (being $\gamma/4\pi b$ and U_{LC} , respectively). As a result, $a = 2b$ and $\gamma_{LC} = 1.09\gamma$. In order to account for the decay of circulation, which is mainly due to diffusion of vorticity in the vertical direction, γ was made time-dependent according to the decay of circulation as obtained by the finite-difference method. In fact, the calculated decay of circulation could be very accurately described by the analytical function $\frac{C}{\sqrt{t}} \exp(-t/\tau)$, with τ a characteristic time scale associated with the decay of vorticity in the horizontal directions (see Flór, van Heijst & Delfos (1995) for more details). Both the initial position of the point-vortex pair and the strain rate constant were taken the same as in the finite-difference simulation. The tracers were initially distributed on the separatrix associated with the point-vortex dipole in an otherwise quiescent fluid.

Figure 6.4(i)–(l) shows that the initially elliptic material line is deformed into a head-tail structure, as expected from the streamline patterns depicted in figure 6.3(b)–(d). Since the initial contour encloses both point vortices, only one tail shows up in the contour kinematics simulation. It is apparent that the translation speed of the vortex pair is larger compared to the experimental and full-numerical results. This can be explained by noting that the point vortices are passively advected by the strain flow according to (6.5), so that the self-induced translation speed $U = \gamma/4\pi b$ of the point-vortex dipole increases more rapidly than in the viscous case, where the convergence of the dipole centres is counteracted by horizontal diffusion of vorticity. Likewise, the absence of viscous effects may explain why the tail associated with the contour kinematics simulation is much thinner than in the laboratory experiments and the finite-difference simulation. Nevertheless, this simple approach clearly demonstrates the formation of a head-tail structure.

6.4 Dipolar vortex in adverse strain flow

6.4.1 Laboratory observations

The qualitative behaviour of a dipolar vortex in an adverse strain flow is displayed by the video images shown in figure 6.9. Shortly after the turbulent-injected fluid has collapsed under gravity, a dipolar vortex appears which entrains a considerable amount of noncoloured ambient fluid (see (a)–(c)). In the next stage, see (d)–(f), the dipole halves gradually separate by the action of the background strain flow, i.e. the dipole breaks up into two monopolar vortices. It is interesting to note that both monopoles are oriented at an angle of approximately 45 degrees with respect to the horizontal strain axis. Similar observations were made in analytical, numerical and experimental studies on monopolar vortices in strain flows (see e.g. Kida (1981), Legras & Dritschel (1993) and chapter 3, respectively), where it was shown that this orientation corresponds to the quasi-stationary state of a monopolar vortex in a strain flow.

The measured vorticity fields are shown in figure 6.10(a)–(d) at four different times, and a similar behaviour is observed as in the dye-visualization experiments. The separation of the vortex centres is also clear from the cross-sectional distributions of vorticity depicted in figure 6.11(a)–(d), where the cross-sections were taken along the line intersecting both vortex centres.

In order to examine whether the dipole halves were passively advected by the strain flow, the distance d between the vortex centers was determined from cross-sectional distributions as shown in figure 6.11(a)–(d). In figure 6.12, the distance d/d_0 is plotted logarithmically as a function of time, with d_0 the distance d at $t = 20$ s. The exponential increase is obvious, at least up to $t = 150$ s. Hence, the experimental data corresponding to $t \leq 150$ s were least-square fitted with an exponential function of the form $\exp(\beta t)$ (see (6.5)), which is displayed by a straight line in figure 6.12. The parameter β was found to be equal to $(0.73 \pm 0.05) \times 10^{-2} \text{ s}^{-1}$, which is in excellent agreement with the strain rate constant $e = (0.68 \pm 0.01) \times 10^{-2} \text{ s}^{-1}$. The final accelerated increase of d is due to the nonuniformity of the strain flow (see chapter 3). In view of the above results, it may be concluded that the vortex centres are passively advected by the strain flow.

The monopolar vortex characteristics were investigated by plotting the distribution of vorticity along a horizontal line through one vortex centre. Figure 6.13(a) shows such a vorticity profile corresponding to the monopolar vortex depicted on the left-hand side of figure 6.10(c), which obviously has only single-signed vorticity. A possible model for a nonisolated vortex is the so-called Lamb vortex (see Lamb (1932)), for which the radial distributions of vorticity and azimuthal velocity are given by

$$\omega(r) = \frac{\gamma_L}{\pi R^2} \exp(-r^2/R^2) \quad (6.14)$$

$$v_\theta(r) = \frac{\gamma_L}{2\pi r} [1 - \exp(-r^2/R^2)], \quad (6.15)$$

respectively, with γ_L the total circulation of the Lamb vortex, and R a characteristic length scale. The experimental data in figure 6.13(a) were least-square fitted with (6.14) and show a very good agreement with the Lamb-vortex model.

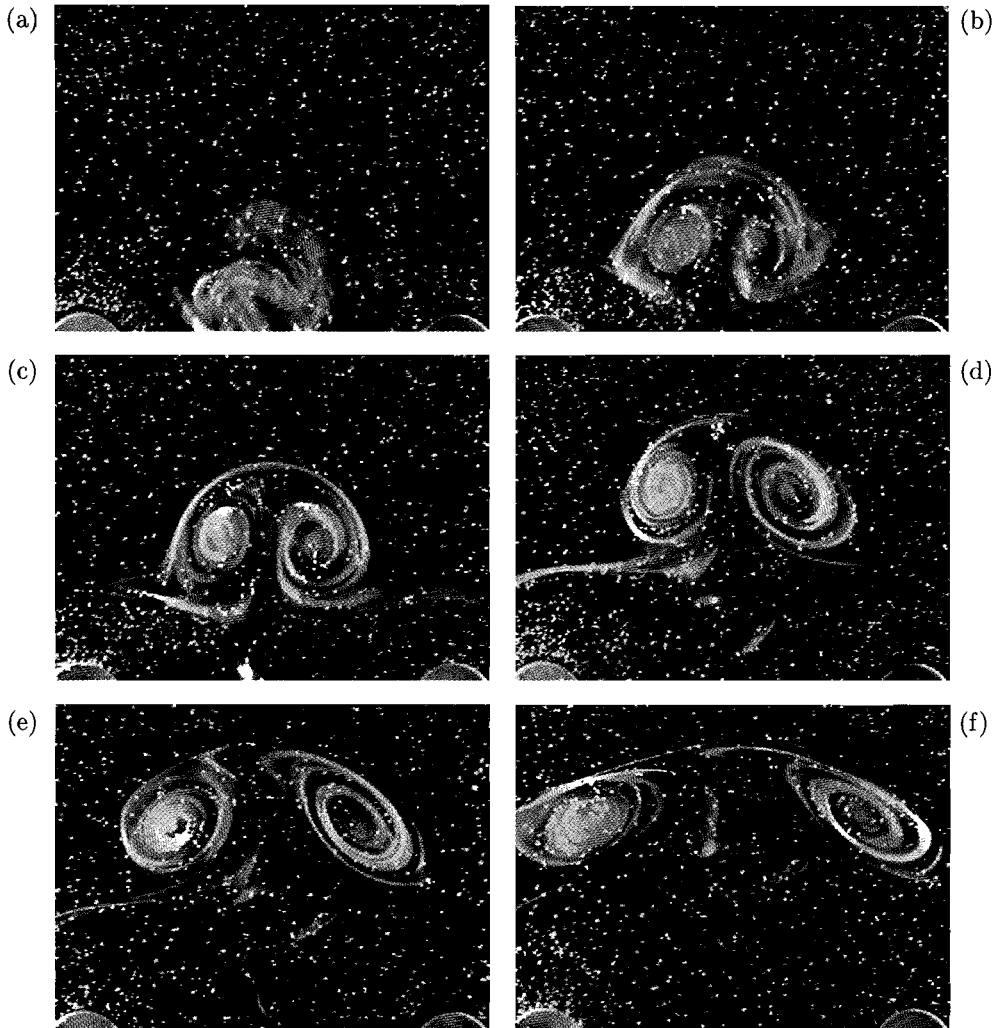


FIGURE 6.9: Sequence of video images illustrating the evolution of a dye-visualized dipolar vortex in an adverse strain flow with $e = 0.68 \times 10^{-2} \text{ s}^{-1}$. The images were taken at (a) $t = 10$ s, (b) 30 s, (c) 50 s, (d) 90 s, (e) 130 s and (f) 170 s. Experimental parameters: $Q = 5.6 \text{ ml s}^{-1}$, $\delta t = 1.2$ s, and $N = 3.5 \text{ rad s}^{-1}$.

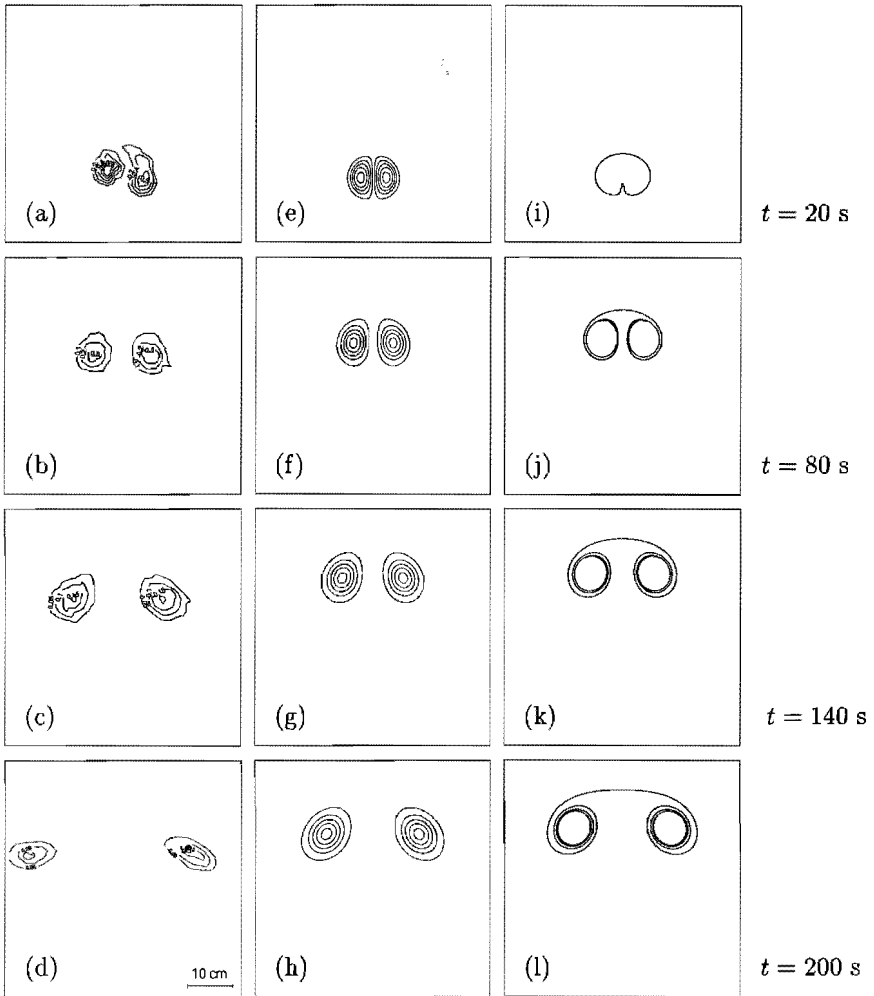


FIGURE 6.10: Experimental and numerical results for a dipolar vortex in an adverse strain flow. Panels (a)–(d) show the observed evolution of the spatial vorticity distribution. The time-evolution of the Lamb-Chaplygin vortex as calculated by the finite-difference method is depicted in panels (e)–(h); for each plot, the contour levels correspond to 10%, 30%, 50%, 70% and 90% of the instantaneous extremal vorticity, respectively. The numerical parameters are: $a = 5.3$ cm, $U_0 = 0.88$ cm s $^{-1}$ and $e = 0.70 \times 10^{-2}$ s $^{-1}$. Panels (i)–(l) show the time-evolution of passive tracers as obtained by the contour kinematics technique. The tracers were initially distributed on the separatrix associated with the point-vortex dipole in an otherwise quiescent fluid. The numerical parameters are: $a = 2b = 5.3$ cm and $C = 102/1.09$ cm 2 s $^{-1/2}$.

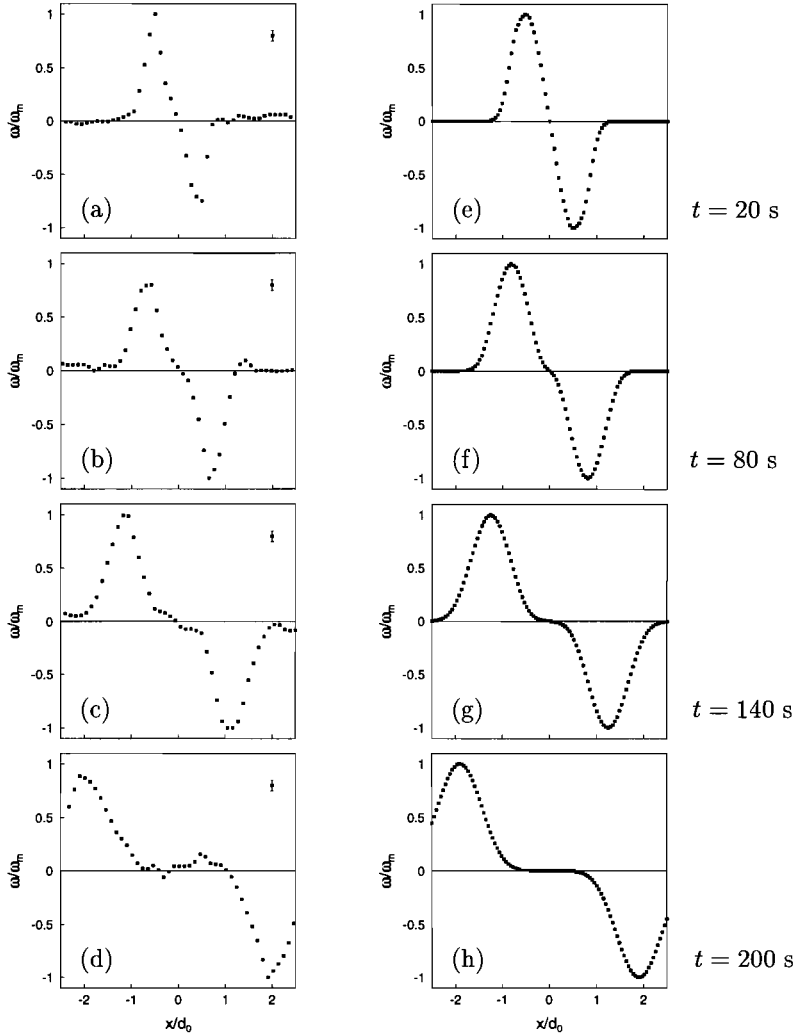


FIGURE 6.11: Experimental and numerical results for a dipolar vortex in an adverse strain flow. In panels (a)–(d), the cross-sectional distributions of vorticity are plotted along a horizontal line through the vortex centres of the laboratory dipoles which are shown in figure 6.10(a)–(d), respectively. In each plot, the vorticity ω has been scaled with its extremal value ω_m , whereas the spatial coordinate has been normalized by the initial distance between the vortex centres $d_0 = 8.85$ cm (at $t = 20$ s). The extremal vorticity ranged from $\omega_m = 1.14$ s $^{-1}$ at $t = 20$ s to $\omega_m = 0.14$ s $^{-1}$ at $t = 200$ s. In frames (e)–(h), similar normalized vorticity profiles are shown related to the finite-difference results depicted in figure 6.10(e)–(h). The extremal vorticity ω_m varied from 1.21 s $^{-1}$ at $t = 20$ s to 0.17 s $^{-1}$ at $t = 200$ s. Furthermore, $d_0 = 5.2$ cm (at $t = 20$ s).

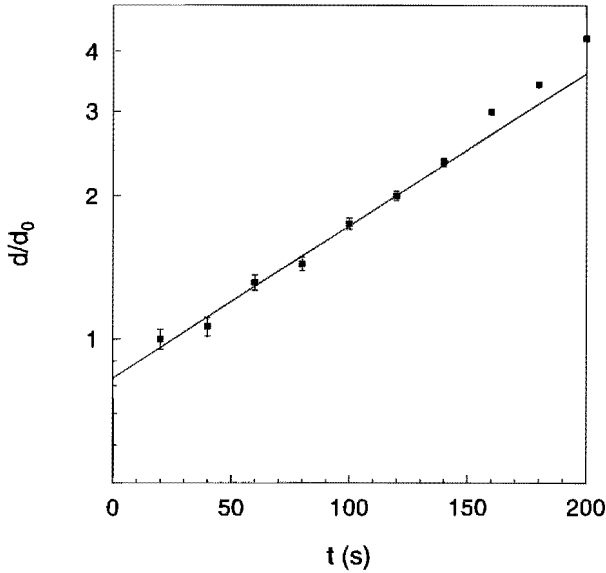


FIGURE 6.12: The measured distance d/d_0 plotted logarithmically as a function of time, where d represents the distance between the points of maximum and minimum vorticity, and $d = d_0 = 4.43$ cm at $t = 20$ s. The experimental data have been obtained from the experiment observations (figure 6.10(a)–(d)) and were least-square fitted by an exponential function of the form $\exp(\beta t)$, with β a free parameter.

In addition, the scatter-plot of the observed monopolar vortex is displayed in figure 6.14(a), where the stream function ψ has been corrected for the translation velocity of the vortex centre. The vorticity and the stream function have been scaled with their extremal values ω_m and ψ'_m , respectively. The scatter is probably caused by the continuous deformation of the monopole and the measurement errors. Also indicated is the analytical (ω, ψ) -relationship according to the Lamb-vortex model (solid line in figure 6.14(a)). Since the theoretical and measured (ω, ψ) -relationships are in good agreement, it can be concluded that the characteristics of the elliptic-shaped monopolar vortices are very similar to those of the Lamb vortex.

6.4.2 Numerical simulations

Figure 6.10(e)–(h) provides the calculated evolution of a Lamb-Chaplygin vortex in an adverse strain flow, where the quasi-two-dimensional vorticity equation (6.12) was solved by the same finite-difference method as described in the preceding section. Likewise, the initial conditions were taken from the experiments, and the simulation was started at $t = 10$ s. Comparison with figure 6.10(a)–(d) reveals that the numerical results are in

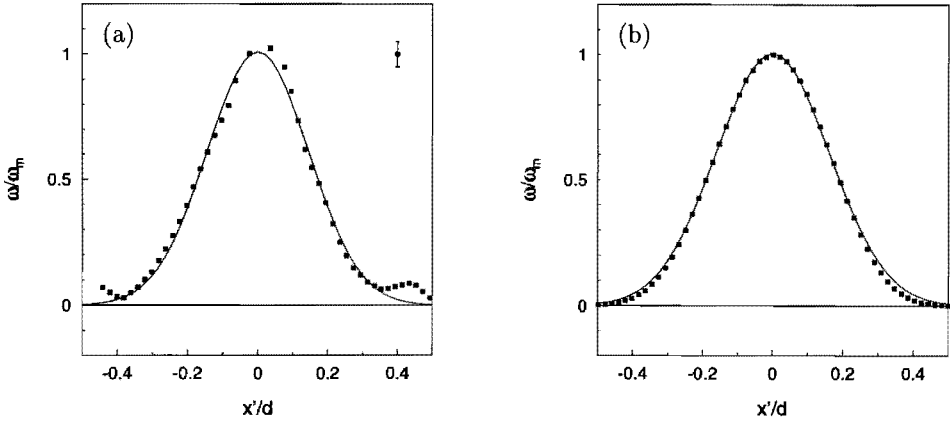


FIGURE 6.13: (a) Measured cross-sectional distribution of vorticity along a horizontal line through the vortex centre displayed on the left-hand side of figure 6.10(c). The vorticity ω has been scaled with its maximum value $\omega_m = 0.20 \text{ s}^{-1}$, while the spatial coordinate x' has been scaled with the distance between the vortex centres $d = 19.7 \text{ cm}$. The solid line corresponds to (6.14) and has been least-square fitted to the experimental data. (b) The corresponding vorticity profile as obtained by the finite-difference calculation (see figure 6.10(g)), with $\omega_m = 0.259 \text{ s}^{-1}$ and $d = 13.0 \text{ cm}$, and a least-square fit through the numerical data according to (6.14).

good qualitative agreement with the laboratory observations, which is evident from the separation as well as the orientation of both dipole halves.

Also shown are the corresponding cross-sectional distributions of vorticity through the vortex centres (see figure 6.11(e)–(h)), which have similar characteristics as observed in the laboratory (see figure 6.11(a)–(d)).

The characteristics of the monopolar vortices were investigated numerically by taking cross-sectional distributions of vorticity along a line through a single vortex centre, as shown in figure 6.13(b), and by plotting the vorticity versus the stream function in a scatter plot, as displayed in figure 6.14(b). The vorticity profiles as well as the scatter plots have been compared with the Lamb-vortex model. The numerical results definitely confirm the formation of two Lamb-like monopoles after the break-up of the Lamb-Chaplygin dipole.

Since the point-vortex model can explain the formation of a head-tail structure, it is interesting to examine whether this simple model can also describe the characteristic features of a dipolar vortex in an adverse strain flow. The relevant initial parameters were taken from the experiments, and the same correction was made as in the previous section to link the point-vortex model to the Lamb-Chaplygin dipole. The circulation of each point vortex was modulated by the analytical function C/\sqrt{t} , which proved to describe the decay of circulation as obtained by the finite-difference simulations very well.

Figure 6.10(i)–(l) displays the evolution of the material contour, which initially corresponded to the atmosphere boundary of a vortex pair in an otherwise still fluid. The

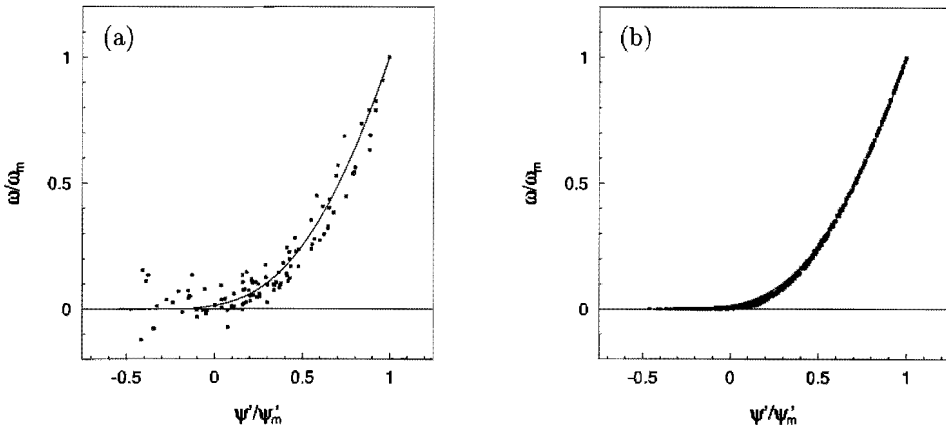


FIGURE 6.14: (a) Characteristic (ω, ψ') -scatter plot corresponding to the monopolar vortex depicted on the left-hand side of figure 6.10(c), as well as the (ω, ψ') -relationship of a Lamb vortex (solid line). The stream function ψ has been corrected according to $\psi' = \psi - U_x y + U_y x$, with $(U_x, U_y) = (-0.072, -0.021)$ cm s $^{-1}$ the drift speed of the monopole. The vorticity ω and the corrected stream function ψ' have been normalized by their extremal values $\omega_m = 0.22$ s $^{-1}$ and $\psi'_m = 1.51$ cm 2 s $^{-1}$, respectively. (b) Numerically obtained (ω, ψ') -scatter plot corresponding to the left-hand monopolar vortex displayed in figure 6.10(g) after correction for the monopole's translation speed $(U_x, U_y) = (-0.047, 0.009)$ cm s $^{-1}$. The extremal values of ω_m and ψ'_m are 0.256 s $^{-1}$ and 1.29 cm 2 s $^{-1}$, respectively. The solid line denotes the (ω, ψ) -relationship according to the Lamb-vortex model.

agreement with the full-numerical simulation is striking considering the translation speed, the distance between the vortex centres, and the orientation of the (passive) contours around the vortex centres. Moreover, both the dye-visualization experiment and the contour kinematics simulation show the entrainment of ambient fluid, which leads to the spiralled shape of the passive tracer distributions. Owing to horizontal diffusion of vorticity, such a spiral structure is not present in the vorticity distributions (see figure 6.10(a)–(h)). Since the dipole halves are weakly linked, the translation speed of the point-vortex pair is approximately the same as in the finite-difference simulation.

6.5 Conclusions

In this chapter, the evolution characteristics of dipolar vortices have been studied both in a cooperative and in an adverse strain flow. Experimentally, the strain flow was generated in the mid-plane of a stratified fluid by four rotating horizontal discs, whereas the dipolar vortex was created by a pulsed injection of a small amount of fluid. Dye-visualization studies and quantitative measurements of the planar flow field revealed that the evolution of the dipole in a cooperative strain flow was characterized by the formation of a head-tail

structure. Similar results were obtained in a numerical study by Kida, Takaoka & Hussain (1991). Despite the presence of the strain flow, the vorticity distribution in the core of the dipolar vortex could be accurately described by the Lamb-Chaplygin dipole model. The distance between the vortex centres was observed to remain nearly constant because the compressive effect of the strain flow was cancelled by the lateral diffusion of vorticity as well as by the initial entrainment of ambient fluid. A kinematic explanation of the head-tail formation was given by modelling the dipolar vortex with a point-vortex pair and its atmosphere, where the deformation of the atmosphere boundary was calculated by applying the contour kinematics technique. However, this kinematic model was not suitable for making a qualitative comparison with the experimental results. On the other hand, the full-numerical simulations based on the quasi-two-dimensional vorticity equation revealed a very good qualitative agreement with the laboratory observations.

When the dipole was embedded in an adverse strain flow, the vortex was observed to split up into two elliptic-like quasi-stationary Lamb vortices, which were oriented at an angle of approximately 45 degrees with respect to the horizontal strain axis. The vortex centres were passively advected by the strain flow. Both the contour kinematics results and the full-numerical simulations were in excellent qualitative agreement with the experimental observations.

Chapter 7

Conclusions

This thesis reports on the evolution characteristics of two-dimensional vortices in strain and shear flows. The experiments were performed both in rotating and in stratified fluids, and a comparison was made with analytical and numerical models. Quantitative information about the observed flow field was obtained by video recordings of passive tracer particles. Likewise, dye-visualization experiments were performed to study the qualitative behaviour of the flow.

First, the decay of monopolar vortices in a stratified fluid was investigated experimentally without the presence of an ambient flow. The observations were compared with an analytical decay model that accounted for both the increasing vertical thickness and the radial expansion of these disk-shaped structures. It was found that these monopolar vortices are characterized by a core of single-signed vorticity and a ring of oppositely-signed vorticity, and that their net circulation is zero. Furthermore, a good agreement was obtained with the theoretical model, which provides a better description of the vortex evolution than the diffusion models presented in earlier studies.

The behaviour of these shielded monopolar vortices was investigated in a straining background flow, the ambient flow being generated by an arrangement of oppositely rotating horizontal discs. The vortex evolution is characterized by the deformation into a tripolar-like structure, followed by the shedding of the accompanying satellites. In the next stage, the vortex evolves quasi-steadily. Owing to the diffusive decay of vorticity, the vortex is finally torn apart. It was found that the dynamics of the vortex core is very similar to that of an elliptic patch of uniform vorticity in a strain flow. Dye visualizations have revealed the 'stripping' of the vortex, i.e. weak vorticity was removed from the edge of the vortex by the ambient flow. Combination of the point-vortex model and the contour kinematics technique gives a simple explanation of the observed advection properties. However, the continuous spatial distribution of 'real' vortices must be considered in order to describe the final stage of the passive tracer evolution and to make a quantitative comparison with the laboratory observations.

Monopolar vortices were also studied in an irrotational annular shear flow, with the shear flow being generated in a rotating fluid by an appropriate source-sink configuration. The cyclonic vortex was created by the suction technique, and was characterized by single-

signed vorticity. Again, the laboratory observations demonstrated the deformation and stripping of the vortex. However, in contrast to uniform strain and shear flows, the vorticity filaments were asymmetrically attached to the vortex core. This asymmetric stripping process was explained simply by two point vortices. Contour dynamics simulations revealed that the final vortex elongation is a property of distributed vortices.

Finally, stratified fluid experiments demonstrated that the evolution of dipolar vortices in a strain flow is characterized either by the formation of a head-tail structure or by the breaking into two elliptically-shaped (quasi-steady) Lamb vortices. The laboratory observations were in very good agreement with the finite-difference calculations. A simple kinematic explanation of the head-tail formation was given by modelling the dipolar vortex with a point-vortex pair and its atmosphere.

The results described in this thesis are relevant to geophysical flow systems, and may lead to a better understanding of the stability of persistent large-scale vortices as occurring in the atmospheres of the Earth (e.g. the high and low pressure cells and 'blocking systems') and the giant planets (e.g. the elliptical 'spots' of Jupiter and Neptune). Since only a limited number of experimental studies have been performed, the present results are also believed to comply with the need for more experimental research in the field of two-dimensional vortices in ambient flows.

References

- Ahlnäs, K., Royer, T.C. & George, T.H. 1987 Multiple dipole eddies in the Alaska Coastal Current detected with Landsat Thematic Mapper data. *J. Geophys. Res.* **92**, 13041–13047.
- Arakawa, A. 1966 Computational design for long term numerical integration of the equations of fluid motion: Two-dimensional incompressible flow. Part I. *J. Comp. Phys.* **1**, 119–143.
- Batchelor, G.K. 1967 *An Introduction to Fluid Dynamics*. Cambridge University Press, Cambridge.
- Brickman, D. & Ruddick, B.R. 1990 The behavior and stability of a lens in a strain field. *J. Geophys. Res.* **95C**, 9657–9670.
- Butchart, N., Haines, K. & Marshall J.C. 1989 A theory and diagnostic study of solitary waves and atmospheric blocking. *J. Atm. Sci.* **46**, 2063–2078.
- Carton, X.J., Flierl, G.R. & Polvani, L.M. 1989 The generation of tripoles from unstable axisymmetric isolated vortex structures. *Europhys. Lett.* **9**, 339–344.
- Chaplygin, S.A. 1899 On a pulsating cylindrical vortex. *Trans. Phys. Sect. Imperial Moscow Soc. Friends of Natural Sciences* **10**, N 1, 13–22 (in Russian).
- Couder, Y. & Basdevant, C. 1986 Experimental and numerical study of vortex couples in two-dimensional flows. *J. Fluid Mech.* **173**, 225–251.
- Dalziel, S. 1992 *DigImage. Image Processing for Fluid Dynamics*. Cambridge Environmental Research Consultants Ltd.
- Dritschel, D.G. 1989 Strain-induced vortex stripping. In *Mathematical aspects of vortex dynamics* (ed. R.E. Caffisch), pp. 107–119. Society of Industrial and Applied Mathematics.
- Dritschel, D.G. & Waugh, D.W. 1992 Quantification of the inelastic interaction of unequal vortices in two-dimensional vortex dynamics. *Phys. Fluids A* **4**, 1737–1744.
- Fedorov, K.N. & Ginsburg, A.I. 1989 Mushroom-like currents (vortex dipoles): One of the most wide-spread forms of non-stationary coherent motions in the ocean. In *Mesoscale/Synoptic Coherent Structures in Geophysical Turbulence* (eds J.C.J. Nihoul and B.M. Jamart), pp. 15–24, Elsevier, Amsterdam.
- Flór, J.B. & van Heijst, G.J.F. 1994 An experimental study of dipolar structures in a stratified fluid. *J. Fluid Mech.* **279**, 101–133.

- Flór, J.B. & van Heijst, G.J.F. 1996 Stable and unstable monopolar vortices in a stratified fluid. *J. Fluid Mech.* **311**, 257–287.
- Flór, J.B., van Heijst, G.J.F. & Delfos, R. 1995 Decay of dipolar structures in a stratified fluid. *Phys. Fluids* **7**, 374–383.
- Greenspan, H.P. 1968 *The Theory of Rotating Fluids*. Cambridge University Press.
- Hairer E., Nørset, S.P. & Wanner, G. 1987 *Solving Ordinary Differential Equations - I: Nonstiff Problems*. Springer, Berlin.
- van Heijst, G.J.F. 1984 Source-sink flow in a rotating cylinder. *J. Engng Maths* **18**, 247–257.
- van Heijst, G.J.F. & Flór J.B. 1989 Dipole formation and collisions in a stratified fluid. *Nature*, **340**, 212–215.
- van Heijst, G.J.F., Kloosterziel R.C. & Williams, C.W.M. 1991 Laboratory experiments on the tripolar vortex in a rotating fluid. *J. Fluid. Mech.* **225**, 301–331.
- Hernan, M.A. & Jimenez, J. 1982 Computer analysis of a high speed film of the plane turbulent mixing layer. *J. Fluid Mech.* **119**, 323–345.
- Hide, R. 1968 On source-sink flows in a rotating fluid. *J. Fluid Mech.* **32**, 737–764.
- Hide, R. 1977 Experiments with rotating fluids. *Quart. J. R. Met. Soc.* **103**, 1–28.
- Hockney, R.W. 1970 The potential calculation and some applications. In *Methods in Computational Physics*, vol. **9**, 135–211.
- Hopfinger, E.J. & van Heijst, G.J.F. 1993 Vortices in rotating fluids. *Annu. Rev. Fluid Mech.* **25**, 241–289.
- Kida, S. 1981 Motion of an elliptic vortex in a uniform shear flow. *J. Phys. Soc. Japan* **50**, 3517–3520.
- Kida, S., Takaoka, M. & Hussain, F. 1991 Formation of head-tail structure on a two-dimensional uniform straining flow. *Phys. Fluids A* **3**, 2688–2697.
- Kimura, Y. & Hasimoto, H. 1985 Motion of two identical point vortices in a simple shear flow. *J. Phys. Soc. Japan* **54**, 4069–4072.
- Kirchhoff, G. 1876 *Vorlesungen über mathematische Physik: Mechanik*. Teubner.

- Kloosterziel, R.C. 1990 *Barotropic Vortices in a Rotating Fluid*. PhD thesis, University of Utrecht, The Netherlands.
- Kloosterziel, R.C. 1990 On the large-time asymptotics of the diffusion equation on infinite domains. *J. Engng Maths* **24**, 213–236.
- Kloosterziel, R.C. & van Heijst, G.J.F. 1991 An experimental study of unstable barotropic vortices in a rotating fluid. *J. Fluid Mech.* **223**, 1–24.
- Kloosterziel, R.C. & van Heijst, G.J.F. 1992 The evolution of stable barotropic vortices in a rotating free-surface fluid. *J. Fluid Mech.* **239**, 607–629.
- Kuo H-H. & Veronis G. 1971 The source-sink flow in a rotating system and its oceanic analogy. *J. Fluid Mech.* **45**, 441–464.
- Lamb, H. 1932 *Hydrodynamics*. (6th edn). Cambridge University Press.
- Legras, B., Santangelo, P. & Benzi R. 1988 High-resolution numerical experiments for forced two-dimensional turbulence. *Europhys. Lett.* **3**, 811–818.
- Legras, B. & Dritschel, D.G. 1991 The elliptic model of two-dimensional vortex dynamics. I: The basic state. *Phys. Fluids A* **3**, 845–854.
- Legras, B. & Dritschel, D.G. 1993 Vortex stripping and the generation of high vorticity gradients in two-dimensional flows. *Appl. Sci. Res.* **51**, 445–455.
- Legras, B. & Dritschel, D.G. 1994 Vortex stripping. In *Modelling of Oceanic Vortices* (ed. G.J.F. van Heijst), pp. 51–59. North Holland, Amsterdam.
- Lilly, D.K. 1983 Stratified turbulence and the mesoscale variability of the atmosphere. *J. Atmos. Sci.* **40**, 749–761.
- Marcus, P.S. 1993 Jupiter's Great Red Spot and other vortices. *Annu. Rev. Astron. Astrophys.* **31**, 523–573.
- Mariotti, A., Legras, B. & Dritschel, D.G. 1994 Vortex stripping and the erosion of coherent structures in two-dimensional flows. *Phys. Fluids* **6**, 3954–3962.
- McIntyre M.E. 1989 On the Antarctic ozone hole. *J. Atmos. Terr. Phys.* **51**, 29–43.
- McWilliams, J.C. 1980 An application of equivalent modons to atmospheric blocking. *Dyn. Atmos. Oceans* **5**, 43–66.

- McWilliams, J.C. 1984 The emergence of isolated coherent vortices in turbulent flows. *J. Fluid Mech.* **146**, 21–43.
- Melander, M.V., McWilliams, J.C. & Zabusky, N.J. 1987 Axisymmetrization and vorticity-gradient intensification of an isolated two-dimensional vortex through filamentation. *J. Fluid Mech.* **178**, 137–159.
- Melander, M.V., Zabusky, N.J. & McWilliams, J.C. 1987 Asymmetric vortex merger in two dimensions: Which vortex is “victorious”? *Phys. Fluids* **30**, 2610–2612.
- Melander, M.V., Zabusky, N.J. & McWilliams, J.C. 1988 Symmetric vortex merger in two dimensions: causes and conditions, *J. Fluid Mech.* **195**, 303–340.
- Meleshko, V.V. & van Heijst, G.J.F. 1994a On Chaplygin’s investigations of two-dimensional vortex structures in an inviscid fluid. *J. Fluid Mech.* **272**, 157–182.
- Meleshko, V.V. & van Heijst, G.J.F. 1994b Interacting two-dimensional vortex structures: point vortices, contour kinematics and stirring properties. *Chaos, Solitons & Fractals* **4**, 977–1010.
- Moore, D.W. & Saffman, P.G. 1971 Structure of a line vortex in an imposed strain. In *Aircraft Wake Turbulence and its Detection* (ed. J.H. Olsen, A. Goldberg, M. Rogers), pp. 339–354. Plenum.
- Nguyen Duc, T. & Sommeria, J. 1988 Experimental characterization of steady two-dimensional vortex couples. *J. Fluid Mech.* **192**, 175–192.
- Orlandi, P. 1990 Vortex dipole rebound from a wall. *Phys. Fluids A* **2**, 1429–1436.
- Overman, E.A. & Zabusky, N.J. 1982 Evolution and merger of isolated vortex structures. *Phys. Fluids* **25**, 1297–1305.
- Overman, E.A. & Zabusky, N.J. 1984 Diagnostic algorithms for contour dynamics. *Trans. First Army Conf. on Appl. Maths and Computing. ARO Rep.* 84-1, pp. 269–287.
- Paihua Montes, L. 1978 *Methodes numériques pour le calcul de fonctions-spline à une ou plusieurs variables*. Thèse de 3^e cycle, Université de Grenoble, France.
- Paireau, O., Tabeling, P. & Legras, B. 1996 Vortex subjected to a shear: an experimental study. *J. Fluid Mech.* (submitted).
- Polvani, L.M., Wisdom, J., DeJong, E. & Ingersoll, A.P. 1990 Simple dynamical models of Neptune’s Great Dark Spot. *Science* **249**, 1393–1398.

- Riley, J.J., Metcalfe, R.W. & Weissman, M.A. 1981 Direct numerical simulations of homogeneous turbulence in density stratified fluids. In *Proc. AIP Conf. Nonlinear Properties of Internal Waves* (ed. B.J. West), pp. 79–112.
- Robinson, A.R. 1983 *Eddies in Marine Science*. Springer Verlag, Berlin.
- Simpson, J.J., Dickey, T.D. & Koblinsky, C.J. 1984 An offshore eddy in the California Current System - I: Interior dynamics. *Prog. Oceanogr.* **13**, 5–49.
- Sommeria, J., Meyers, S.D. & Swinney, H.L. 1988 Laboratory simulation of Jupiter's Great Red Spot. *Nature* **331**, 689–693.
- Stewartson, K. 1957 On almost rigid rotations. *J. Fluid Mech.* **3**, 17–26.
- Taylor, G.I. 1918 On the dissipation of eddies. In *The scientific papers of Sir Geoffrey Ingram Taylor; Vol. 2: Meteorology, oceanography and turbulent flow* (ed. G.K. Batchelor), pp. 96–101. Cambridge University Press.
- Thomson, W. 1867. On vortex atoms. *Phil. Mag.* (ser. 4) **34**, 15–24.
- Waugh, D.W., Plumb, R.A., Atkinson, R.J., Schoeberl, M.R., Lait, L.R., Newman, P.A., Lowenstein, M., Toohey, D.W., Avallone, L.M., Webster, C.R. & May R.D. 1994 Transport of material out of the stratospheric Arctic vortex by Rossby wave breaking. *J. Geophys. Res.* D **99**, 1071–1088.
- Zabusky, N.J. Hughes, M.H. & Roberts, K.V. 1979 Contour dynamics for the Euler equations in two dimensions. *J. Comp. Phys.* **30**, 96–106.

Summary

The aim of the study presented in this thesis was to investigate both experimentally and theoretically the behaviour of two-dimensional vortices in strain and shear flows. This research topic is relevant to large-scale geophysical flow systems, such as the planetary atmospheres and the world's oceans. Experimentally, two-dimensional vortices were studied in rotating as well as stratified fluids. Apart from flow visualization studies, which were necessary to observe the qualitative behaviour of the flow field, quantitative information was obtained by video recordings of small tracer particles. Image analysis techniques were used to measure vorticity distributions and to follow individual particles.

The behaviour of monopolar and dipolar vortices embedded in a strain flow was studied in a stratified fluid, the ambient flow being generated by a suitable arrangement of rotating discs. Monopolar vortices were created by locally inducing a swirling motion, whereas dipolar vortices were generated by a horizontal, pulsed injection of a small amount of fluid. The experiments have shown that the monopolar vortex is deformed by the ambient flow, and that, after some time, the vortex is completely torn apart. Dye visualizations have revealed the 'stripping' of the vortex, i.e. long filaments of dye were peeled off from the edge of the vortex. The time-evolution of dipolar vortices in a strain flow was characterized either by the formation of a head-tail structure or by the breaking into two elliptic-like monopolar vortices.

Monopolar vortices were also examined in an irrotational annular shear flow. The background flow was generated in a rotating tank by an appropriate source-sink configuration, while the vortices were created by the suction technique. Again, the observations demonstrated the elongational deformation of the vortex and the shedding of weak vorticity from the vortex edge.

Theoretically, the laboratory observations were compared with analytical and numerical models. As a first approach, the monopolar and dipolar vortices were modelled numerically by point vortices surrounded by contours of passive tracers. As a second approach, numerical techniques of contour dynamics as well as a finite-difference method for solving the full two-dimensional vorticity equation were applied. The theoretical predictions were in good agreement with the experimental observations.

Samenvatting

Twee-dimensionale wervels komen in overvloed voor in grootschalige geofysische systemen, zoals de atmosfeer en de oceaan. Typische voorbeelden van grootschalige wervels zijn de hoge- en lage-drukgebieden in de atmosfeer. Zowel de atmosfeer als de oceaan kunnen beschouwd worden als een dunne laag die zich om de aardbol bevindt. Hierdoor zijn grootschalige wervels bij benadering twee-dimensionaal. De twee-dimensionaliteit wordt tevens bevorderd door de rotatie van de aarde en de verticale dichtheidsstratificatie. Twee-dimensionale wervels worden gekenmerkt door een lange levensduur en spelen een belangrijke rol bij het transport van bijvoorbeeld warmte en zout.

Grootschalige wervels kunnen vervormd worden door de aanwezigheid van een achtergrondstroming die het gevolg is van omringende wervels of de algehele west-oost circulatie. In dit proefschrift is het gedrag van twee-dimensionale wervels in 'strain flows' (rekstromingen) en 'shear flows' (scheringstromingen) onderzocht. De Grote Rode Vlek van de planeet Jupiter is een zeer kenmerkend voorbeeld van een twee-dimensionale wervel in een shear-stroming. Het promotie-onderzoek is o.a. van belang om een beter inzicht te krijgen in de uitwisseling van fysische bestanddelen tussen het zgn. ozon-gat boven Antarctica en de atmosfeer op lagere geografische breedten.

Aangezien experimentele studies nog maar nauwelijks gedaan zijn, werd in het huidige promotie-onderzoek de nadruk gelegd op laboratorium-experimenten. Quasi-twee-dimensionale stromingen werden gerealiseerd in een roterende vloeistof of in een niet-roterende gestratificeerde zoutoplossing. Met behulp van kleurstofvisualisatie en digitale beeldverwerking werd zowel kwalitatieve als kwantitatieve informatie verkregen over de stroming, zoals bijvoorbeeld het snelheidsveld en de vorticieteitsverdeling. De strain-stroming werd gegenereerd met behulp van vier roterende schijfjes, terwijl de shear-stroming gecreëerd werd door middel van een geschikte bron-put configuratie. Voor het opwekken van wervels werden dezelfde technieken gebruikt als in eerdere studies. Er zijn twee typen wervelstructuren onderzocht: monopolen en dipolen. Monopolaire wervels hebben één centrum waaromheen de vloeistof roteert, terwijl dipolen bestaan uit twee compacte gebieden van tegengestelde vorticieteit.

Uit de experimenten bleek dat monopolaire wervels in strain- en shear-stromingen een elliptische vorm verkrijgen. Ten gevolge van de afname van vorticieteit (door diffusie) werd de monopool uiteindelijk geheel uitgerekt. Kleurstofvisualisaties hebben het zgn. 'strippen' van de wervel aangetoond, d.w.z. vloeistof aan de rand van de monopool werd meegevoerd door de achtergrondstroming. Dit leidde tot het ontstaan van lange filamenten die symmetrisch of asymmetrisch verbonden waren met de monopool. De evolutie van dipolen in een strain-stroming werd gekarakteriseerd door de vorming van een kop-staart structuur of het opsplitsen van de dipool in twee ellipsvormige monopolaire wervels.

Voor een goede interpretatie van de experimenten werd een vergelijking gemaakt met analytische en numerieke modellen. Als eerste benadering werden monopolen en dipolen numeriek gemodelleerd d.m.v. puntwervels omgeven door passieve tracers. Als tweede benadering werd gebruik gemaakt van meer geavanceerde numerieke technieken, zoals contourdynamica en eindige-differentie methoden. De theoretische resultaten kwamen goed overeen met de experimentele waarnemingen.

Dankwoord

Graag wil ik een aantal mensen bedanken die een belangrijke rol hebben gespeeld bij de totstandkoming van dit proefschrift. Op de eerste plaats natuurlijk GertJan van Heijst voor zijn inspirerende begeleiding. Mede dankzij zijn enthousiasme voor de stromingsleer ga ik met plezier en vol goede moed verder in het huidige vakgebied.

Natuurlijk ben ik ook veel dank verschuldigd aan de studenten die als afstudeerder of stagiair een belangrijke bijdrage geleverd hebben aan het promotie-onderzoek: Marcel Beckers, André Linssen, Bas van Wesenbeeck, Angelique van Hassel, Jeroen van Ooijen, Bas Nijsten, Michel van Rooij en Oliver Atassi. Verder waren de laboratorium experimenten niet mogelijk geweest zonder de technische ondersteuning door Marius Bogers en zijn team, Harm Jager, Eep van Voorthuisen, Louis Wasser en Jan Willems.

Daarnaast heb ik veel hulp gehad van Gert van der Plas wanneer er weer eens problemen waren op software- of hardwarematig gebied. Ook van de software geschreven door Oscar Velasco Fuentes heb ik veel profijt gehad. I would like to thank Roberto Verzicco (Università di Roma "La Sapienza") for his kind willingness to provide the finite-difference code, and for helpful suggestions on some numerical problems. Jos van Geffen wil ik bedanken voor de nuttige uitbreiding van de eindige-differentie code, Pauline Vosbeek voor het ter beschikking stellen van het contourdynamica programma en Herman Clercx voor het onderhoud over fundamentele numerieke zaken. Tevens wil ik graag Slava Meleshko bedanken die als een soort 'wetenschappelijke encyclopedie' mij regelmatig wees op (langvergeten) publicaties uit de vorige eeuw.

In het laatst stadium van mijn promotieperiode hebben prof. L. van Wijngaarden, prof. M.E.H. van Dongen en prof. F.W. Sluijter mij nuttige opmerkingen en suggesties gegeven betreffende het proefschrift. Verder dank ik alle medewerkers van de vakgroep Transportfysica voor de plezierige tijd in de afgelopen vier jaar.

Tenslotte wil ik mijn ouders en vooral Monique bedanken voor al hun goede zorgen en steun.

Curriculum Vitae

Ruben Robert Trieling was born in Dordrecht on January 25, 1969. From 1981 to 1987 he followed pre-university education (VWO) at the Rythoviuscollege in Eersel. After that, he went to Eindhoven University of Technology to study Technical Physics. His graduation project was concerned with the electric transport in two-dimensional electron gasses. After receiving his university degree in 1992, he became a Junior Scientist (Onderzoeker in Opleiding) at the Fluid Dynamics Laboratory of the same university. The Ph.D. project was supported by the Netherlands Foundation for Fundamental Research on Matter (FOM). As from October 1, 1996, Ruben Trieling is working at the Royal Netherlands Meteorological Institute (KNMI) in De Bilt. The postdoctoral research involves the predictability of two-layer contour dynamics systems.

Ruben Robert Trieling werd geboren op 25 januari 1969 in Dordrecht. Van 1981 tot 1987 doorliep hij zijn middelbare schooltijd (VWO) op het Rythoviuscollege in Eersel. Daarna begon hij met zijn studie Technische Natuurkunde aan de Technische Universiteit Eindhoven. Zijn afstudeerproject betrof het elektrische transport in twee-dimensionale electronengassen. Na het behalen van zijn ingenieurstitel in 1992 werd hij Onderzoeker in Opleiding bij de vakgroep Transportfysica aan de Faculteit Technische Natuurkunde van dezelfde universiteit. Het promotie-onderzoek werd gefinancierd door de stichting Fundamenteel Onderzoek der Materie (FOM). Vanaf 1 oktober 1996 is Ruben Trieling werkzaam bij het Koninklijk Nederlands Meteorologisch Instituut (KNMI) in De Bilt. Het post-doctorale onderzoek betreft de voorspelbaarheid van twee-lagen contourdynamica systemen.

Stellingen

behorende bij het proefschrift
'Two-Dimensional Vortices in Strain and Shear Flows'
R.R. Trieling, 27 november 1996

1. De radiale expansie van platte, monopolaire wervelstructuren in een gestratificeerde vloeistof is niet voornamelijk te wijten aan 'entrainment' van omgevingsvloeistof, zoals beweerd wordt door Flór en Van Heijst. Radiale diffusie speelt een minstens even belangrijke rol.

*J.B. Flór & G.J.F. van Heijst (1996) J. Fluid Mech. 311, 257–287.
Dit proefschrift, hoofdstuk 2.*

2. Puntwervels zijn zeer geschikt voor het beschrijven van de kinematische eigenschappen van monopolaire wervels in strain- en shear-stromingen.

Dit proefschrift, hoofdstuk 4 en 5.

3. Twee-dimensionale wervels in een niet-uniforme shear-stroming bezitten een zekere dynamische equivalentie met quasi-twee-dimensionale wervels boven een bepaalde bodemtopografie.

4. Wervels kunnen dienen ter vermaak van het grote publiek.

5. De ontmoeting tussen twee personen is als de samenkomst van twee scheikundige stoffen: als er enige reactie is, veranderen ze alle twee.

C.G. Jung.

6. De overheidsinkomsten die door accijnsheffingen via de tabaksindustrie ontvangen worden, zijn debet aan het milde anti-rokersbeleid van de Nederlandse overheid.

7. De (wan)orde op iemands bureau kan gezien worden als een afspiegeling van zijn of haar gedachten.

8. There is hardly anything in the world that some man cannot make a little worse and sell a little cheaper, and the people who consider price only are this man's lawful prey.

John Ruskin.

9. Ter bevordering van het gebruikersgemak dienen muziekboeken bij voorkeur ingebonden te zijn door middel van een ringband.
10. De piramiden van Gizeh, die omstreeks 2450 v.Chr. gebouwd werden, zijn een nauwkeurige weerspiegeling van het sterrenpatroon zoals dat rond 10450 v.Chr. werd waargenomen in de Gordel van Orion.
R.G. Bauval & A.G. Gilbert (1994) The Orion Mystery.
11. Er is echte vriendschap wanneer de stilte tussen twee mensen behaaglijk is.
Dave Tyson Gentry.
12. Het verhoogde geluidsniveau tijdens t.v.-commercials komt de levensduur van de afstandsbediening niet ten goede.